ABSTRACT

A STUDY OF THREE TRANSITION METAL COMPOUNDS AND THEIR APPLICATIONS

by
Zhen Qin

The $La_{5/8-y}Pr_yCa_{3/8}MnO_3$ with colossal magnetoresistance (CMR) effect has a rich phase diagram and is well studied for its electronic phase separation phenomenon, where the ferromagnetic (FM) metal order co-exists and competes with the charge-ordered (CO) insulator phase. High Pr doping will favor the CO order, leading a sharp FM to CO dominated phase transition around Pr concentration of 0.3 and above. Hydrostatic pressure favors FM metallic order without damaging the sample and can be tuned continuously. In this study, pressurized-magnetic and resistivity measurements was done on a $La_{0.25}Pr_{0.375}Ca_{0.375}MnO_3$ single crystal. The sample, at first sitting in CO dominated phase, changed into FM upon a small amount of pressure. This transition was verified both by magnetic and resistivity measurement results.

$FeSe_{1-x}$ is one of the newly discovered iron-based superconductors. As a binary transition metal compound, it is of great research interest due to the simple stacking 2d-layered structure. The itinerant or localized nature of the electrons in Fe^{2+} ion has been debated but not concluded. In this research, Raman scattering measurements on $FeSe_{0.97}$ were applied within a temperature range from 5 K to 300 K. The excitation near 185 cm^{-1} was assigned to B_{1g} phonon excitation. Broad and intensive excitation peaks were found in a wide region between 200 cm^{-1} and 700 cm^{-1}, and they are classified as the Fe^{2+} crystal field excitations. These excitations suggest a low Hund coupling constant and thus support the itinerant nature of 3d electrons in Fe^{2+} ion indirectly.

Evanescent wave was discovered to be able to tunnel through a negative reflectance index material and gets strengthened inside an alternating metal-high K material 1d photonic crystal structure. Where the regular light eventually fails in sub-micron photolithography due to diffraction limit, evanescent wave can carry the information of small structure below diffraction limit. In our study, HfO_2, a transitional metal oxide widely used in IC fabrication, was used as the high-K material to construct a sub-wavelength length imaging device for nano scale photolithography applications.

A STUDY OF THREE TRANSITION METAL COMPOUNDS AND THEIR APPLICATIONS

by
Zhen Qin

A Dissertation
Submitted to the Faculty of
New Jersey Institute of Technology
in Partial Fulfillment of the Requirements for the Degree of
Doctor of Philosophy in Materials Science and Engineering

Interdisciplinary Program in Materials Science and Engineering

May 2011

.

APPROVAL PAGE

A STUDY OF THREE TRANSITION METAL COMPOUNDS AND THEIR APPLICATIONS

Zhen Qin

Dr. Tao Zhou, Dissertation Co-Advisor — Date
Assistant Professor of Physics, NJIT

Dr. Sang-Wook Cheong, Dissertation Co-Advisor — Date
Professor of Physics, Rutgers University-New Brunswick

Dr. Andrei Sirenko, Committee Member — Date
Associate Professor of Physics, NJIT

Dr. Keun H Ahn, Committee Member — Date
Assistant Professor of Physics, NJIT

Dr. Weida Wu, Committee Member — Date
Assistant Professor of Physics, Rutgers University-New Brunswick

BIOGRAPHICAL SKETCH

Author: Zhen Qin

Degree: Doctor of Philosophy

Date: May 2011

Undergraduate and Graduate Education:

- Doctor of Philosophy in Materials Science and Engineering,
  New Jersey Institute of Technology, Newark, NJ, 2011

- Master of Science in Microelectronics and Solid State Electronics,
  Nanjing University, Nanjing, P. R. China, 2005

- Bachelor of Science in Physics,
  Nanjing University, Nanjing, P. R. China, 2002

Major: Materials Science and Engineering

Presentations and Publications:

Z. Qin, C. Zhang, S. O'Malley, K. Lo, T. Zhou and S-W. Cheong
Crystal field excitations in the Raman spectra of $FeSe_{1-x}$
Solid State Communications 150, 768 (2010).

Z. Qin, Y.J. Choi, H.T. Yi, T. Zhou, and S-W. Cheong
Giant increase of magnetic transition temperature in $La_{0.25}Pr_{0.375}Ca_{0.375}MnO_3$ *under pressure*
Presented on APS March meeting 2010, Session A36.

I dedicate this thesis to New Jersey Institute of Technology

ACKNOWLEDGMENT

I would like to express my sincere thanks to my co-advisors, Professor Tao Zhou from NJIT and Professor Sang Wook Cheong from Rutgers University. It is their advising that illuminated my research project. I have learned not just academic skills, but also scientific thinking and discipline from both.

I would also like to thank Professor Andrei Sirenko, Professor Ken Ahn, and Professor Weida Wu for being my committee members. I understand that all were busy and really appreciate your work on my behalf.

DOE grant DE-FG02-07ER46382, DARPA SBIR program, and Dymas Research Inc are also acknowledged for their funding, support and collaboration.

I would like to thank my student colleagues who helped me during the research. They are: Sean O'Malley, Y. J. Choi, H. T. Yee, Nara Lee, Chenglin Zhang, and Phil, Dan, Matt, Steve, Andy.

I have to thank Xingmiao Liu, for the encouragement that she has given me. This dissertation would not be possible without the understanding and support of my parents, Jinyuan Qin and Fengxiu Zhou, I love them dearly.

TABLE OF CONTENTS

TABLE OF CONTENTS
(Continued)

Chapter **Page**

TABLE OF CONTENTS
(Continued)

LIST OF TABLES

LIST OF FIGURES

LIST OF FIGURES
(Continued)

Figure **Page**

LIST OF FIGURES
(Continued)

LIST OF FIGURES
(Continued)

LIST OF FIGURES
(Continued)

Figure **Page**

CHAPTER 1

HIGH PRESSURE MAGNETIC AND ELECTRICAL MEASUREMENTS ON $La_{0.25}Pr_{0.375}Ca_{0.375}MnO_3$

1.1 Introduction

1.1.1 Transition Metal

Transition metal usually refers to the elements between group 2 and group 12 elements in the periodic table [1]. Based on International Union of Pure and Applied Chemistry (IUPAC), it is defined as "an element whose atom has an incomplete d sub-shell, or which can give rise to cations with an incomplete d sub-shell". Many transition metals are strongly correlated materials because of the incompletely filled d electron shell and narrow band. The electrons interact with each other and can not be treated as single electrons in the averaged electron "sea". Various anomalous phenomena are found in transition metals, e.g. high-Tc superconductors, spintronic materials, Mott insulators, spin Peierls materials, heavy Fermion materials, quasi-low-dimensional materials, colossal magnetoresistance materials, thermoelectric materials. There are many theoretical approximations (e.g. extensions of local-density approximations (LDA+U, GGA, SIC, GW, etc) and simplified model Hamiltonians such as Hubbard model) proposed to solve the complicated systems but most of them can only handle specific matter, a general theory paradigm has still yet to be established. The complex electron interactions implicate new phenomena and therefore make transition metals one of the most interesting material families.

Transition-metal oxides are materials whose electronic properties are determined by interplay of several interactions of comparable magnitude, all on the order of 1 eV. Schematically, these are as follows [2]:

Table 1.1 Estimates of characteristic energies in $LaMnO_3$

U_{dd}	4.0 eV	$J_H = U_{ex}/2$	1.0 eV
U_{pd}	4.5 eV	Δ_{cf}	1.8 eV
		δ_{JT}	0.6 eV
W=12t	1.0 eV	$\|J_{ij}\|$	0.001 eV

(1) the Mott - Hubbard interaction U_{dd} , which is the cost of creating a $d^{n+1}d^{n-1}$ charge excitation in an array of d^n ions;

(2) the charge-transfer interaction U_{pd}, which is the cost of transferring an oxygen p electron to the neighboring d ion to create a p^5d^{n+1} charge excitation from p^6d^n ;

(3) the transfer integral t which determines the d-electron bandwidth W;

(4) the Hund rule on-site exchange interaction U_{ex} which is the energy required to flip a d-electron spin;

(5) the crystal-field interactions Δ_{cf} and Jahn-Teller interaction δ_{JT}.

Besides the classical Bloch - Wilson insulators where the Fermi level falls in a gap in the one-electron density of states, transition-metal oxides may be Mott - Hubbard or charge-transfer insulators when the electron correlations are such that $U_{dd} > W$ or $U_{pd} > W$ respectively. Most oxides of the early 3d transition metals are Mott - Hubbard

insulators and many oxides of the late 3d transition metals are charge-transfer insulators.

At the end of the 3d series, the charge transfer gap may go to zero, and the oxides then become metals. In the middle of the series where $U_{dd} \approx U_{dp}$ the nature of the gap is less clear cut. A summary of the magnitudes of these interactions in $LaMnO_3$ is given in table 1.1.

1.1.2 Electronic States of D-electron Systems

The atomic orbitals of transition-metal elements are constructed as eigenstates under the spherical potential generated by the transition-metal ion [3]. When the solid is formed, the atomic orbital forms bands due to the periodic potential of atoms. Because of the relatively small radius of the d electron wave function as compared to the lattice constant of the crystals, d-electron systems have in general smaller overlap and hence smaller bandwidths than alkaline metals. In transition-metal compounds, the overlap is often determined by indirect transfer between d orbitals through ligand p orbitals (Figure 1.1). This means that the bandwidth is determined by the overlap (in other words, hybridization) of the d wave function at a transition metal atom and the p wave function of the adjacent ligand atom if the ligand atoms bridges between two transition-metal atoms. Another origin of the relatively narrow bandwidth in transition-metal compounds is that 4s and 4p bands are pushed well above the d band, where screening effects by 4s and 4p electrons do not work well. In any case, because of the narrow bandwidth, the

tight-binding models constructed from atomic Wannier orbitals provide a good starting point.

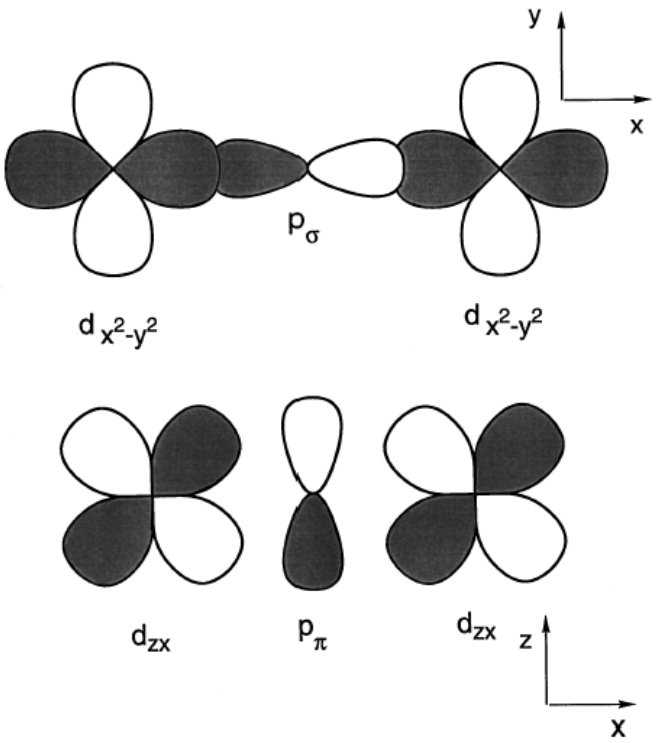

Figure 1.1 Examples of configurations for transition-metal 3d orbitals which are bridged by ligand p orbitals.

The bands that are formed are under the strong influence of anisotropic crystal fields in solids. Because the $3d$ orbital has the total angular momentum L = 2, it has fivefold degeneracy (Lz = 2,1,0,-1,-2) for each spin and hence a total of tenfold degeneracy including spins. This degeneracy is lifted by the anisotropic crystal field. In transition-metal compounds, a transition-metal atom is surrounded by ligand atoms to help in the formation of a solid through the increase in cohesive energy by covalent bonds of the two. Because the ligand atoms have a strong tendency towards negative valence, the crystal field of electrons in the direction of the ligand atom is higher than in

other directions. Figure 1.2 shows an example of the crystal field splitting, where the cubic lattice symmetry leads to a higher energy level of fourfold degenerate e_g (or d_y) orbital and sixfold degenerate lower orbitals, t_{2g} (or d_ε). When a transition-metal atom is surrounded by ligand atoms with an octahedron configuration, the e_g orbital has anisotropy with larger amplitude in the direction of the principle axes, namely, toward neighboring ligand atoms. The basis of these orbitals may be expanded by $d_{x^2-y^2}$ and $d_{3z^2-r^2}$ orbitals. On the other hand, the t_{2g} orbital has anisotropy with larger amplitude of the wave function toward other directions and may be represented by d_{xy}, d_{yz}, and d_{zx} orbitals. For other lattice structures with other crystal symmetries, such as tetragonal or orthorhombic as in the case of 2D perovskite structure, similar crystal field splitting appears. In the case of tetrahedral surroundings of ligand ions, e_g orbitals lie lower than t_{2g}, in contrast to cubic symmetry or octahedron surroundings.

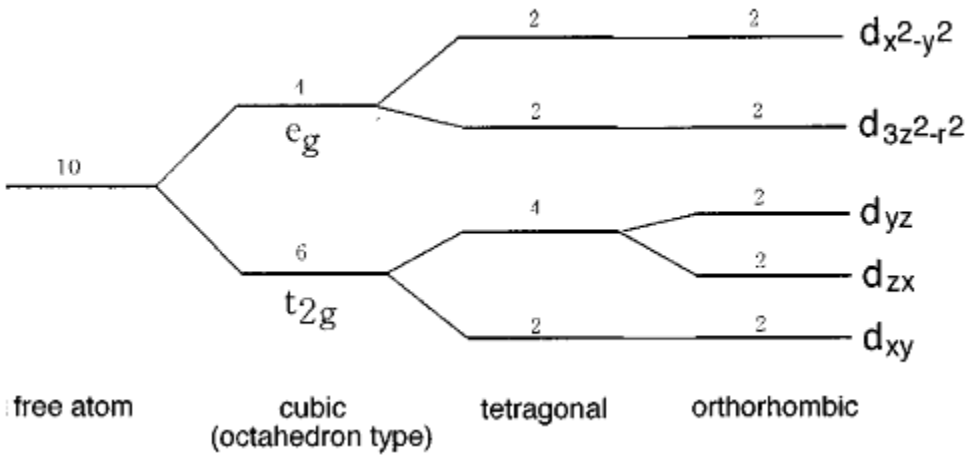

Figure1.2 Crystal-field splitting of 3d orbitals under cubic, tetragonal, and orthorhombic symmetries. The numbers cited near the levels are the degeneracy.

1.1.3 Colossal Magnetoresistance (CMR)

In 2007, the Nobel Prize in physics was awarded to Albert Fert and Peter Grünberg for the discovery of the discovery of giant magnetoresistance (GMR) in the year of 1988 [4]. GMR is a quantum mechanical magnetoresistance effect observed in thin film structures composed of alternating ferromagnetic and non magnetic layers. GMR has triggered the rise of a new field of electronics called spintronics which has been used extensively in the read heads of modern hard drives and magnetic sensors. A hard disk storing binary information can use the difference in resistance between parallel and antiparallel layer alignments as a method of storing 1s and 0s. More recently, it has become recognized that some materials, specifically 3d transition-metal oxides, possess large room-temperature magnetoresistance associated with a paramagnetic–ferromagnetic phase transition, and that phenomenon is called colossal magnetoresistance (CMR). The growth of interest in their properties stems in large part from the prospect of creating metal oxide devices whose performance exceeds GMR devices, while the GMR effect can cause around 10% difference in resistance, the CMR can change the resistance by several orders of magnitudes. In addition, it is now recognized that the large magnetoresistance in these oxides is the result of a unique type of metal–insulator transition, the understanding of which complements the drive for applications.

The majority of CMR compounds are perovskite manganites [5], they have the chemical formula $T_{1-x}D_xMnO_3$, where the T is trivalent lanthanide cation (e.g. La, Pr), and D is a divalent, e.g. alkaline-earth (e.g. Ca, Sr, Ba), cation. For both of the end

members of the composition, $LaMnO_3$ and $CaMnO_3$ (x= 0 and 1 respectively), the ground state is antiferromagnetic (AF), which is explained by spins interacting via the superexchange interaction when the metal–oxygen–metal bond angle is close to 180°. In the doping range of $x \approx 0.2 - 0.4$, the ground state is ferromagnetic (FM), and the paramagnetic-to-ferromagnetic transition is accompanied by a sharp drop in resistivity *ρ(T).* This has been reported as a phenomenon since 1950. These materials have attracted much attentions recently, because it is realized that the magnetoresistance (MR) associated with this correlation between magnetization (*M*) and resistivity (ρ) can be very large (and therefore named as colossal magnetoresistance (CMR)), and that the basic interaction responsible for the ρ–*M* correlation, the double-exchange (DE) interaction [6-8] between Mn^{3+} and Mn^{4+} neighbors, is not sufficient to explain the CMR effect by itself [9]. The CMR effect is also related to the formation of small lattice polarons in the paramagnetic state. Besides the renewed interest in the FM state, another type of collective state, charge order (CO), has drawn much attention, which is usually observed for $x > 0.3$. At these doping levels CO can compete with the FM ground state, leading to complex electronic phase behavior as chemical formula changes [10–12]. The most important advance in understanding these disparate effects is the realization of the importance of electron–phonon (e–ph) coupling. Several theories have been presented to explain the role of e–ph coupling in producing CMR [13, 14]. The e–ph coupling can explain not only CMR, but also the polaron signatures in transport studies, the large isotope effect on the FM Curie temperature [15], the large Debye–Waller factors [16] and

the CO state and its large sound velocity anomalies [12]. The origin of strong e–ph coupling is the large Jahn–Teller effect which occurs for d^4 ions in an octahedral ligand environment [17]. The question of how this e–ph coupling becomes significant in the CMR range ($x \approx 0.2$–0.4) is one of the focus issue to be solved by theory.

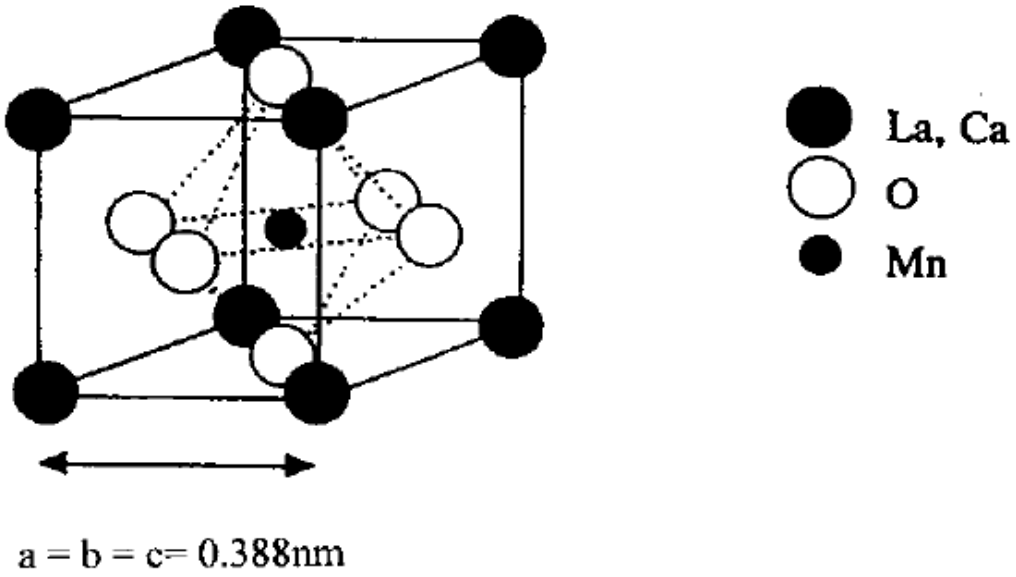

Figure 1.3 The ideal cubic perovskite structure, ABO_3. A is a large cation, similar in size to O^{2-} ; B is a small cation such as Mn^{3+} or Mn^{4+} , octahedrally-coordinated by oxygen.

Chemically, the system is characterized by the wide range of cations which can occupy the A site in the perovskite structure [2], which may sit at the body-centre or the cube corner (Figure 1.3). A good way to regard the structure is as a cubic close-packed array formed of O^{2-} anions and large A cations, with the small B cations in the octahedral

interstitial sites. As will be discussed afterwards, the ideal cubic structure is distorted by cation size mismatch and the Jahn - Teller effect, whereby a distortion of the oxygen octahedron surrounding the B site cation splits the energy levels of a 3d ion such as Mn^{3+}, thus lowering the energy. The distorted structures are frequently orthorhombic. Divalent cations which can occupy the body-centre A site include calcium, barium, strontium and lead; trivalent cations include yttrium, lanthanum, praseodymium, neodymium and some other rare earths (R). Besides manganese, many perovskite-structure oxides form with gallium or another 3d element such as chromium, iron, cobalt or nickel on the B sites. The rare-earth orthof- errites $RFeO_3$ are one example of a series of perovskite-structure oxides. There are many others. Any of the trivalent 3d cations can substitute partially for manganese. An exhaustive compilation of data on perovskite-structure compounds by Goodenough and Longho was published in a 1970 Landoldt-Bernstein volume.

The main effects of the various substitutions are to vary the number of electrons in the 3d band and to alter the inter-atomic distances and bond angles. Whenever different ions of the same 3d element with different numbers of electrons occupy crystallographically equivalent B sites, say B1 and B2, there is a partly-filled d band with a tendency towards metallic conduction. The configurations $3d^n$ (B1) - $3d^{n+1}$ (B2) and $3d^{n+1}$ (B1) - $3d^n$ (B2) are degenerate provided that there is no charge ordering. The idea that mixed valence can lead to metallic conduction is due to Verwey and de Boer. It was developed with particular reference to magnetite (Fe_3O_4) in The Netherlands in the 1930s. The occupancy of the B sites in the spinel structure of magnetite by a mixture of Fe^{3+}

($3d^5$) and Fe^{2+} ($3d^6$) leads to electrical conduction and ferromagnetic B-B exchange interactions. The idea of mixed-valence ferromagnetism was then applied to oxides with the perovskite structure.

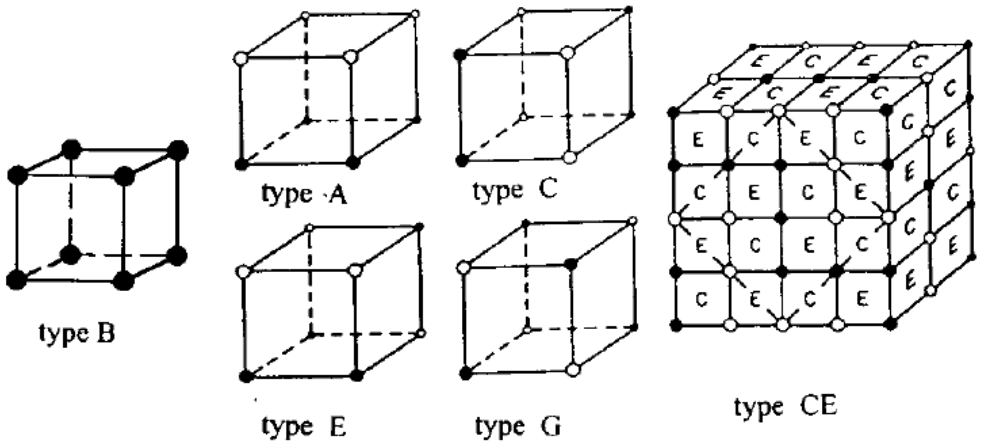

Figure 1.4 Some possible magnetic modes for the B-site cations in the perovskite structure (solid and open circles represent the two antiferromagnetic sublattices).

The mixed-valence manganites can exhibit magnetic order, charge order and orbital order. Examples of charge and orbital order are given later in Figure 6. Some of the simplest magnetic modes for the B sites in the perovskite structure are illustrated in Figure 3. Mode B is ferromagnetic, but all the others are antiferromagnetic and entail an enlarged magnetic unit cell. Modes A, C and G consist of oppositely aligned ferromagnetic planes of the type {001}, {110} and {111} respectively. Mode G, where each B-site cation is oriented antiparallel to its six neighbours will be favoured by negative B-O-B superexchange interactions. Modes C and E each have four antiparallel and two parallel neighbours, whereas mode A has four parallel and two antiparallel

neighbours. A composite CE mode is composed of a chequer board of alternating C and E blocks. The magnetic axis is usually indicated by a suffix x, y or z. Modes may be combined, so that A_xB_z for example represents a canted antiferromagnet with the antiferromagnetic axis along x (a) but with the net ferromagnetic moment along z (c).

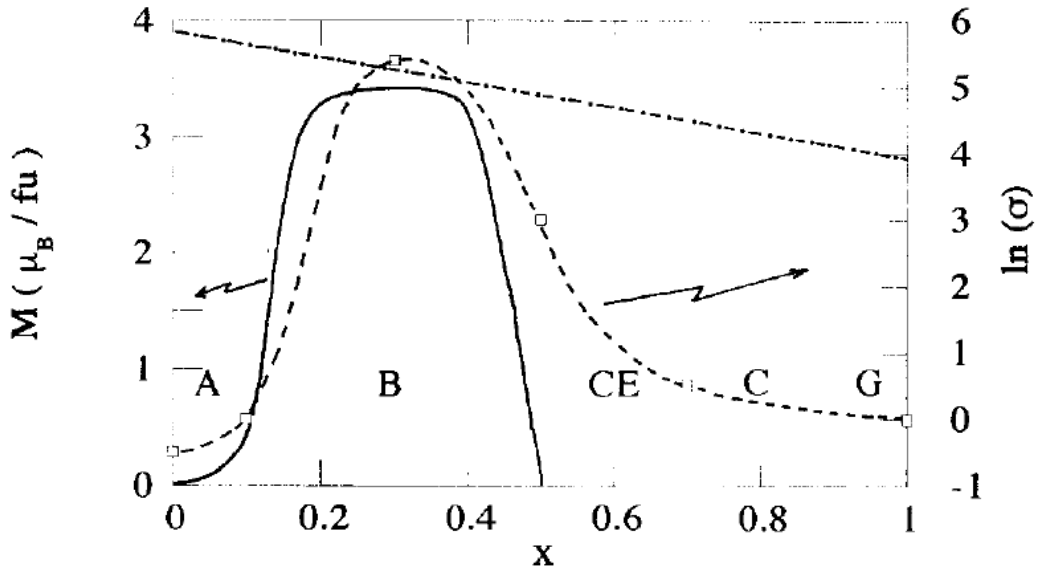

Figure 1.5 Low-temperature magnetic modes and ferromagnetic moment for the $(La_{1-x}Ca_x)MnO_3$ series compared with the electrical conductivity at 80 K , the spin-only moment for a mixture of Mn^{3+} and Mn^{4+}.

The crystallographic and magnetic structures for the $(La_{1-x}Ca_x)MnO_3$ compounds were determined in 1955 by Wollan and Koehler [11] in a remarkably complete neutron and X-ray diffraction study as a function of Mn^{4+} content. In particular, the neutron data revealed a very rich magnetic phase diagram where, for different doping levels, antiferromagnetism can take different configurations (A, C, CE and G types) and can even coexist with ferromagnetism (B type). The magnetic structures are indicated on

figure 1.5. There are three main regions: for small amounts of Mn^{4+} the compounds have essentially antiferromagnetic properties. For x around 0.3, they become ferromagnetic but, for x > 0.5, they revert to antiferromagnetism up to the end-member $CaMnO_3$. From magnetization and susceptibility results, Jonker concluded that the exchange is weakly positive (ferromagnetic) between two $3d^4$ Mn^{3+} ions, negative (antiferromagnetic) between two $3d^3$ Mn^{4+} ions and positive between a $3d^4$ Mn^{3+} and a $3d^3$ Mn^{4+} ion. Resistivity measurements also revealed a strong correlation between electron transport and magnetic properties. The resistivity is lowest for the x = 0.3 composition corresponding to the best ferromagnetism, whereas high resistivities are associated with the antiferromagnetic compositions.

There are two other CMR compound families that can not be explained easily by the theory developed to describe manganite perovskites. They are the pyrochlores, e.g. $Tl_2Mn_2O_7$ [18], and the spinels ACr_2Ch_4 where A = Fe, Cu, Cd (for example) is a tetrahedrally coordinated cation and Ch is a chalcogen (S, Se, Te). Similar to manganese perovskites, these compounds exhibit large drops in resistivity at their FM T_C values. What makes them different from perovskites is that they possess no mixed valence (and as a result, have low carrier density), an A-site cation (Tl or A) capable of contributing states at the Fermi level, and large deviations of the metal–anion–metal bond angle from 180° .

1.1.4 Jahn - Teller Effect

Ions on B sites of the perovskite manganese are coordinated by an octahedron of oxygen neighbors, assuming for the moment that there is an integral number of d electrons per site. The intra-atomic electronic correlations which give rise to the Hund rules for the free ion are perturbed by the crystalline electrostatic field due to the oxygen anions. The five d orbitals, each of which can accommodate one electron of each spin, are split by the octahedral crystal field into a group of three t_{2g} (d_{xy}, d_{yz}, d_{zx}) orbitals which have their lobes oriented between the oxygen neighbors and a group of two eg (d_{x2-y2} , d_{z2}) orbitals which are directed towards the oxygen neighbors. The former obviously have a lower energy because of the electrostatic repulsion of electrons on neighboring sites, and the crystal field splitting Δ_{cf} between the t_{2g} and e_g orbitals is of the order 1.5 eV. The intra-atomic correlations which give rise to the Hund first rule (maximum S) is represented on a one-electron energy diagram by introducing an energy splitting U_{ex} of the orbitals, which is greater than Δ_{cf}. Good evidence that U_{ex} and Δ_{cf} are quite similar in magnitude in the perovskite-structure oxides is provided by the trivalent cobalt in $LaCoO_3$ which does not follow the Hund first rule; it is in a low-spin state, $3d^6$, t_{2g}^6, with S = 0. Trivalent nickel in nickel-substituted manganites is also of a low-spin nature. Manganese ions generally have a high spin; the divalent ion Mn^{2+} has a very stable $3d^5$ configuration, a half -filled shell $t_{2g}^{3\uparrow}e_g^{2\uparrow}$ with S = 5/2 and a spherically symmetric electron density. Trivalent manganese is $3d^4$, $t_{2g}^{3\uparrow}eg^{\uparrow}$ with S = 2, whereas quadvalent

manganese is $3d^3$, $t_{2g}^{3\uparrow}$ with S = 3/2. The spin-only moments of these ions are $5\mu_B$, $4\mu_B$ and $3\mu_B$ respectively.

A distortion of the oxygen octahedron lowers the symmetry of the cubic crystal field in such a way that the centre of gravity of the t_{2g} levels and the centre of gravity of the e_g levels is unchanged. There is therefore nothing to be gained by Mn^{2+} or Mn^{4+} from such a distortion, but Mn^{3+} can lower its energy in proportion to the distortion, and the corresponding penalty in elastic energy will scale as the distortion squared, hence we have the marked tendency of d^4 ions to distort their octahedral environment in order to lower their energy. This is the Jahn - Teller effect. For example, the tetragonal elongation of the octahedron found in the O-type structure will stabilize the d_{z2} orbital relative to the d_{x2-y2} orbital, as shown in figure 1.6.

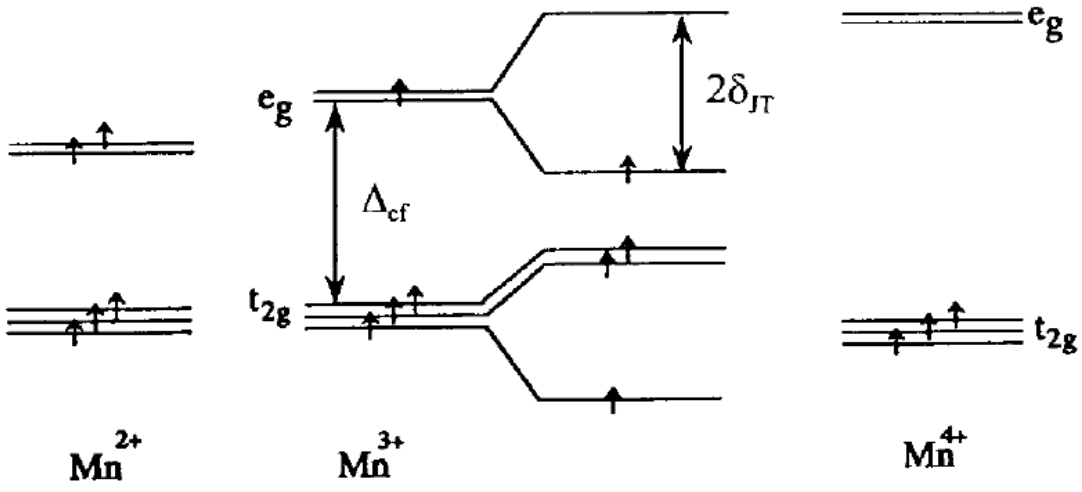

Figure 1.6 Occupancy of one-electron energy levels for Mn^{4+}, Mn^{3+} and Mn^{2+} in octahedral coordination. The effect of a tetragonal distortion is to lower the energy of Mn^{3+} by δ_{JT}, but it leaves the others unchanged.

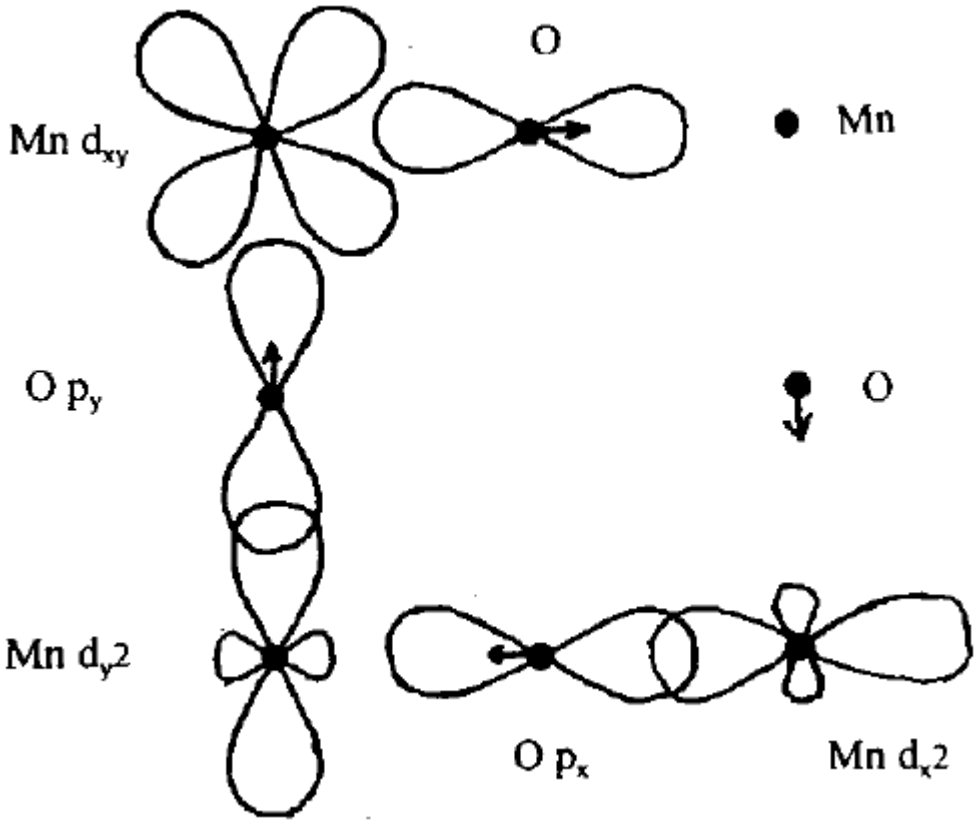

Figure 1.7 Illustration of the orbital overlap in a plane of the perovskite structure. The d_{xy} orbital (a t_{2g} orbital) has little overlap with the 2p orbitals of the oxygen neighbours, whereas the d_{x2} and d_{y2} orbitals (e_g orbitals) overlap strongly with the oxygen p_x or p_y orbitals to form a σ * band. Displacements of the oxygen atoms in the plane are indicated by arrows.

The t_{2g} orbitals overlap relatively little with the orbitals of nearby oxygen or lanthanum ions (Figure 1.7) so these electrons tend to form a localized $t_{2g}^{3\uparrow}$ ion core. However the e_g orbitals overlap directly with the p orbitals of the oxygen neighbors, so they tend to form a σ* anti-bonding band. The end-member compounds such as $LaMnO_3$ have a distorted perovskite structure where the Fermi level falls in a gap between the two Jahn - Teller split e_g bands. However, intermediate compositions such as $(La_{1-x}Ca_x)MnO_3$ with a cubic structure have a partly-filled s band, extending in three dimensions. These

band electrons, which we refer to as the Zener electrons, hop from one manganese site to another with spin memory. They are both conduction electrons and mediators of the ferromagnetic exchange. Direct overlap of the t_{2g} core electrons of adjacent manganese ions leads to antiparallel exchange coupling, since only theese orbitals are empty.

1.1.5 Double Exchange

Double exchange (DE) was first proposed by Zener in the year of 1951 to explain the qualitative aspects of the experimentally discovered relation between transport and magnetic properties, namely the increase in conductivity upon the polarization of the spins [19]. Zener consider the DE process as $Mn_{1\uparrow}{}^{3+}O_{2\uparrow,3\downarrow}Mn^{4+} \rightarrow Mn^{4+}O_{1\uparrow,3\downarrow}Mn_{2\uparrow}{}^{3+}$, where 1, 2, and 3 label electrons that belong either to the oxygen between manganese, or to the e_g-level of the Mn-ions (Figure 1.8). In this process, electron 2 moves from the oxygen to the right Mn-ion, and electron 1 moves from the left Mn-ion to the oxygen. These two motions happen simultaneously and thus the process dubbed as double exchange. The detailed DE process was presented by Anderson and Hasegawa in year 1955, and it involves a second-order process in which the two states described above go from one to the other using an intermediate state $Mn_{1\uparrow}{}^{3+}O_{3\downarrow}Mn_{2\uparrow}{}^{3+}$. In this scenario, the effective hopping for the electron to move from one Mn-site to the next is proportional to the square of the hopping involving the p-oxygen and d-manganese orbitals (t_{pd}). In addition, if the localized spins are considered classical and with an angle θ between nearest-neighbor ones, the effective hopping becomes proportional to $\cos(\theta/2)$. If $\theta = 0$

the hopping is the largest, while if $\theta = \pi$, corresponding to an antiferromagnetic background, then the hopping cancels. The quantum version of this process has been described by Kubo and Ohata in the year of 1972.

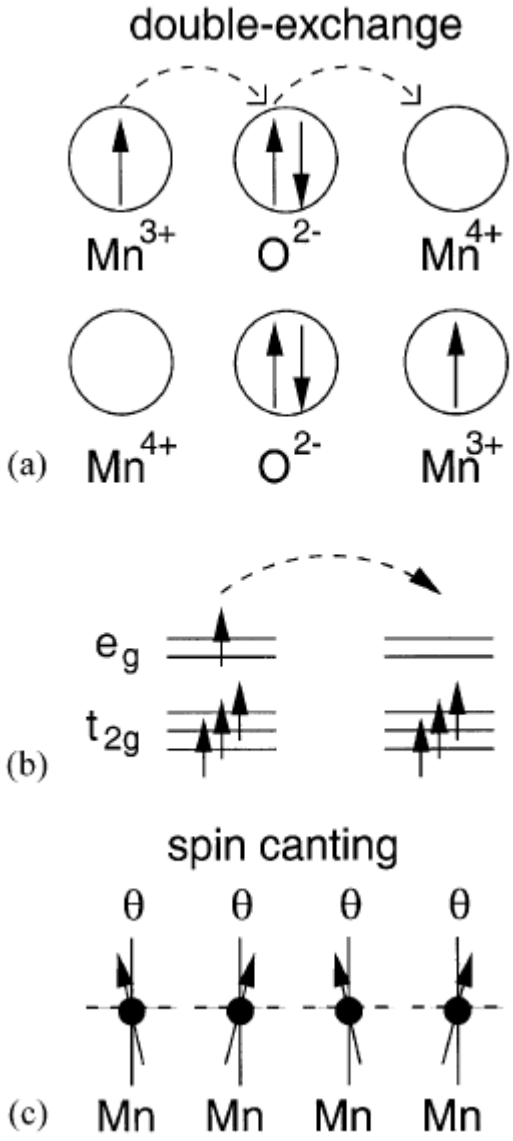

Figure 1.8 (a) Sketch of the Double Exchange mechanism which involves two Mn ions and one O ion. (b) The mobility of e_g-electrons improves if the localized spins are polarized. (c) Spin-canted state which appears as the interpolation between FM and AF states in some mean-field approximations.

DE has been very important and effective in explaining the manganite. However it is based on the assumption that the states are uniform, while the recent research shows that the manganite system has coexisting clusters of competing phases. DE alone is no more sufficient to describe the material.

1.1.6 Ferromagnetism, Charge Ordering and Orbital Ordering

There are three mechanisms that produce effective ferromagnetism interactions. First is double exchange, where electrons are mobile, which is valid for non-charge-ordered states and where the oxygen plays a key role (Figure 1.9). The second is Goodenough's approach where covalent bonds are important (here the electrons do not have mobility in spite of the FM effective coupling), and it mainly applies to charge-ordered states. The third is based on purely Mn models (no oxygens) which lead to FM interactions mainly as a consequence of the large Hund coupling in the system. Out of all the three mechanisms the double exchange is the most pronounced and best accepted.

Kanamori [20] pointed out that the carriers in mixed-valence manganites may be strongly coupled to local lattice distortions. Orbital ordering can occur at certain carrier concentrations when the d electrons occupy an asymmetric orbital, as shown in Figure 1.10 (b). The driving force is partly direct electrostatic repulsion of the charge clouds, but coupled Jahn-Teller distortions of adjacent octahedral stabilize the effect. Finally, Figure 1.10 (c) illustrates the coupled charge and orbital order expected when x=1/2.

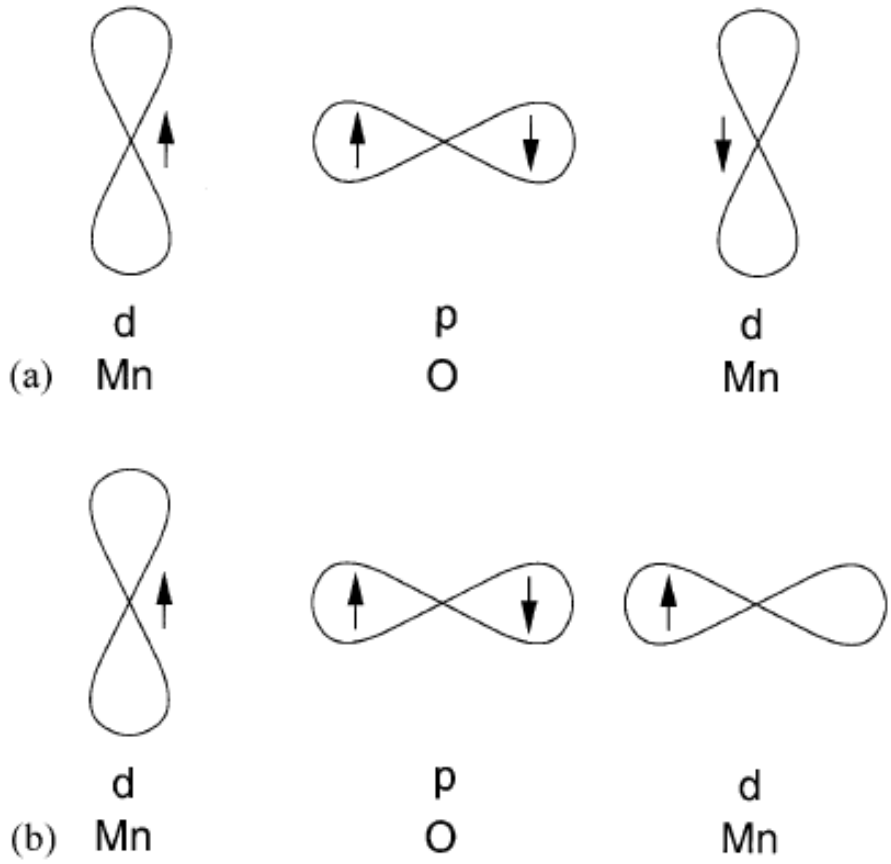

Figure 1.9 Generation of antiferromagnetic (a) or ferromagnetic (b) effective interactions between the spins of Mn ions mediated by oxygen, depending on the orientation of the Mn orbitals.

Charge ordering is a phenomenon generally observed in mixed-valent transition metal oxides (Figure 1.10(a)). When differently charged cations (i.e., 2+ and 3+) in an oxide order on specific lattice sites, the hopping of electrons between the cations is no longer favored. An increase in the electrical resistivity at the charge-ordering transition can therefore be observed, usually accompanied by a change in crystal symmetry. Because transition metal ions also carry spins, it is interesting to examine the magnetic (spin) ordering in the solids in relation to charge ordering. A well-known example of

charge ordering is found in Fe_3O_4 (magnetite). Charge ordering has been discovered to exist in rare earth manganese with perovskie structure.

Charge-ordered states are usually related to the CE-type antiferromagnetic (AFM) state which often shows interesting patterns like stripes, zig-zag chains, checkboards. Goodenough explained the CO with the idea of "semicovalent". In his model, Mn^{3+} and Mn^{4+} are arranged like a checkerboard (see Figure 1.11) and the $Mn3^{+}$ sites have a Jahn-Teller (JT) distortion. The charge ordering and the JT distortion in the CE-type AFM state have been observed by x-ray and neutron diffraction measurements.

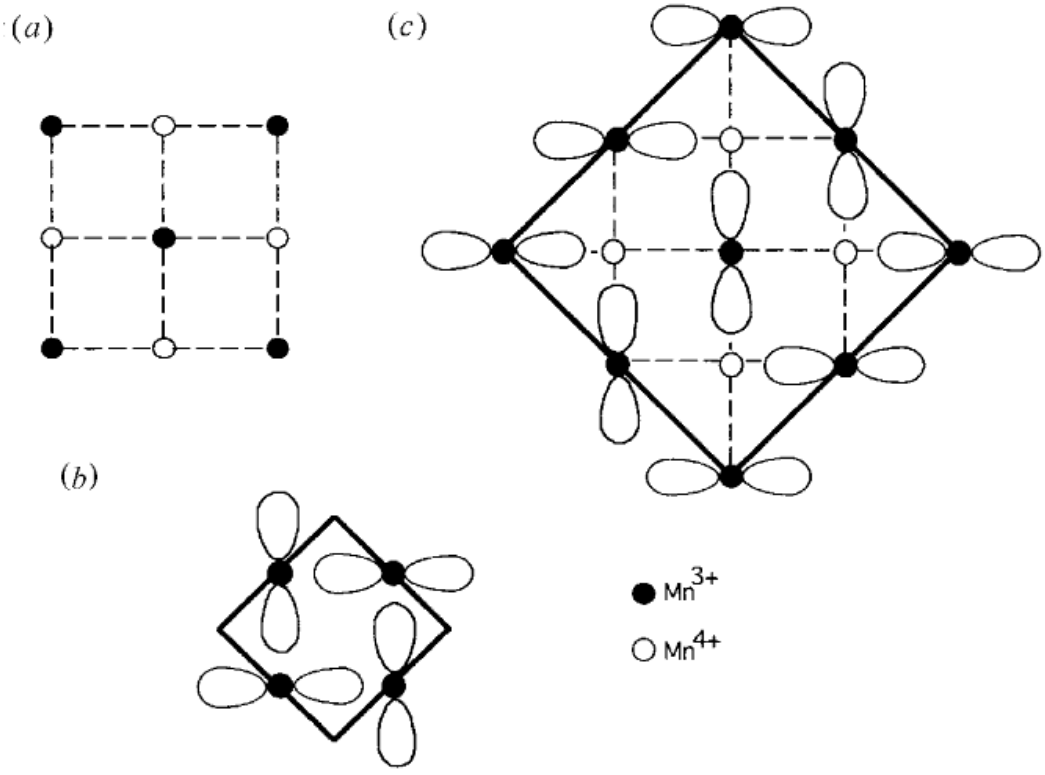

Figure 1.10 (a) Charge ordering of Mn^{3+} and Mn^{4+} in a mixed crystal with x = 1/2. (b) Orbital ordering of the d_{z^2} orbitals of Mn^{3+} when x = 0. (c) Combined charge and orbital ordering when x = 1/2.

.

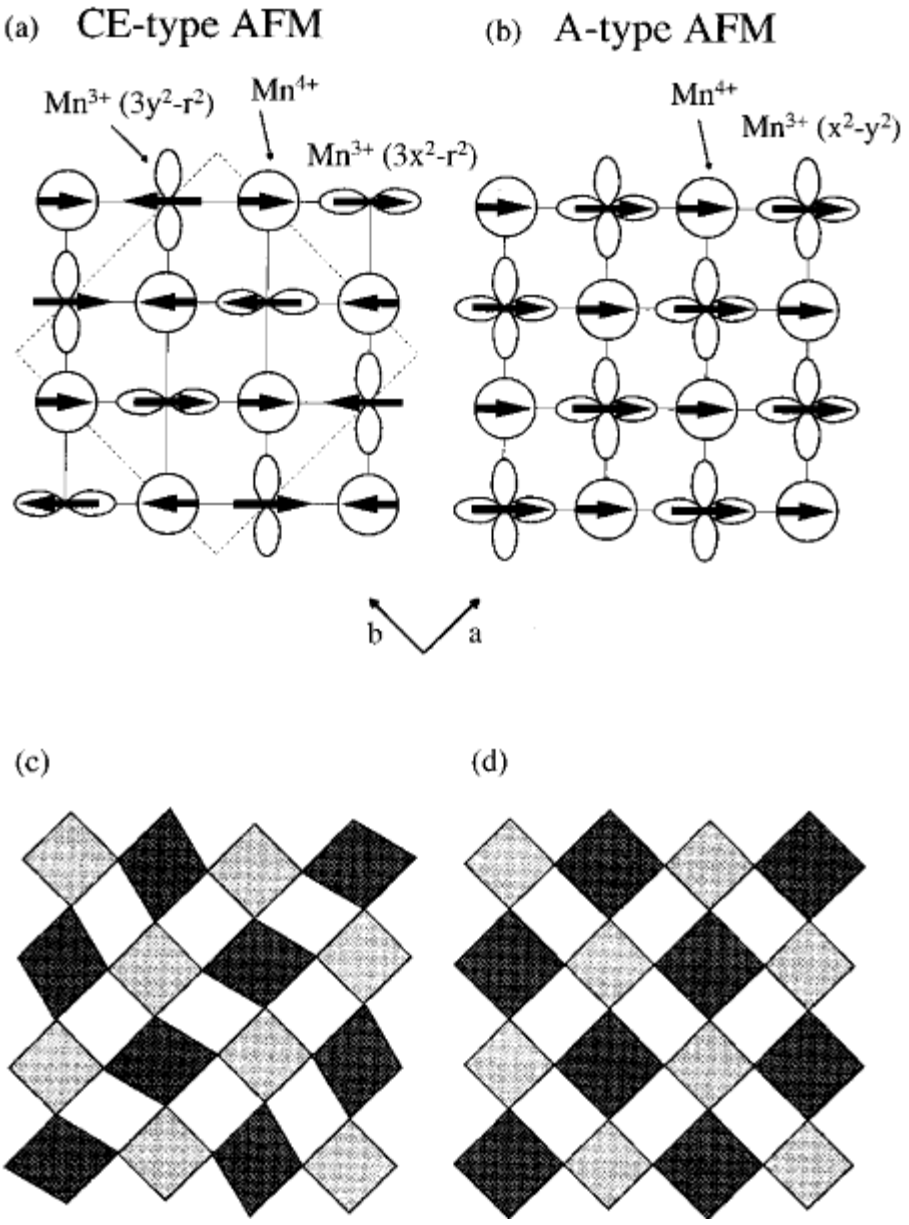

Figure 1.11 Upper panel: Spin, charge, and orbital ordering for the CE-type AFM CO state (a) and for the A-type AFM CO state (b). The broken line shows the unit cell for the CE-type AFM CO order. Lower panel: JT distortions consistent with the CE-type AFM CO state (c) and the A-type AFM CO state (d). The dark and light shaded squares show the Mn3+ and Mn4+ sites, respectively.

Charge-ordered state and ferromagnetism are mutually exclusive, mainly because charge ordering inhibits the electron transfer process that is associated with double exchange, while double exchange favors metallic ferromagnetism state. The competition between FM and CO states can be understood qualitatively in terms of the variations of the A site cation radius $<r_A>$, which will result in changes on the Mn-O-Mn angle. The ferromagnetic and antiferromagnetic exchange coupling constants J_{FM} and J_{AFM} decrease with diminishing $<r_A>$, the former more rapidly than the latter. On the other hand, the single-ion Jahn-Teller energy E_{JT} must be invariant with A-cation size. The largest $<r_A>$ region, therefore, is dominated by the large J_{FM} and only ferromagnetism is observed. In the regime of slightly smaller cation size, J_{AFM} is larger than J_{FM} and ferromagnetism gives way to antiferromagnetism on cooling. The e_g electrons, which are localized magnetically, further lower the configuration energy by undergoing charge ordering that coexists with the antiferromagnetic state. Such a state should be sensitive to magnetic fields. In the small (r_A) regime, the cooperative Jahn- Teller effect becomes the dominating factor, leading to charge ordering at a higher temperature than the antiferromagnetism. Here the state is much less sensitivity to magnetic fields. The charge-ordered, insulating state in the manganates can be "melted" into the metallic state by the application of magnetic fields, the temperature-field behavior depending on the size of the A-site cations. The size of the A-site cations presumably determines the Mn-O-Mn angles, thereby controlling the e_g bandwidth and the strength of the double-exchange mechanism. For example, in $Y_{0.5}Ca_{0.5}MnO_3$, with its small A-site

cations, not only does the charge ordering occur in the paramagnetic state at a relatively high temperature(T_{CO} = 250 K, T_N = 140 K), but it is nearly impossible to destroy the robust charge-ordere state by the application of magnetic field.

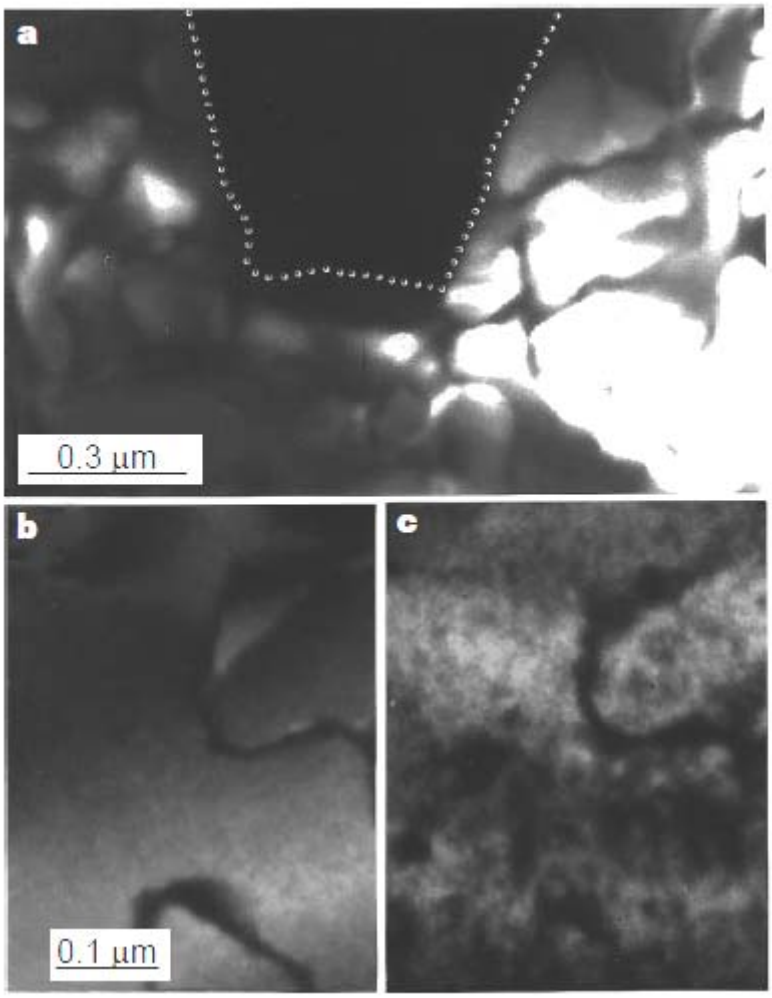

Figure 1.12 Dark-field images for $La_{5/8-y}Pr_yCa_{3/8}MnO_3$ obtained by using a superlattice peak caused by CO.

The competition and co-exsistance of ferromagnetism and charge ordering was revealed in Uehara's paper [21]. Evidences show that the FM metallic phase and CO insulating phase exsist in sub-micron scale domains, and that coexistance is called

electrical phase separation (see Figure 1.12, Figure 1.13). The CMR effect of the system is determined by the percolative current through isolated FM island domains. Electron conduction between neighbouring FM domains is reduced if their magnetizations are not aligned. This conduction reduction is particularly large in manganites where hopping electrons are strongly aligned with the local orientation of magnetization (manganites are the so-called halfmetallic ferromagnets). The degree of this magnetization misalignment increases when the concentration of Pr approaches the percolation threshold where the abundance of CO domains leads to poor connection of the minority FM domains.

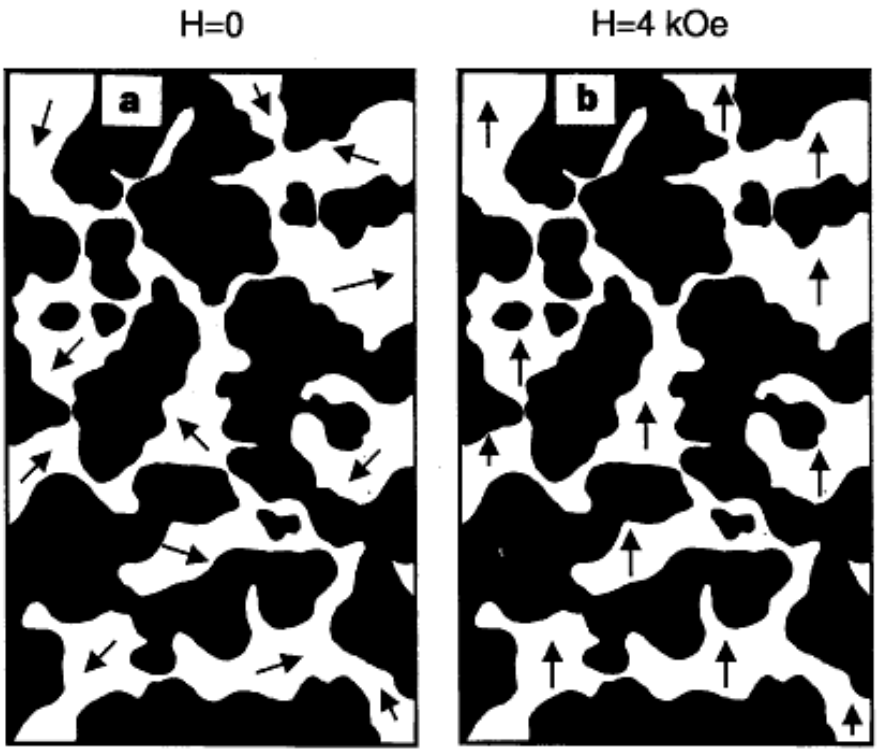

Figure 1.13 Schematic illustration of the sub-micrometer-scale coexistence of the x = 1/2-type CO insulating (dark area) and FM metallic (white area) domains. The typical size of domains is ~ 0.5mm. In zero field (a), the magnetizations of FM domains are random, but all magnetizations of FM domains can be aligned by applying field of about 4 kOe (b).

Therefore, with decreasing relative volume of FM domains, ρ_0 increases much faster than the prediction of simpler percolative transport. When all these magnetizations of FM domains were aligned in applied fields, ρ_0 follows closely the percolation prediction.

1.1.7 Bandwidth Control

Unlike the ionic $4f$ levels, which are little broadened by overlap and hybridization, the $3d$ ionic levels acquire a substantial bandwidth, of order 1 eV, from overlap with the neighboring orbitals [2]. Bandwidth is the crucial parameter that controls the balance between the FM and CO states. The bandwidth is defined as $W = 2Zt$, where t is the transfer integral and Z is the number of manganese nearest neighbors. This is indicated in the modified one-electron energy levels of Figure 1.14.

In perovskite manganese compounds, Mn occupies B site, which is octahedral and 6 cordinated, therefore the bandwidth can be written in Anderson-Hasegawa scenario as following:

$$W_\sigma = 12t_{ij}\left(\uparrow\uparrow\right) = \varepsilon_\sigma \lambda_\sigma^2 \cos\phi \left\langle \cos\left(\theta_{ij}/2\right)\right\rangle \tag{1.1}$$

Here ε_σ is the stabilization energy which is constant with fixed electron concentration, λ_σ is the covalent-mixing parameter which increases when hydrostatic pressure is applied, 180-ϕ is the angle of the Mn-O-Mn bound (in another word, ϕ stands for how much the Mn-O-Mn bound have been distorted), and θ_{ij} is the angle between the two spins.

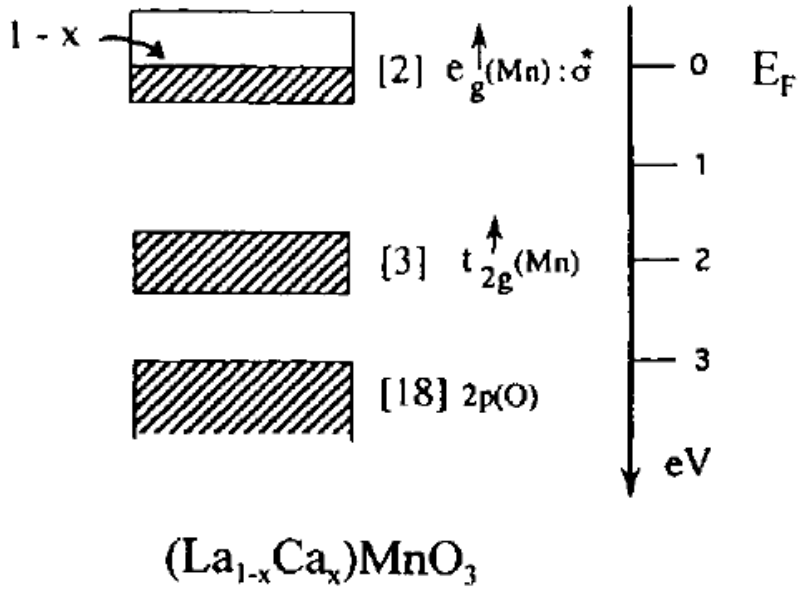

Figure 1.14 Schematic energy band structure of $(La_{1-x}Ca_x)MnO_3$.

ϕ is highly dependant on tolerance factor t, which is defined as following:

In a perovskite structure AMO_3, the tolerance factor

$$t \equiv \frac{\langle r_A \rangle + \langle r_O \rangle}{\sqrt{2}\left(\langle r_M \rangle + \langle r_O \rangle\right)} \tag{1.2}$$

Here $\langle r_A \rangle$, $\langle r_M \rangle$ and $\langle r_O \rangle$ stands for the ionic radius of the A site ion, M site ion and oxygen ion respectively. In perovskite manganese system, M is Mn, t increases with larger A site ion and is usually smaller than 1. A $t < 1$ places the M–O bonds under compression and the A–O bonds under tension. The structure can alleviate these stresses by a cooperative rotation of the MO_6 octahedra. Rotation about a cubic [110] axis, gives the orthorhombic Pbnm structure of $GdFeO_3$; rotation about a [111] axis gives the

rhombohedral R3c structure of $LaAlO_3$; and rotation about an [001] axis gives the tetragonal structure of low-temperature SrTiO3. These rotations bend the M–O–M bond angle from 180° to$180° - \phi$, and ϕ increases as $t < 1$ decreases, which means smaller t will result in smaller $\cos\phi$ and therefore smaller W. $\cos(\theta_{ij}/2)$ is maximized when $\theta_{ij} = 0$, which stands for more ferromagnetic ordering.

There are 3 ways to control the bandwidth W. First is hydrostatic external pressure, which modifies the covalent-mixing parameter λ_σ and changes bandwidth W as a consequence. The second way is to change the effective A site ionic radius $\langle r_A \rangle$, and therefore change the M–O–M bond angle ϕ, this is usually done by doping smaller ions into A site. The third way is modification of the chemical composition using the solid solution or mixed crystal effect. In the case of transition-metal compounds, the electron correlation arises from a narrow d band. Therefore alloying of the transition-metal cations should be avoided for W control, and the solid solution in other chemical sites is usually attempted. One of the best known examples of this W control is the case of $NiS_{2-x}Se_x$ crystals.

1.1.8 Phase diagram

$La_{1-x}Ca_xMnO_3$ was intensively studied due to its colossal magnetoresistance effect [22]. Magnetic structures in the mixed-valence manganites were first determined from neutron diffraction measurements carried out by Wollan and Koehler in 1955 on the $(La_{1-x}Ca_x)MnO_3$ system. The mixed-valent manganite has a rich phenomenology of

phase diagram strongly depending on the Ca doping level, x [23] (see Figure 1.15). As first established from magnetization measurements, the compounds are ferromagnetic around x=0.3 where moments are close to the expected spin-only value. The sublattice moments for the pure antiferromagnetic phases at x=0 and x=1 are also close to the spin-only values. The different magnetic ordering found as the proportion of Mn^{3+} to Mn^{4+} is varied depends primarily on the charge ordering in the perovskite lattice. A simple set of rules can be inferred by comparing the magnetic and charge order; exchange coupling is ferromagnetic between Mn^{3+} and Mn^{4+} ions, antiferromagnetic between two Mn^{4+} ions, and ferromagnetic or antiferromagnetic between two Mn^{3+} ions. The ferromagnetic bond between the ions in different valence states is also the shortest.

At low Mn^{4+} contents ($x \geq 0$ in $(La_{1-x}Ca_x)MnO_3$), a ferromagnetic component B_z along the c axis appears in the neutron diffraction patterns which grows for increasing x up to x = 0.3 where the samples are entirely ferromagnetic [2]. The coexistence of A_y and B_z modes is consistent with spin canting or micro-scale phase segregation. The variation in the ^{55}Mn hyperfine frequencies in an applied field favors the latter interpretation [24]. The existence of narrow magnetic Bragg peaks associated with the B_z mode indicates some underlying long-range ferromagnetic order in the $0 < x < 0.3$ compounds [25] but weak magnetic satellites around the Bragg peaks in a crystal with x = 0.08 have been attributed to correlated ferromagnetic density fluctuations on the scale of 1.7 nm with an average separation of 3.5 nm [26]. Curie temperatures in this concentration range reach 250 K with a saturation magnetization slightly less than the expected spin only value of

3.7 μ_B per manganese atom. The cubic structure obtained in this region reflects the absence of charge ordering. At Mn^{4+} concentrations above 0.35, a different mixture of ferromagnetism and antiferromagnetism is found. The new antiferromagnetic phase consists of a regular stacking of the C and E types, called the CE type by Wollan and Koehler. It is the result of charge ordering near a Mn^{4+} to Mn^{3+} ratio of unity (x = 0.5). On heating the x = 0.5 compound, the antiferromagnetic order turns ferromagnetic at T_N = 170 K before becoming paramagnetic at T_C = 225 K [27]. The antiferromagnetic → ferromagnetic transition is accompanied by a change from commensurate to incommensurate charge order [28]. As x increases, the CE structure progressively transforms itself to the C-type structure corresponding to another charge ordering obtained for a Mn^{4+} to Mn^{3+} ratio of 3 (x = 0.75). The magnetic configuration is then one of ferromagnetic chains ordered antiferromagnetically. Both C and CE structures present tetragonal distortions from the ideal cubic phase with c < a (the ferromagnetic bond again being shorter than the antiferromagnetic bond). As the proportion of Mn^{4+} increases further, they replace Mn^{3+} ions at random creating more antiferromagnetic bonds in the structure. The end member $CaMnO_3$ indeed contains only Mn^{4+} and is fully antiferromagnetic, with the nearest-neighbor G-type antiferromagnetic structure. The crystallographic cell for the latter is almost cubic since Mn^{4+} ($3d^3$), unlike Mn^{3+} ($3d^4$), does not tend to deform its octahedral environment.

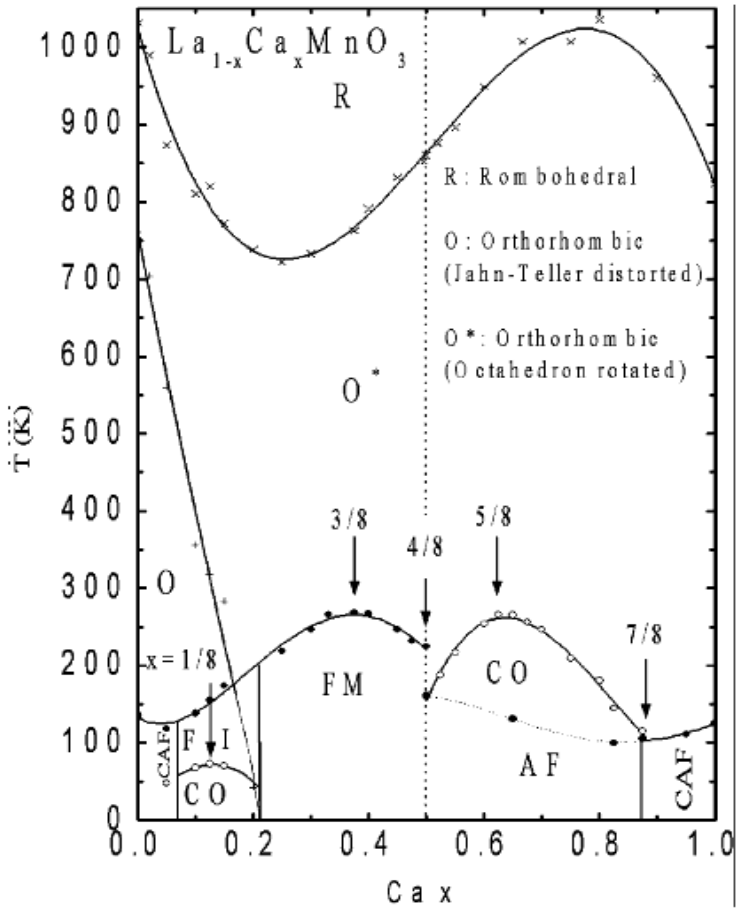

Figure 1.15 Phase diagram of $La_{1-x}Ca_xMnO_3$.

Goodenough [29] was the first to attempt a comprehensive explanation of the properties of the mixed-valence manganites [2]. He discussed the phase diagram of $(La_{1-x}Ca_x)MnO_3$ in chemical terms, considering the hybridization of manganese orbitals: dsp^2 for Mn^{3+} which forms square coplanar bonds, and d^2sp^3 for Mn^{4+} which forms octahedral bonds to six near neighbors. These ions can form bonds of different nature with the surrounding oxygens through which magnetic coupling is mediated.

(1) Covalent bonds are formed when one empty manganese orbital points towards an O^{2-} ion. This is a strong short bond which leads to antiferromagnetic superexchange between two manganese atoms forming covalent bonds with a common oxygen atom. Each electron of the bond has the same spin as its corresponding manganese because of the Hund rule coupling. The spins of the two electrons of the oxygen atoms have to be antiparallel because they belong to the same 2p orbital. The resulting coupling between Mn^{4+} ions (or Mn^{3+} in certain cases) is therefore antiferromagnetic.

(2) Semicovalence arises when only one out of the two manganese atoms surrounding an O^{2-} has a hybridized orbital available pointing towards the oxygen. In that case, full covalence is not possible since only one side of the O^{2-} orbitals can share an electron with the neighboring manganese ion. The other bond is ionic, and the oxygen ion is displaced towards the first manganese, with which it forms the covalent bond. One electron is then localized on the oxygen ion to which it confers a magnetic moment that is antiparallel to the spin of the covalent electron (the two electrons sharing the oxygen orbitals have to be antiparallel). Because of the Hund rule, the manganese ion participating in the bond has its moment parallel to the electron shared with the oxygen. On this side of the ionic bond, there is a direct (therefore antiferromagnetic) exchange interaction between the magnetic moment of the anion and that of the neighboring manganese. The resulting configuration is a ferromagnetic arrangement of the manganese ions with an antiparallel oxygen between them.

(3) Ionic bonds are obtained when the empty Mn^{3+} (dsp^2) orbitals point away from the O^{2-} ion. This is a long bond appearing only between two Mn^{3+}. There is no indirect exchange in that case.

(4) Double exchange is the last bonding possibility, involving the simultaneous transfer of an electron from the Mn^{3+} to the oxygen and from the O^{2-} to the neighboring Mn^{4+}. Such hopping is greatest if the spins of the two d shells are parallel, hence the lowest energy of the system at low temperature is obtained for a ferromagnetic arrangement of the two manganese ions. In that case, the configurations Mn^{3+}-O-Mn^{4+} and Mn^{4+}-O-Mn^{3+} are degenerate.

These interactions can account for the observations regarding Mn-Mn coupling [11]: antiferromagnetic between two Mn^{4+} (covalent), ferromagnetic between a Mn^{3+} and a Mn^{4+} (double exchange) and antiferromagnetic (covalent) or ferromagnetic (semicovalent) between Mn^{3+}. With these rules, Goodenough rationalized the crystallographic and magnetic arrangements, associated with the different possible charge orderings. Typical charge-ordered arrangements are obtained for special ratios of Mn^{3+} to Mn^{4+} ions.

(a) Pure $CaMnO_3$ (100% Mn4+) contains only Mn^{4+} ions which couple antiferromagnetically. The order is then nearest-neighbor antiferromagnetism (G type) with no lattice distortion.

(b) For 75% Mn^{4+}, the arrangement is one of planes of Mn^{4+} alternating with planes containing equal proportions of Mn^{3+} and Mn^{4+}. In these planes, the ordering is

purely antiferromagnetic but along chains running in the c direction, the coupling is on average ferromagnetic (some Mn^{4+}-Mn^{4+} bonds being mismatched). This is C-type order, where ferromagnetic chains are coupled antiferromagnetically.

(c) The 50% Mn^{4+} case is more complex since three possible ordered bond arrangements are electrostatically equivalent. The minimum elastic energy, however, corresponds to a CE-type ordering of semicovalent bonds.

(d) At 30% Mn^{4+}, the magnetic order is ferromagnetic with a moment almost equal to the spin only value. This is due to the double exchange between Mn^{3+} and Mn^{4+}. Goodenough explained why the best ferromagnetic phase is not reached at 50% Mn^{4+}. The double-exchange interaction is optimized for a disordered composition which has the largest number of Mn^{3+} ions with one and only one Mn^{4+} near neighbor. The corresponding Mn^{4+} content is 31%. It is interesting to note that, for an ordered lattice, the optimum value would be 25% [29].

(e) Pure $LaMnO_3$ (0% Mn^{4+}) is an A-type antiferromagnet where all the bonds in the c direction are covalent ($J_2 < 0$), while the in-plane orbital arrangement maximizes the number of ferromagnetic semicovalent bonds ($J_1 > 0$). The magnetic structure is that of ferromagnetic planes coupled antiferromagnetically with the c axis shorter than a or b (the covalent bond is short). Goodenough predicted that the semicovalent bonds would order below a certain temperature to form the O′ structure, reducing the elastic energy associated with the different Mn-Mn separations. This semicovalent bond ordering

(orbital ordering) is a cooperative phenomenon that occurs well above the Curie temperature.

Transitions between these different magnetic phases are continuous. They are realized either by inhomogeneous mixing in a two-phase region or by a homogeneous progressive magnetic transition involving canting, as in the low x region. A short summary of the interplay between spin, charge and orbital degrees of freedom in magnetic oxides with reference to the theoretical literature has been written by Khomskii and Sawatzky [30].

It is worth emphasizing that double exchange is not indispensable for ferromagnetism in manganites, as shown by the example of $(La_{1-x}Ba_x)$-$(Mn_{1-x}Ti_x)MnO_3$ which is ferromagnetic and yet contains no Mn^{4+} [25], or the net ferromagnetic exchange interaction in $LaMnO_3$. Exchange constants have been estimated for the insulating end members by Millis [31], using standard superexchange arguments.

Extensive neutron measurements have also been carried out on the $(Pr_{1-x}A_x)MnO_3$ systems (A= Ca, Ba, Sr, Na or K) by a Czech group. The full range of solid solutions exists only for A = Ca but when A = Sr or Ba, solid solubility extends to x = 0.5 or x = 0.4 respectively [32]. Their work on the $(Pr_{1-x}Ca_x)MnO_3$ system extended the early study of Wollan and Koehler on the $(La_{1-x}Ca_x)MnO_3$ system to higher temperatures which allowed them to examine the charge ordering transitions. Salient features of crystallographic and magnetic structures are presented on Figure 1.16.

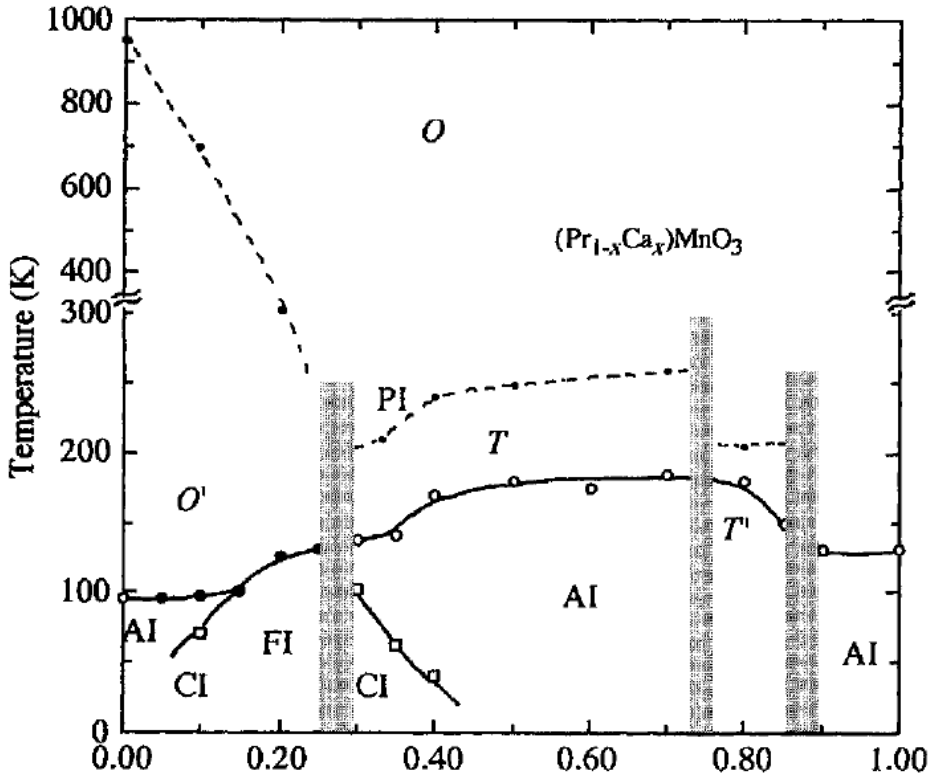

Figure 1.16 Crystallographic and magnetic order in the $(Pr_{1-x}Ca_x)MnO_3$ system.

The low-temperature phases in $(Pr_{1-x}Ca_x)MnO_3$ can be divided into four compositional regions, depending on the ordering of the Mn^{3+} ions and their d_{z^2} orbitals.

(a) $0 < x < 0.2$. Antiferromagnetism of type A for the end member occurs where moments in the (010) direction gradually cant as holes are added (x increasing). For x = 0.1, at 4.2 K, the moments are along the (110) directions. Above a transition temperature of 70 K, the compound becomes ferromagnetic with its easy axis along the (010) direction. This transition, predicted by deGennes, was observed for the first time in this system. The magnetic ordering temperature is reached at 100 K. Another interesting

result in the x = 0.1 sample is that praseodymium ions order below 30-40 K contributing by 0.5 μ_B per praseodymium ion to the ferromagnetic component of the moment of the manganese ions. This is in contrast with the result for the end-member where no order of the praseodymium was detected down to 1.5 K.

(b) 0.2 < x < 0.3. This is the region of ferromagnetism. The manganese moment reaches 3.75 μ_B, which is close to the expected spin-only value. The magnetic easy axis is along the (010) direction.

(c) 0.3 < x < 0.75. The charge ordering throughout this range is most fully developed in the x 0.5 compound which is antiferromagnetic of type CE with moments along the (010) direction. Adding holes or electrons in this structure initially has the same effect. It produces a canting between antiferromagnetic layers. On one side, this canting leads over to the ferromagnetic region near x 0.3 where the CE structure is still present in (001) planes with a ferromagnetic component along the 001 direction. There is a transition between antiferromagnetic and canted states when 0.3 < x < 0.4 [33, 34]. On the other side, the canting leads to the antiferromagnetic C structure for x 0.75. An interesting feature of the $(Pr_{0.3}Ca_{0.7})MnO_3$ compound is the presence of satellite lines in the neutron diffraction pattern which indicates a non-commensurate spiral structure along the (010) axis with period 3.5 nm. It was suggested that the long range interaction causing it to appear is antiferromagnetic superexchange along in-plane diagonals (Mn-O-Mn-O-Mn) which couples manganese neighbors in fourth order [35]. This resembles the situation found in other perovskites such as $SrFeO_3$[36].

(d) $0.75 < x < 1$. This is the two-phase region where the C type coexists with the G-type nearest-neighbor antiferromagnetism of the x 1 end member. Canting is not favored in G-type structures, where electrons are localized [8].

Even though the magnetic properties of the $(La_{1-x}Ca_x)MnO_3$ and $(Pr_{1-x}Ca_x)MnO_3$ systems are similar, there is an important difference in electronic structure that must be emphasized. A ferromagnetic phase is obtained for x 0.3 in $(La_{1-x}Ca_x)MnO_3$ and for x closer to 0.2 for $(Pr_{1-x}Ca_x)MnO_3$ but the latter does not have the high conductivity associated with ferromagnetism in a cubic or rhombohedral phase. The fact that the transport properties are so different in the two systems (there is no maximum in R(T) curves for $(Pr_{1-x}Ca_x)MnO_3$ for $x \approx 0.2$) reflects the importance of the tolerance factor t′ and related structural details such as Mn-O-Mn bond angle for the double-exchange mechanism.

$La_{5/8-y}Pr_yCa_{3/8}MnO_3$ can be considered as a mixture of $(La_{1-x}Ca_x)MnO_3$ and $(Pr_{1-x}Ca_x)MnO_3$. The Ca concentration is chosen to be 3/8 to maximize the Tc. A few striking features can be seen in the temperature (T) dependence of resistivity (ρ) and MR of $La_{5/8-y}Pr_yCa_{3/8}MnO_3$ shown in Figure 1.17. First, Tc, determined by the maximum slope of the sudden ρ drop, decreases gradually with increasing y (for $0.25 > y > 0$), but Tco (charge ordering temperature $\approx$ 210 K)— which is observed only for $y \geq 0.3$ and characterized by ρ upturn—does not depend on y. Tc is strongly reduced from ,210K for $y = 0.25$ down to ~80 K for $y = 0.3$, clearly indicating the competition between the two dominant FM and CO ground states in the manganites. The most striking aspect, however,

is that enormously large residual ρ (for example, $\rho_0 \approx 2\times10^4\,\Omega cm$ for y = 0.4), much larger than the Mott metallic limit, develops for large y even though the T dependence of ρ is metallic-like below Tc, suggesting percolative conduction through metallic regions embedded in insulating regions. A significant hysteresis develops when Tc becomes lower than Tco < 210K (Fig. 1.17), consistent with the first-order-type transition in a system with two-phase coexistence. Even for 0.275 > y > 0.2 where no CO transition is indicated in ρ(T), the ρ hysteresis is clearly observable, and this hysteresis behavior appears to correlate with a broad 'hump' far below Tc which exists for y down to 0.

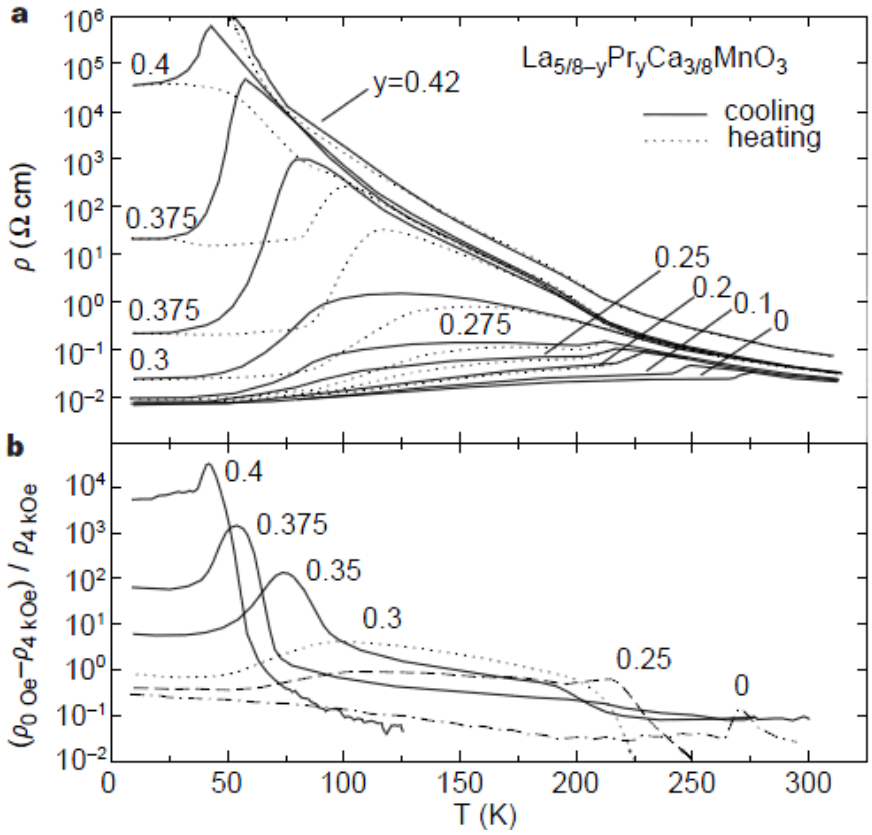

Figure 1.17 Transport and magnetic properties of $La_{5/8-y}Pr_yCa_{3/8}MnO_3$ as a function of temperature and y. (a) T dependence of ρ. Both cooling (solid lines) and heating (dotted lines) curves are shown. (b) Magnetoresistance of representative specimens in 4 kOe with field cooling.

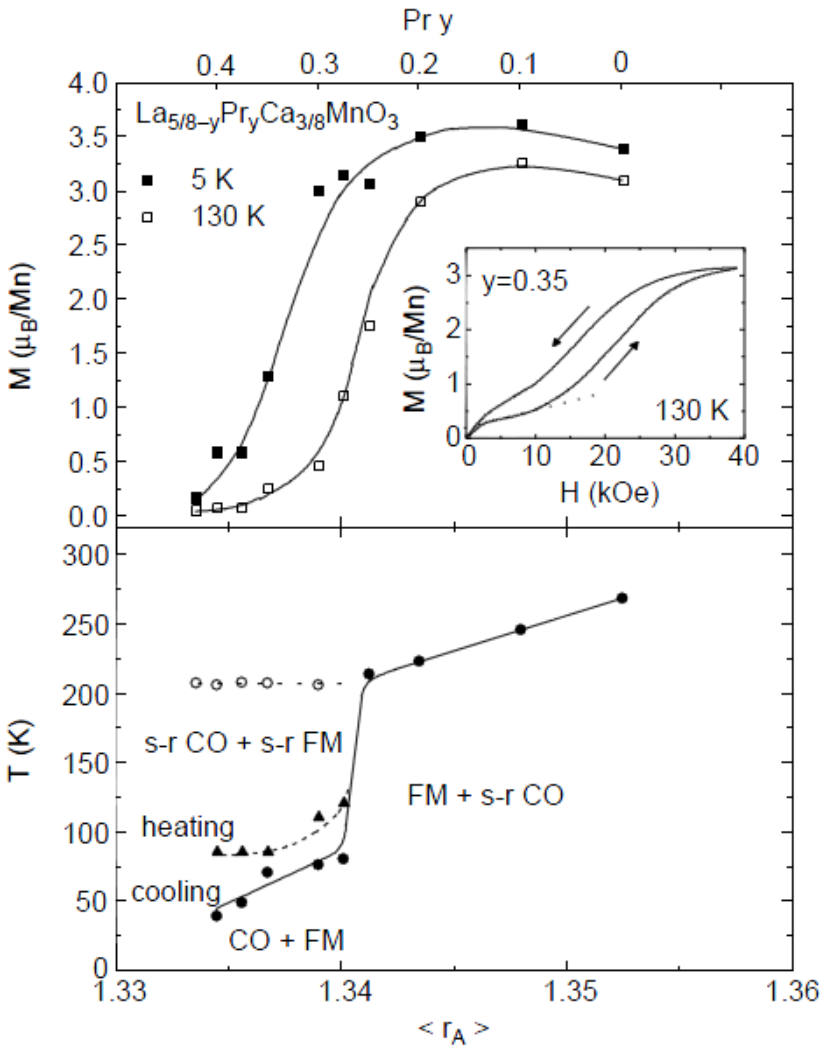

Figure 1.18 Ferromagnetically-ordered moment and the phase diagram of $La_{5/8-y}Pr_yCa_{3/8}MnO_3$ as a function of average ionic radius $\langle r_A \rangle$ or y.

The MR of $La_{5/8-y}PryCa_{3/8}MnO_3$ was measured in a magnetic field of 4 kOe, which is high enough to orient magnetic domains but low enough not to affect the CO phase (Figure 1.17 b). The MR peaks near Tc result from the shift of TC to higher T by applying field, and the MR becomes ‘‘colossal’’ in low-TC materials (particularly for 0.4 > y > 0.25). One noticeable feature is the existence of a plateau in the MR for 0.375 > y > 0.25 at 210K > T > 80 K; this MR plateau is also associated with the two-phase

coexistence. The FM behavior at 130 K, between Tco and TC, for y = 0:35 is clearly visible in the magnetization, M(H), curve (Figure 1.18 inset), and the change of this FM component at 130 K with y is shown in the top panel of Figure 1.18. The persistence of the FM component at 130 K for y up to 0.42 indicates the two-phase coexistence even for Tco > T > TC. The saturation moment (Ms) at 5K in the same panel decreases sharply with y (>0.3) where TC is suppressed below 80 K, supporting the suggestion above that two phases coexist for y > 0.3 below Tc. We note that Ms for 0.3 > y > 0, including y = 0, at 5 K is also slightly reduced from the optimum value of,3.9–4 μ_B in $(La_{1-x}Sr_x)MnO_3$ (x $\approx$ 3=8; Tc $\approx$ 375 K). This reduced Ms suggests the presence of a small amount of CO phase even for y = 0.

1.2 Experimental Method

In this experiment, a single crystal $La_{0.25}Pr_{0.375}Ca_{0.375}MnO_3$ was used. The Ca concentration was chosen to be 3/8 where the FM Tc is maximized. Based on the phase diagram from [21], the $La_{5/8-y}Pr_yCa_{3/8}MnO_3$ system experiences a significant phase transition near y = 0.3. Below 0.29, the system was dominated by FM, with minor existence of short-ranged CO-state. Above 0.3, the CO-state rapidly takes over the place and keeps getting strengthened with the increase of Pr concentration. The sample with the composition of $La_{0.25}Pr_{0.375}Ca_{0.375}MnO_3$, sits in the close left side to the y = 0.3 composition. Since the pressure effect will favor the FM state, it could be expected that while a certain amount of pressure is applied, the system might shift to the FM dominated

phase, because the system is near the transition edge and therefore is volatile. This kind of phase transition could be characterized by the magnetic susceptibility and electrical resistivity due to the different nature of the CO and FM states.

1.2.1 M-cell Measurement

M-cell (see Figure 1.19) was utilized to help measuring the pressurized magnetization of a 0.1 gram $La_{0.25}Pr_{0.375}Ca_{0.375}MnO_3$ single crystal. The position and orientation of the crystal is fixed in the pressure cell and the measurement is along the C-axis direction. A certain amount of Sn is also loaded to be the pressure indicator. Liquid transmitting medium is then added into the capsule before it was sealed by PTFE plug. The M-cell was assembled and pressurized by 10 ton hydraulic press. The pressure was first applied following a loading curve, and then verified by the Sn superconductor temperature change which varies with pressure change. During the measurement a magnetic field of 2 kOe was applied, which is high enough to align the FM domains without influencing the CO insulating phases. The magnetic susceptibility was measured under field-cooled cooling, field-cooled warming and zero-field-cooled warming conditions.

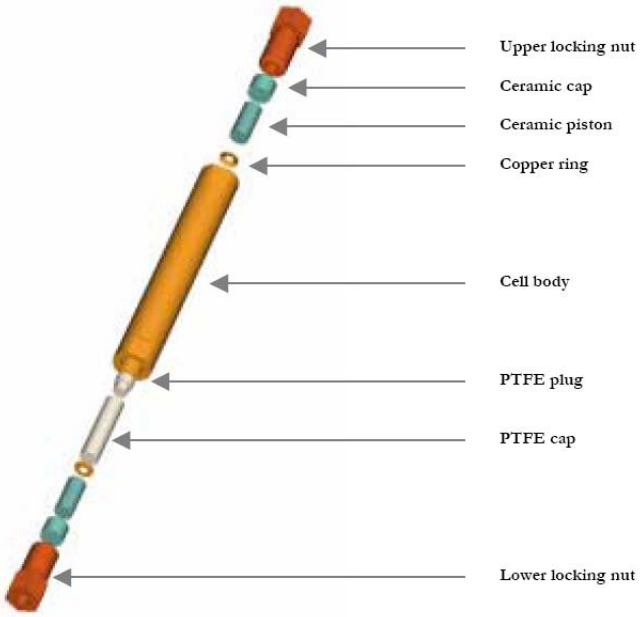

Figure 1.19 The configuration of M-Cell.

1.2.2 P-cell Measurement

P-cell was used to assist to measure the electrical resistivity of the identical sample used in magnetic susceptibility measurement (see Fig. 1.20). The dimension of the sample is 2 mm (a) * 4 mm (b)* 1 mm (c). Two contacts are made on a-b plane and the other two contacts are made on the a-c side plane, all the wires are perpendicular to the b plane. Transmitting liquid is added into the capsule before it is sealed. The whole cell is then assembled and the other side of the wires through the feed-through is soldered to a puck. The cell is then pressurized and the measurements were carried out inside a PPMS system.

The resistivity was measured under cooling and warming conditions.

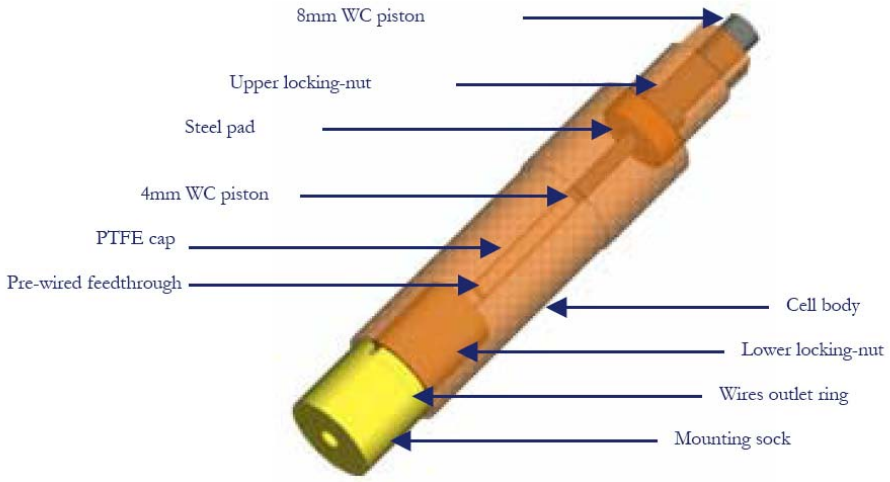

Figure 1.20 Configuration of P-cell.

1.3 Result and Discussion

The magnetic susceptibility was measured under field-cooled cooling (FCC), field-cooled warming (FCW) and zero-field-cooled warming (ZFC-W) conditions and the data are shown in Figure 1.21, Figure 1.22, and Figure 1.23. For the cooling process, the system is mainly in non-magnetic CO-state at higher temperature. When the temperature goes down, the system changes into FM metallic states and the magnetic susceptibility start to increase. The warming process is similar to the cooling process but the system was in FM metallic states before CO-state. The temperature at which the CO-state and FM converts into each other is marked as Tc. 150 K Tc increase was observed during the cooling process, and 100 K Tc increase was observed in the warming process, with only up to 11 kbar pressure. The M/H versus temperature plots vary from each other, mainly because the sample is at different original states while the measurement starts under

different procedures. In the field-cooled cooling measurement, steps can be observed between 130 K and 200 K, indicating the existence of secondary phase transitions. This phase transition, which becomes significant starting from 9 kbar, and almost saturated at 11 kbar, is mostly due to the small amount of CAF phase getting released under a certain amount of pressure. In both the field-cooled warming and zero-field-cooled warming measurements, some step-like secondary transitions can be observed around 30 K while the system is under zero or low pressure. This phenomenon is called the "reentrance" of CO-state [37], originated from the strain glass nature of the system while the measurement started. Measurement was also done during the unloading pressure process. The plot in the pressure-unloading process is almost identical to the similar pressure point during the pressure-loading process, which indicates that the pressure induced phase transition is reversible.

Similar to the magnetic susceptibility result, 150 K and 100 K Tc increase was observed for resistivity measurements during cooling and warming process, respectively (see Figure 1.24, Figure 1.25). This is expected because the FM state is metallic and is more conductive, and CO-state is insulating and is less conductive.

Usually the pressure induced phase transition Tc changes only at an order of 1K per kbar. Here we had roughly 12 K per kbar with a linear relationship to the pressure within 12 kbar. Comparing with the pressure effect in the similar system, where $Sm_{0.5}Ba_{0.5}MnO_3$ shows around 1 K per kbar and $La_{0.85}MnO_{3-\delta}$ shows around 1.43 K per

kbar, our experiment is still about 10 times more sensitive to pressure, which could be applied as pressure sensor in future.

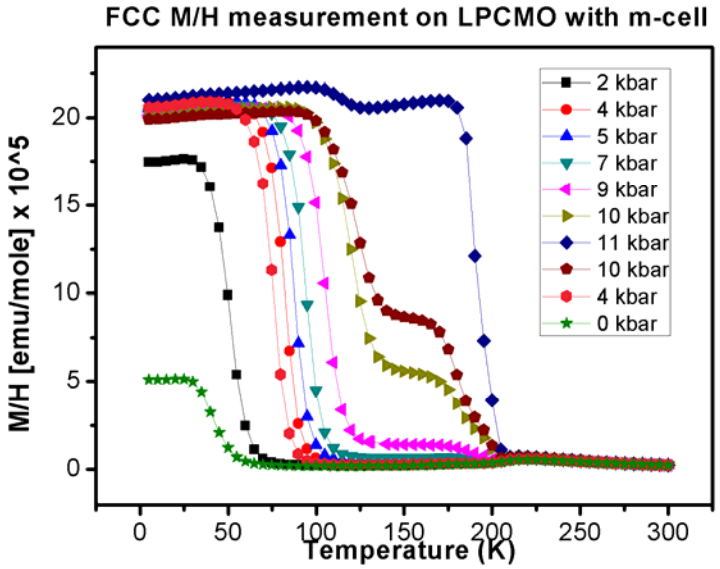

Figure 1.21 FCC M/H measurements on LPCMO with m-cell.

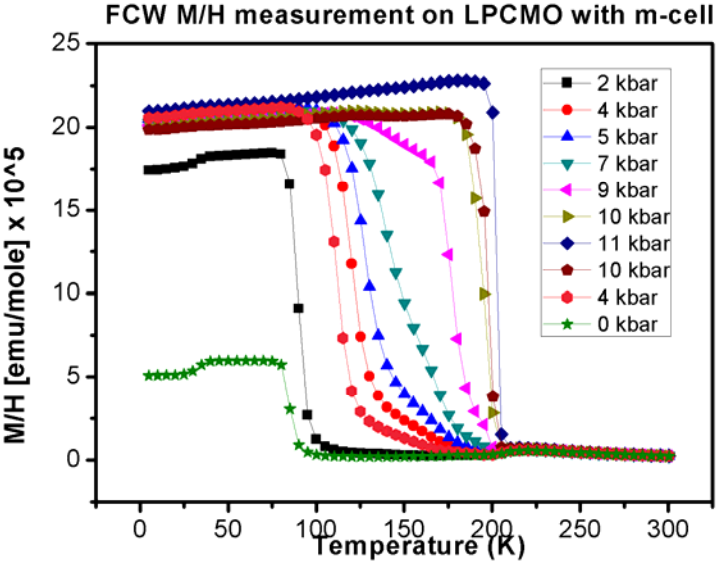

Figure 1.22 FCW M/H measurements on LPCMO with m-cell.

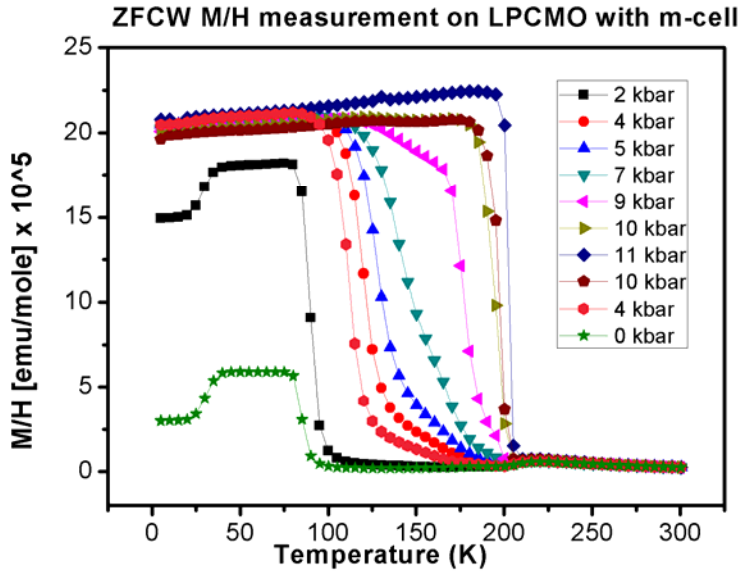

Figure 1.23 ZFC-W M/H measurements on LPCMO with m-cell.

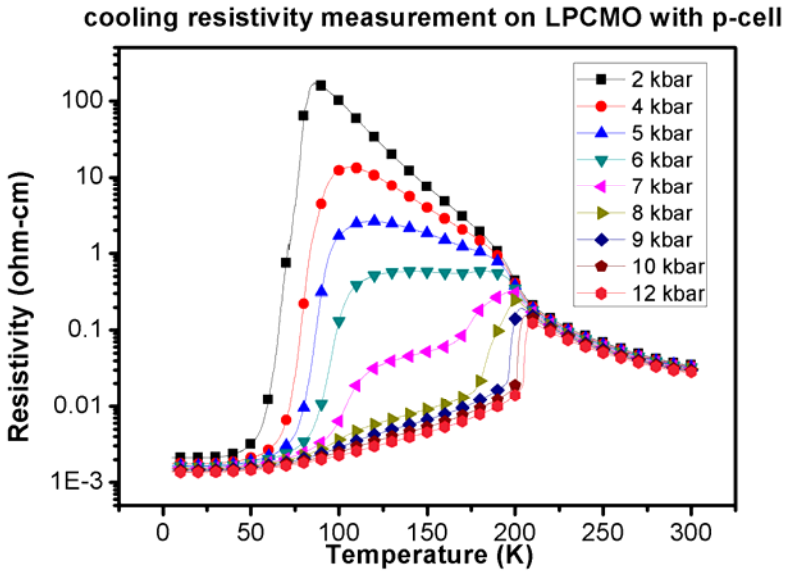

Figure 1.24 Cooling resistivity measurements on LPCMO with p-cell.

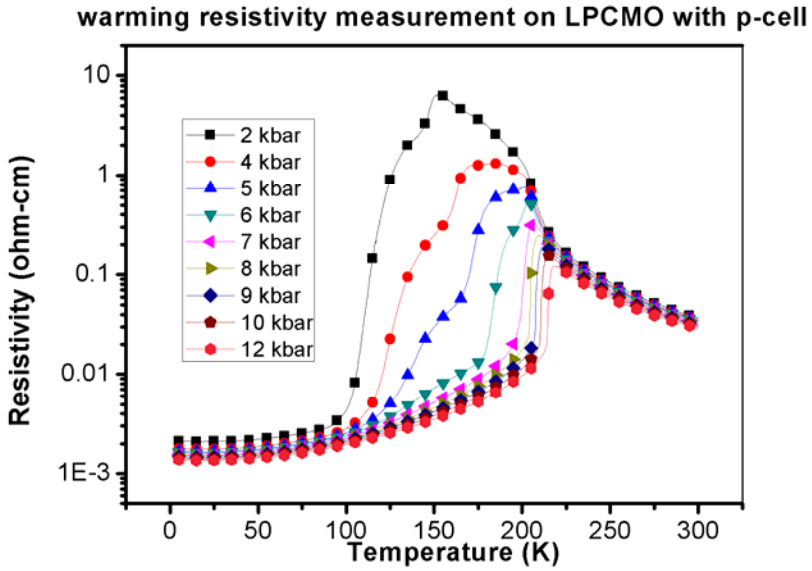

Figure 1.25 Warming resistivity measurements on LPCMO with p-cell.

1.4 Conclusion

In conclusion, M-cell and P-cell were used to apply pressure on $La_{0.25}Pr_{0.375}Ca_{0.375}MnO_3$ single crystal. Phase transition between FM metallic phase and CO insulating phase was observed. The transition temperature Tc was increased by at least 100 K under only up to 12 kbar pressure. This pressure induced transition temperature change is more than 10 times larger than the effects discovered in the similar manganese oxide compounds and has the potential to be applied for pressure sensor in future.

CHAPTER 2

CRYSTAL FIELD EXCITATIONS IN THE RAMAN SPECTRA OF $FeSe_{1-x}$

2.1 Introduction

2.1.1 Superconductivity

Superconductivity was discovered in 1911 by Heike Kamerlingh Onnes, who was studying the resistance of solid mercury at cryogenic temperatures using the recently-discovered liquid helium as a refrigerant [38]. At the temperature of 4.2 K, he observed that the resistance abruptly disappeared. In subsequent decades, superconductivity was found in several other materials. In 1913, lead was found to superconduct at 7 K, and in 1941 niobium nitride was found to superconduct at 16 K.

The next important step in understanding superconductivity occurred in 1933, when Meissner and Ochsenfeld discovered that superconductors expelled applied magnetic fields, a phenomenon which has come to be known as the Meissner effect. In 1935, F. and H. London showed that the Meissner effect was a consequence of the minimization of the electromagnetic free energy carried by superconducting current.

In 1950, the phenomenological Ginzburg-Landau theory of superconductivity was devised by Landau and Ginzburg. This theory, which combined Landau's theory of second-order phase transitions with a Schrödinger-like wave equation, had great success in explaining the macroscopic properties of superconductors. In particular, Abrikosov showed that Ginzburg-Landau theory predicts the division of superconductors into the

two categories now referred to as Type I and Type II. Abrikosov and Ginzburg were awarded the 2003 Nobel Prize for their work (Landau had received the 1962 Nobel Prize for other work, and died in 1968).

Also in 1950, Maxwell and Reynolds et al. found that the critical temperature of a superconductor depends on the isotopic mass of the constituent element. This important discovery pointed to the electron-phonon interaction as the microscopic mechanism responsible for superconductivity.

The complete microscopic theory of superconductivity was finally proposed in 1957 by Bardeen, Cooper and Schrieffer. This BCS theory explained the superconducting current as a superfluid of Cooper pairs, pairs of electrons interacting through the exchange of phonons. For this work, the authors were awarded the Nobel Prize in 1972.

The BCS theory was set on a firmer footing in 1958, when Bogolyubov showed that the BCS wavefunction, which had originally been derived from a variational argument, could be obtained using a canonical transformation of the electronic Hamiltonian. In 1959, Lev Gor'kov showed that the BCS theory reduced to the Ginzburg-Landau theory close to the critical temperature.

In 1962, the first commercial superconducting wire, a niobium-titanium alloy, was developed by researchers at Westinghouse, allowing the construction of the first practical superconducting magnets. In the same year, Josephson made the important theoretical prediction that a supercurrent can flow between two pieces of superconductor separated by a thin layer of insulator. This phenomenon, now called the Josephson effect,

is exploited by superconducting devices such as SQUIDs. It is used in the most accurate available measurements of the magnetic flux quantum $\Phi_0 = \frac{h}{2e}$, and thus (coupled with the quantum Hall resistivity) for Planck's constant h. Josephson was awarded the Nobel Prize for this work in 1973.

In 2008, it was discovered that the same mechanism that produces superconductivity could produce a superinsulator state in some materials, with almost infinite electrical resistance.

Superconducting magnets are some of the most powerful electromagnets known. They are used in MRI and NMR machines, mass spectrometers, and the beam-steering magnets used in particle accelerators. They can also be used for magnetic separation, where weakly magnetic particles are extracted from a background of less or non-magnetic particles, as in the pigment industries.

In the 1950s and 1960s, superconductors were used to build experimental digital computers using cryotron switches. More recently, superconductors have been used to make digital circuits based on rapid single flux quantum technology and RF and microwave filters for mobile phone base stations.

Superconductors are used to build Josephson junctions which are the building blocks of SQUIDs (superconducting quantum interference devices), the most sensitive magnetometers known. SQUIDs are used in scanning SQUID microscopes and Magnetoencephalography. Series of Josephson devices are used to realize the SI volt. Depending on the particular mode of operation, a Josephson junction can be used as a

photon detector or as a mixer. The large resistance change at the transition from the normal- to the superconducting state is used to build thermometers in cryogenic micro-calorimeter photon detectors.

Other early markets are arising where the relative efficiency, size and weight advantages of devices based on high-temperature superconductivity outweigh the additional costs involved.

Promising future applications include high-performance smart grid, electric power transmission, transformers, power storage devices, electric motors (e.g. for vehicle propulsion, as in vactrains or maglev trains), magnetic levitation devices, fault current limiters, nanoscopic materials such as buckyballs, nanotubes, composite materials and superconducting magnetic refrigeration. However, superconductivity is sensitive to moving magnetic fields so applications that use alternating current (e.g. transformers) will be more difficult to develop than those that rely upon direct current.

2.1.2 Elementary Properties of Superconductors

Most of the physical properties of superconductors vary from material to material, such as the heat capacity and the critical temperature, critical field, and critical current density at which superconductivity is destroyed.

On the other hand, there is a class of properties that are independent of the underlying material. For instance, all superconductors have exactly zero resistivity to low applied currents when there is no magnetic field present or if the applied field does not

exceed a critical value. The existence of these "universal" properties implies that superconductivity is a thermodynamic phase, and thus possesses certain distinguishing properties which are largely independent of microscopic details.

2.1.2.1 Zero electrical DC resistance

Superconductors are also able to maintain a current with no applied voltage whatsoever, a property exploited in superconducting electromagnets such as those found in MRI machines. Experiments have demonstrated that currents in superconducting coils can persist for years without any measurable degradation. Experimental evidence points to a current lifetime of at least 100,000 years. Theoretical estimates for the lifetime of a persistent current can exceed the estimated lifetime of the universe, depending on the wire geometry and the temperature.

In a normal conductor, an electrical current may be visualized as a fluid of electrons moving across a heavy ionic lattice. The electrons are constantly colliding with the ions in the lattice, and during each collision some of the energy carried by the current is absorbed by the lattice and converted into heat, which is essentially the vibrational kinetic energy of the lattice ions. As a result, the energy carried by the current is constantly being dissipated. This is the phenomenon of electrical resistance.

The situation is different in a superconductor. In a conventional superconductor, the electronic fluid cannot be resolved into individual electrons. Instead, it consists of bound pairs of electrons known as Cooper pairs. This pairing is caused by an attractive

force between electrons from the exchange of phonons. Due to quantum mechanics, the energy spectrum of this Cooper pair fluid possesses an energy gap, meaning there is a minimum amount of energy ΔE that must be supplied in order to excite the fluid. Therefore, if ΔE is larger than the thermal energy of the lattice, given by kT, where k is Boltzmann's constant and T is the temperature, the fluid will not be scattered by the lattice. The Cooper pair fluid is thus a superfluid, meaning it can flow without energy dissipation.

In a class of superconductors known as type II superconductors, including all known high-temperature superconductors, an extremely small amount of resistivity appears at temperatures not too far below the nominal superconducting transition when an electrical current is applied in conjunction with a strong magnetic field, which may be caused by the electrical current. This is due to the motion of vortices in the electronic superfluid, which dissipates some of the energy carried by the current. If the current is sufficiently small, the vortices are stationary, and the resistivity vanishes. The resistance due to this effect is tiny compared with that of non-superconducting materials, but must be taken into account in sensitive experiments. However, as the temperature decreases far enough below the nominal superconducting transition, these vortices can become frozen into a disordered but stationary phase known as a "vortex glass" (Figure 2.1). Below this vortex glass transition temperature, the resistance of the material becomes truly zero.

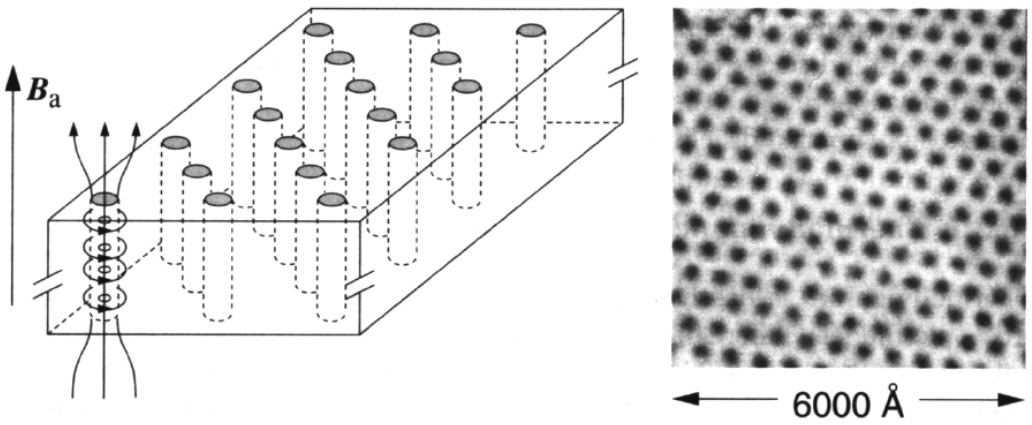

Figure 2.1 Vortices (dark regions) in a type-II superconductor.

2.1.2.2 Superconducting Phase Transition

In superconducting materials, the characteristics of superconductivity appear when the temperature T is lowered below a critical temperature Tc. The value of this critical temperature varies from material to material. Conventional superconductors usually have critical temperatures ranging from around 20 K to less than 1 K. Solid mercury, for example, has a critical temperature of 4.2 K. As of 2009[update], the highest critical temperature found for a conventional superconductor is 39 K for magnesium diboride (MgB2) [39] although this material displays enough exotic properties that there is some doubt about classifying it as a "conventional" superconductor [40]. Cuprate superconductors can have much higher critical temperatures: YBa2Cu3O7, one of the first cuprate superconductors to be discovered, has a critical temperature of 92 K, and mercury-based cuprates have been found with critical temperatures in excess of 130 K. The explanation for these high critical temperatures remains unknown. Electron pairing

due to phonon exchanges explains superconductivity in conventional superconductors, but it does not explain superconductivity in the newer superconductors that have a very high critical temperature.

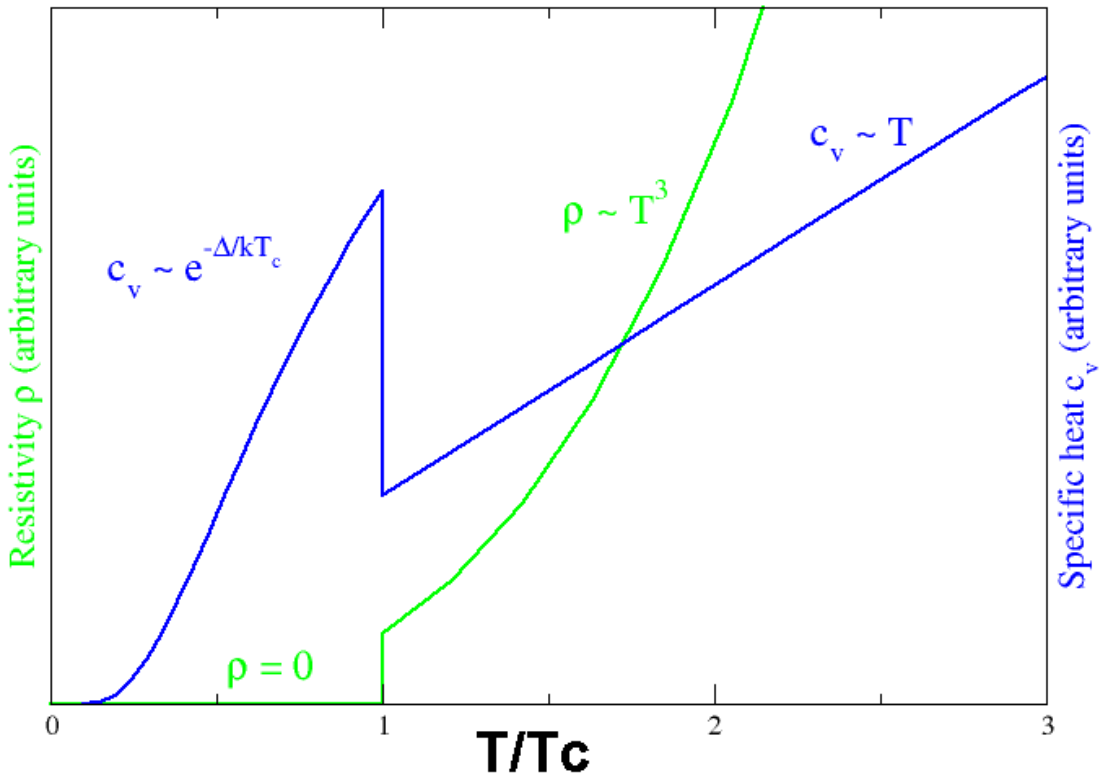

Figure 2.2 Behavior of heat capacity (c_v, blue) and resistivity (ρ, green) at the superconducting phase transition.

Similarly, at a fixed temperature below the critical temperature, superconducting materials cease to superconduct when an external magnetic field is applied which is greater than the critical magnetic field. This is because the Gibbs free energy of the superconducting phase increases quadratically with the magnetic field while the free energy of the normal phase is roughly independent of the magnetic field. If the material

superconducts in the absence of a field, then the superconducting phase free energy is lower than that of the normal phase and so for some finite value of the magnetic field (proportional to the square root of the difference of the free energies at zero magnetic field) the two free energies will be equal and a phase transition to the normal phase will occur. More generally, a higher temperature and a stronger magnetic field lead to a smaller fraction of the electrons in the superconducting band and consequently a longer London penetration depth of external magnetic fields and currents. The penetration depth becomes infinite at the phase transition.

The onset of superconductivity is accompanied by abrupt changes in various physical properties, which is the hallmark of a phase transition. For example, the electronic heat capacity is proportional to the temperature in the normal (non-superconducting) regime (Figure 2.2). At the superconducting transition, it suffers a discontinuous jump and thereafter ceases to be linear. At low temperatures, it varies instead as $e^{-\alpha /T}$ for some constant α. This exponential behavior is one of the pieces of evidence for the existence of the energy gap.

The order of the superconducting phase transition was long a matter of debate. Experiments indicate that the transition is second-order, meaning there is no latent heat. However in the presence of an external magnetic field there is latent heat, as a result of the fact that the superconducting phase has lower entropy below the critical temperature than the normal phase. It has been experimentally demonstrated [41] that, as a

consequence, when the magnetic field is increased beyond the critical field, the resulting phase transition leads to a decrease in the temperature of the superconducting material.

Calculations in the 1970s suggested that it may actually be weakly first-order due to the effect of long-range fluctuations in the electromagnetic field. In the 1980s it was shown theoretically with the help of a disorder field theory, in which the vortex lines of the superconductor play a major role, that the transition is of second order within the type II regime and of first order (i.e., latent heat) within the type I regime, and that the two regions are separated by a tricritical point [42]. The results were confirmed by Monte Carlo computer simulations [43].

2.1.2.3 Meissner Effect

When a superconductor is placed in a weak external magnetic field H, and cooled below its transition temperature, the magnetic field is ejected. The Meissner effect (Figure 2.3) does not cause the field to be completely ejected but instead the field penetrates the superconductor but only to a very small distance, characterized by a parameter λ, called the London penetration depth, decaying exponentially to zero within the bulk of the material. The Meissner effect, is a defining characteristic of superconductivity. For most superconductors, the London penetration depth is on the order of 100 nm.

The Meissner effect is sometimes confused with the kind of diamagnetism one would expect in a perfect electrical conductor: according to Lenz's law, when a changing magnetic field is applied to a conductor, it will induce an electrical current in the

conductor that creates an opposing magnetic field. In a perfect conductor, an arbitrarily large current can be induced, and the resulting magnetic field exactly cancels the applied field.

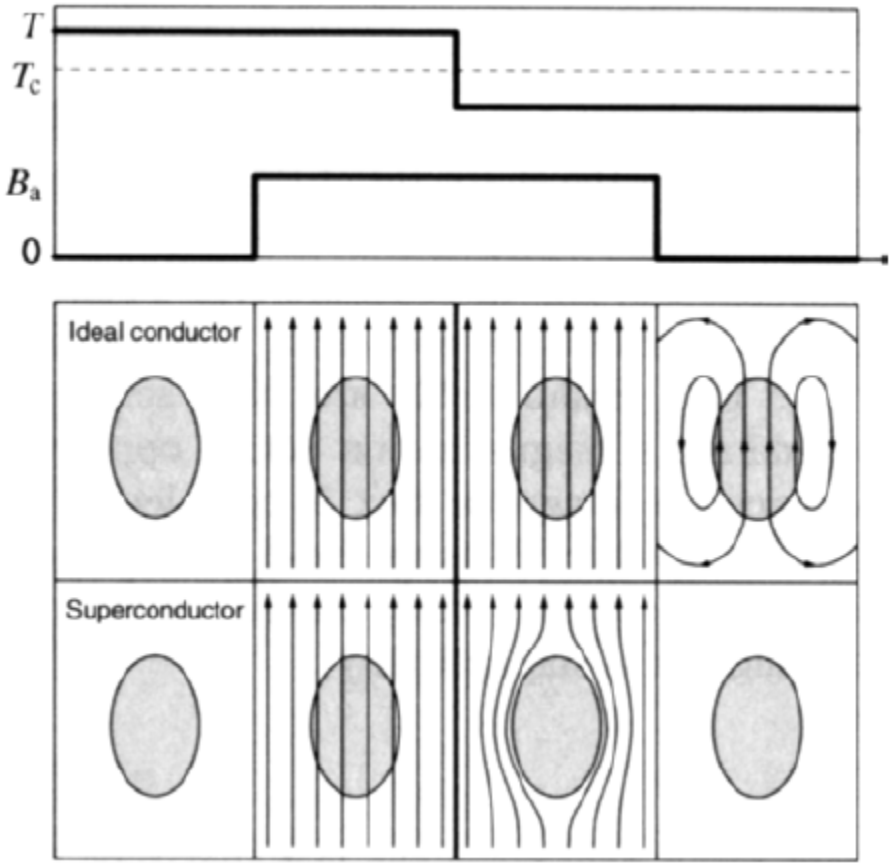

Figure 2.3 The Meissner effect.

The Meissner effect is distinct from this—it is the spontaneous expulsion which occurs during transition to superconductivity. Suppose we have a material in its normal state, containing a constant internal magnetic field. When the material is cooled below the critical temperature, we would observe the abrupt expulsion of the internal magnetic field, which we would not expect based on Lenz's law.

The Meissner effect was given a phenomenological explanation by the brothers Fritz and Heinz London, who showed that the electromagnetic free energy in a superconductor is minimized provided

$$\nabla^2 H = \lambda^{-2} H \tag{2.1}$$

where H is the magnetic field and λ is the London penetration depth.

This equation, which is known as the London equation, predicts that the magnetic field in a superconductor decays exponentially from whatever value it possesses at the surface.

A superconductor with little or no magnetic field within it is said to be in the Meissner state. The Meissner state breaks down when the applied magnetic field is too large. Superconductors can be divided into two classes according to how this breakdown occurs. In Type I superconductors, superconductivity is abruptly destroyed when the strength of the applied field rises above a critical value Hc. Depending on the geometry of the sample, one may obtain an intermediate state [44] consisting of a baroque pattern [45] of regions of normal material carrying a magnetic field mixed with regions of superconducting material containing no field. In Type II superconductors, raising the applied field past a critical value Hc1 leads to a mixed state (also known as the vortex state) in which an increasing amount of magnetic flux penetrates the material, but there remains no resistance to the flow of electrical current as long as the current is not too large. At a second critical field strength Hc2, superconductivity is destroyed. The mixed state is actually caused by vortices in the electronic superfluid, sometimes called fluxons

because the flux carried by these vortices is quantized. Most pure elemental superconductors, except niobium, technetium, vanadium and carbon nanotubes, are Type I, while almost all impure and compound superconductors are Type II.

2.1.2.4 London moment

Conversely, a spinning superconductor generates a magnetic field, precisely aligned with the spin axis. The effect, the London moment, was put to good use in Gravity Probe B. This experiment measured the magnetic fields of four superconducting gyroscopes to determine their spin axes. This was critical to the experiment since it is one of the few ways to accurately determine the spin axis of an otherwise featureless sphere.

2.1.2.5 Josephson Effect

A Josephson junction (Figure 2.4) is a type of electronic circuit capable of switching at very high speeds when operated at temperatures approaching absolute zero [46]. Named for the British physicist who designed it, a Josephson junction exploits the phenomenon of superconductivity, the ability of certain materials to conduct electric current with practically zero resistance. Josephson junctions are used in certain specialized instruments such as highly-sensitive microwave detectors, magnetometers, and QUIDs.

A Josephson junction is made up of two superconductors, separated by a nonsuperconducting layer so thin that electrons can cross through the insulating barrier. The flow of current between the superconductors in the absence of an applied voltage is

called a Josephson current, and the movement of electrons across the barrier is known as Josephson tunneling. Two or more junctions joined by superconducting paths form what is called a Josephson interferometer.

While researching superconductivity, Brian David Josephson studied the properties of a junction between two superconductors. Following up on earlier work by Leo Esaki and Ivar Giaever, he demonstrated that in a situation when there is electron flow between two superconductors through an insulating layer (in the absence of an applied voltage), and a voltage is applied, the current stops flowing and oscillates at a high frequency.

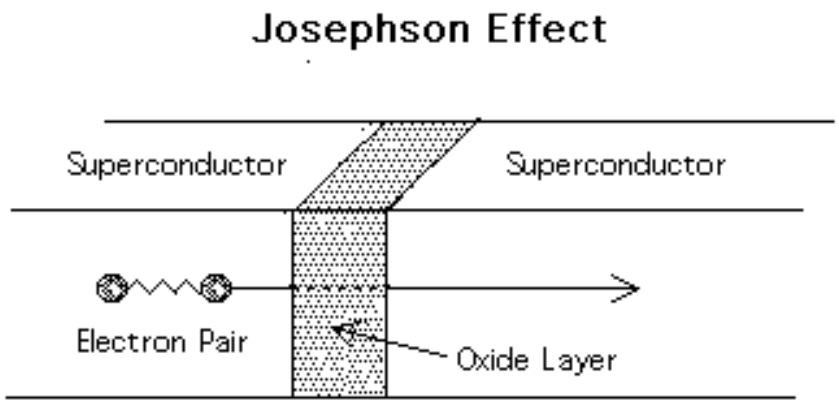

Figure 2.4 The Josephson effect.

The Josephson effect is influenced by magnetic fields in the vicinity, a capacity that enables the Josephson junction to be used in devices that measure extremely weak magnetic fields, such as superconducting quantum interference devices (SQUIDs). For their efforts, Josephson, Esaki, and Giaever shared the Nobel Prize for Physics in 1973.

2.1.3 Types of Superconductors

Based on physical properties, superconductors can be divided into two types: Type I [47] if the phase transition is of first order and Type II [48] if the phase transition is of second order (Figure 2.5).

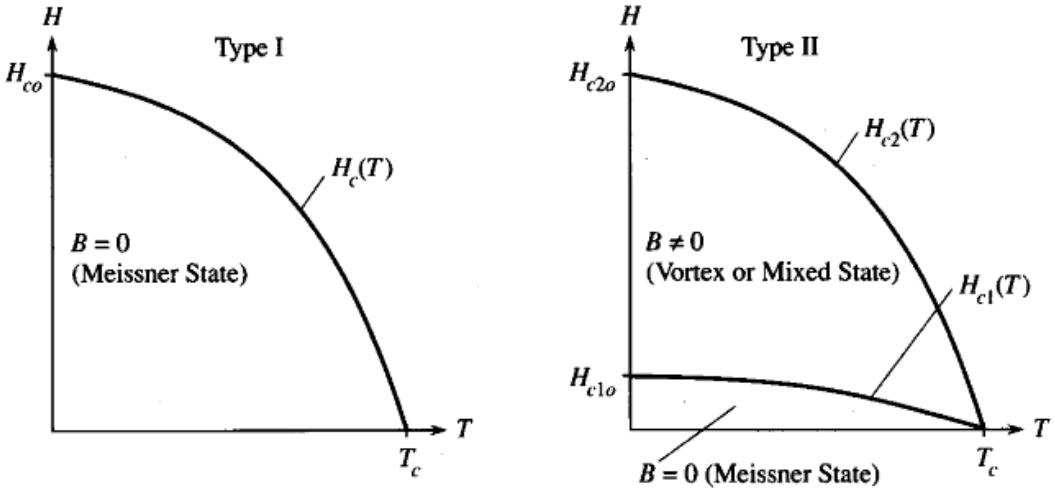

Figure 2.5 Type I and Type II superconductors.

In Type-I superconductors, superconductivity is abruptly destroyed when the strength of the applied field rises above a critical value Hc. As such, they have only a single critical magnetic field at which the material ceases to superconduct, becoming resistive. Depending on the geometry of the sample, one may obtain an intermediate state consisting of a baroque pattern of regions of normal material carrying a magnetic field mixed with regions of superconducting material containing no field. Elementary superconductors, such as aluminum and lead are typical Type-I superconductors. The origin of their superconductivity is explained by BCS theory. Type-I superconductivity is

exhibited by materials with a regularly structured lattice. This allows electrons to be coupled over a relatively large distance (compared to the size of an atom). These pairings are called Cooper pairs.

Though normally electrons exhibit Coulomb repulsion when displayed to each other, when they interact within a lattice, via a phonon interaction they display an attractive force. As this is not a normal state for an electron pair to be in, it is only achieved at very low temperatures. This is because, modeling it as a bond, it has a low bond energy, thus requiring very little force to break it. As such, if the temperature of the material is too high, the energy in the vibrations of the lattice are sufficient to break the bond.

The reason for this force of attraction is an effect known as the 'mattress effect'. This comes about due to spins of electrons. As an electron passes through a lattice, the attractive forces between it and the protons in the nuclei of the atoms cause a ripple in the lattice structure. This means that there are ripples through much of the lattice. These ripples are vibrations called phonons. The ripples induced throughout the lattice will affect other electrons passing through it. This creates the weak link between two electrons being affected by one phonon. This coupling means that even if one electron is presented with resistance the effect of the resistance is minimized as it is 'pulled along' by the other electron.

A Type-II superconductor is a superconductor characterised by its gradual transition from the superconducting to the normal state within an increasing magnetic

field. Typically they superconduct at higher temperatures and magnetic fields than Type-I superconductors. This allows them to conduct higher currents and makes them useful for strong electromagnets. Type-II superconductors are usually made of metal alloys or complex oxide ceramics, whereas most superconducting pure metals are Type-I superconductors. All high temperature superconductors are Type-II superconductors, and (as of early 2008) comprise mostly complex copper oxide ceramics. While most pure metal or pure element superconductors are Type-I, Niobium, Vanadium, Technetium, Diamond and Silicon are pure element Type-II superconductors. Metal alloy superconductors also exhibit Type-II behavior (e.g. niobium-titanium, niobium-tin).

Other Type-II examples are the cuprate-perovskite ceramic materials which have achieved the highest temperatures to reach the superconducting state. These include La1.85Ba0.15CuO4, BSCCO, and YBCO (Yttrium-Barium-Copper-Oxide), which is famous as the first material to achieve superconductivity above the boiling point of liquid nitrogen.

In 2001 Magnesium diboride was discovered to be a type-II SC with useful properties. Until the discovery of the iron-arsenide family, it was the highest temperature superconductor not containing copper.

In comparison to the (theoretically) sharp transition of a Type-I superconductor above the lower temperature Tc1, magnetic flux from external fields is no longer completely expelled, and the superconductor exists in a mixed state. Above the higher temperature Tc2, the superconductivity is completely destroyed, and the material exists in

a normal state. Both of these temperatures are dependent on the strength of the applied field. It is more usual to consider a fixed temperature, in which case transition (flux penetration) occurs between critical field strengths Hc1 and Hc2 (the upper critical field).

Ginzburg–Landau theory defines 2 parameters: The coherence length of a superconductor related to the mean free path of its charge carriers, and a penetration depth.

The earlier London penetration depth is the penetration distance of a weak magnetic field.

In a Type-II superconductor, the coherence length is smaller than the London penetration depth, meaning that magnetic flux lines can pierce the material at high enough external fields. This is known as the vortex state, as the flux lines run through narrow regions of non superconducting material, surrounded by vortices of supercurrents protecting the rest of the superconductor. The vortices can arrange themselves in a regular structure known as the vortex lattice, also named the Abrikosov vortex, after Alexei Alexeyevich Abrikosov, who was awarded the 2003 Nobel Prize in Physics for his pioneering contributions.

Superconductors can also be classified as conventional [49] (if they are explained by the BCS theory or its derivatives) or unconventional [50] (if not). The most commonly used conventional superconductor in applications is a niobium-titanium alloy - this is a type-II superconductor with a Tc of 11 K. The highest critical temperature so far achieved in a conventional superconductor was 39 K (-234 °C) in magnesium diboride.

Unconventional superconductors are materials that display superconductivity which does not conform to either the conventional BCS theory or the Nikolay Bogolyubov's theory or its extensions.

The first unconventional singlet d-wave superconductor, CeCu2Si2, a type of heavy fermion metal, was discovered in 1978 by Frank Steglich.[51] In the early eighties, many more unconventional, heavy fermion superconductors were discovered, including UBe_{13} [52], UPt_3 [53] and URu_2Si_2 [54]. In each of these materials, the anisotropic nature of the pairing is implicated by the power-law dependence of the nuclear magnetic resonance (NMR) relaxation rate and specific heat capacity on temperature. The presence of nodes in the superconducting gap of UPt3 was confirmed in 1986 from the polarization dependence of the ultrasound attenuation [55].

The first unconventional triplet superconductor, organic material $(TMTSF)_2PF_6$, was discovered by Denis Jerome and Klaus Bechgaard in 1979 [56]. Recent experimental works by Paul Chaikin's and Michael Naughton's groups as well as theoretical analysis of their data by Andrei Lebed have firmly confirmed unconventional nature of superconducting pairing in $(TMTSF)_2X$ ($X=PF_6$, ClO_4, etc.) organic materials [57].

High-temperature singlet d-wave superconductivity was discovered by J.G. Bednorz and K.A. Müller in 1986, who discovered that the lanthanum-based cuprate perovskite material LaBaCuO4 develops superconductivity at a critical temperature (Tc) of approximately 35 K (-238 degrees Celsius). This is well above the highest critical temperature known at the time (Tc = 23 K) and thus the new family of materials were

called high-temperature superconductors. Bednorz and Müller received the Nobel Prize in Physics for this discovery in 1987. Since then, many other high-temperature superconductors have been synthesized. As early as 1987, superconductivity above 77 K, the boiling point of nitrogen, was achieved. This is highly significant from the point of view of the technological applications of superconductivity, because liquid nitrogen is far less expensive than liquid helium, which is required to cool conventional superconductors down to their critical temperature. The current record critical temperature is about Tc = 133 K (−140 °C) at standard pressure, and somewhat higher critical temperatures can be achieved at high pressure. Nevertheless at present it is considered unlikely that cuprate perovskite materials will achieve room-temperature superconductivity.

On the other hand, in recent years other unconventional superconductors have been discovered. These include some that do not superconduct at high temperatures, such as the strontium-ruthenate oxide compounds, but that, like the high-temperature superconductors, are unconventional in other ways (for example, the origin of the attractive force leading to the formation of Cooper pairs may be different from the one postulated in BCS theory). In addition to this, superconductors that have unusually high values of Tc but that are not cuprate perovskites have been discovered. Some of them may be extreme examples of conventional superconductors (this is suspected of magnesium diboride, MgB2, with Tc = 39 K). Others display more unconventional features.

In 2008 a new class (layered oxypnictide superconductors), for example LaOFeAs, were discovered that do not include copper [58, 59]. An oxypnictide of samarium seems to have a Tc of about 43 K which is higher than predicted by BCS theory [60]. Tests at up to 45 teslas [61] suggest the upper critical field of $LaFeAsO_{0.89}F_{0.11}$ may be around 64 teslas. Some other iron-based superconductors do not contain oxygen.

By their critical temperature, superconductors can be high temperature [62] (generally considered if they reach the superconducting state just cooling them with liquid nitrogen, that is, if Tc > 77 K), or low temperature (generally if they need other techniques to be cooled under their critical temperature).

From 1960 to 1980, 30 K was thought to be the highest theoretically possible Tc. The first high-Tc superconductor was discovered in 1986 by IBM Researchers Karl Müller and Johannes Bednorz [63], for which they were awarded the Nobel Prize in Physics in 1987. Until Fe-based superconductors were discovered in 2008, the term high-temperature superconductor was used interchangeably with cuprate superconductor for compounds such as bismuth strontium calcium copper oxide (BSCCO) and yttrium barium copper oxide (YBCO).

"High-temperature" has three common definitions in the context of superconductivity:

1. Above the temperature of 30 K that had historically been taken as the upper limit allowed by BCS theory. This is also above the 1973 record of 23 K that had lasted until copper-oxide materials were discovered in 1986.

2. Having a transition temperature that is a larger fraction of the Fermi temperature than for conventional superconductors such as elemental mercury or lead. This definition encompasses a wider variety of unconventional superconductors and is used in the context of theoretical models.

3. Greater than the boiling point of liquid nitrogen (77 K or −196 °C). This is significant for technological applications of superconductivity because liquid nitrogen is a relatively inexpensive and easily handled coolant.

Technological applications benefit from both the higher critical temperature being above the boiling point of liquid nitrogen and also the higher critical magnetic field (and critical current density) at which superconductivity is destroyed. In magnet applications the high critical magnetic field may be more valuable than the high Tc itself. Some cuprates have an upper critical field around 100 teslas. However, cuprate materials are brittle ceramics which are expensive to manufacture and not easily turned into wires or other useful shapes.

Two decades of intense experimental and theoretical research, with over 100,000 published papers on the subject [64], have discovered many common features in the properties of high-temperature superconductors [65], but as of 2009, there is no widely accepted theory to explain their properties. Cuprate superconductors (and other unconventional superconductors) differ in many important ways from conventional superconductors, such as elemental mercury or lead, which are adequately explained by the BCS theory. There also has been much debate as to high-temperature

superconductivity coexisting with magnetic ordering in YBCO [66], iron-based superconductors, several ruthenocuprates and other exotic superconductors, and the search continues for other families of materials. HTS are Type-II superconductors, which allow magnetic fields to penetrate their interior in quantized units of flux, meaning that much higher magnetic fields are required to suppress superconductivity. The layered structure also gives a directional dependence to the magnetic field response.

Magnesium diboride is occasionally referred to as a high-temperature superconductor because its Tc value of 39 K is above that historically expected for BCS superconductors. However, it is more generally regarded as the highest Tc conventional superconductor, the increased Tc resulting from two separate bands being present at the Fermi energy.

Fulleride superconductors [67] where alkali-metal atoms are intercalated into C_{60} molecules show superconductivity at temperatures of up to 38 K for Cs_3C_{60} [68].

Some organic superconductors and heavy fermion compounds are considered to be high-temperature superconductors because of their high Tc values relative to their Fermi energy, despite the Tc values being lower than for many conventional superconductors. This description may relate better to common aspects of the superconducting mechanism than the superconducting properties.

Theoretical work by Neil Ashcroft predicted that liquid metallic hydrogen at extremely high pressure should become superconducting at approximately room-temperature because of its extremely high speed of sound and expected strong

coupling between the conduction electrons and the lattice vibrations [69]. This prediction is yet to be experimentally verified.

Table 2.1 Transition temperatures of well-known superconductors

Transition temperature (k)	Material	Class
133	HgBa2Ca2Cu3Ox	Copper-oxide superconductors
110	Bi2Sr2Ca2Cu3O10(BSCCO)	Copper-oxide superconductors
90	YBa2Cu3O7 (YBCO)	Copper-oxide superconductors
77	Boiling point of liquid nitrogen	
55	SmFeAs(O,F)	Iron-based superconductors
46	CeFeAs(O,F)	Iron-based superconductors
21	LaFeAs(O,F)	Iron-based superconductors
20	Boiling point of liquid hydrogen	
18	Nb3Sn	Metallic low-temperature superconductors
10	NbTi	Metallic low-temperature superconductors
4.2	Hg (mercury)	Metallic low-temperature superconductors

All known high-Tc superconductors are Type-II superconductors. In contrast to Type-I superconductors, which expel all magnetic fields due to the Meissner Effect, Type-II superconductors allow magnetic fields to penetrate their interior in quantized

units of flux, creating "holes" or "tubes" of normal metallic regions in the superconducting bulk. Consequently, high-Tc superconductors can sustain much higher magnetic fields.

2.1. 4 BCS theory

Since discovery of superconductivity, great efforts have been devoted to finding out how and why it works. During the 1950s, theoretical condensed matter physicists arrived at a solid understanding of "conventional" superconductivity, through a pair of remarkable and important theories: the phenomenological Ginzburg-Landau theory (1950) and the microscopic BCS theory (1957) [70, 71]. Generalizations of these theories form the basis for understanding the closely related phenomenon of superfluidity, because they fall into the Lambda transition universality class, but the extent to which similar generalizations can be applied to unconventional superconductors as well is still controversial. The four-dimensional extension of the Ginzburg-Landau theory, the Coleman-Weinberg model, is important in quantum field theory and cosmology.

BCS theory is the first microscopic theory of superconductivity, proposed by Bardeen, Cooper, and Schrieffer in 1957 since the discovery of superconductivity in 1911 [72]. It describes superconductivity as a microscopic effect caused by a "condensation" of pairs of electrons into a boson-like state.

The mid-1950s saw rapid progress in the understanding of superconductivity. It began in the 1948 paper, On the Problem of the Molecular Theory of Superconductivity

where Fritz London proposed that the phenomenological London equations may be consequences of the coherence of a quantum state. In 1953, Brian Pippard, motivated by penetration experiments, proposed that this would modify the London equations via a new scale parameter called the coherence length. John Bardeen then argued in the 1955 paper, Theory of the Meissner Effect in Superconductors that such a modification naturally occurs in a theory with an energy gap. The key ingredient was Leon Neil Cooper's calculation of the bound states of electrons subject to an attractive force in his 1956 paper, Bound Electron Pairs in a Degenerate Fermi Gas.

In 1957 Bardeen and Cooper assembled these ingredients and constructed such a theory, the BCS theory, with Robert Schrieffer. The theory was first announced in February 1957 in the letter, Microscopic theory of superconductivity. The demonstration that the phase transition is second order, that it reproduces the Meissner effect and the calculations of specific heats and penetration depths appeared in the July 1957 article, Theory of superconductivity. They received the Nobel Prize in Physics in 1972 for this theory. The 1950 Landau-Ginzburg theory of superconductivity is not cited in either of the BCS papers.

In 1986, "high-temperature superconductivity" was discovered (i.e. superconductivity at temperatures considerably above the previous limit of about 30 K; up to about 130 K). It is believed that at these temperatures other effects are at play; these effects are not yet fully understood. (It is possible that these unknown effects also control superconductivity even at low temperatures for some materials).

At sufficiently low temperatures, electrons near the Fermi surface become unstable against the formation of Cooper pairs. Cooper showed such binding will occur in the presence of an attractive potential, no matter how weak. In conventional superconductors, an attraction is generally attributed to an electron-lattice interaction. The BCS theory, however, requires only that the potential be attractive, regardless of its origin. In the BCS framework, superconductivity is a macroscopic effect which results from "condensation" of Cooper pairs. These have some bosonic properties, while bosons, at sufficiently low temperature, can form a large Bose-Einstein condensate. Superconductivity was simultaneously explained by Nikolay Bogoliubov, by means of the so-called Bogoliubov transformations.

In many superconductors, the attractive interaction between electrons (necessary for pairing) is brought about indirectly by the interaction between the electrons and the vibrating crystal lattice (the phonons). Roughly speaking the picture is the following:

An electron moving through a conductor will attract nearby positive charges in the lattice. This deformation of the lattice causes another electron, with opposite "spin", to move into the region of higher positive charge density. The two electrons then become correlated. There are a lot of such electron pairs in a superconductor, so that they overlap very strongly, forming a highly collective "condensate". Breaking of one pair results in changing of energies of remained macroscopic number of pairs. If the required energy is higher than the energy provided by kicks from oscillating atoms in the conductor (which is true at low temperatures), then the electrons will stay paired and resist all kicks, thus

not experiencing resistance. Thus, the collective behaviour of "condensate" is a crucial ingredient of superconductivity.

BCS theory starts from the assumption that there is some attraction between electrons, which can overcome the Coulomb repulsion. In most materials (in low temperature superconductors), this attraction is brought about indirectly by the coupling of electrons to the crystal lattice (as explained above). However, the results of BCS theory do not depend on the origin of the attractive interaction. The original results of BCS (discussed below) described an "s-wave" superconducting state, which is the rule among low-temperature superconductors but is not realized in many "unconventional superconductors", such as the "d-wave" high-temperature superconductors. Extensions of BCS theory exist to describe these other cases, although they are insufficient to completely describe the observed features of high-temperature superconductivity.

BCS is able to give an approximation for the quantum-mechanical many-body state of the system of (attractively interacting) electrons inside the metal. This state is now known as the "BCS state". In the normal state of a metal, electrons move independently, whereas in the BCS state, they are bound into "Cooper pairs" by the attractive interaction. The BCS formalism is based on the "reduced" potential for the electrons attraction. Within this potential, a variational ansatz for the wave function is proposed. This ansatz was later shown to be exact in the dense limit of pairs. Note that the continuous crossover between the dilute and dense regimes of attracting pairs of

fermions is still an open problem, which now attracts a lot of attention within the field of ultracold gases.

BCS derived several important theoretical predictions that are independent of the details of the interaction, since the quantitative predictions mentioned below hold for any sufficiently weak attraction between the electrons and this last condition is fulfilled for many low temperature superconductors - the so-called "weak-coupling case". These have been confirmed in numerous experiments:

1. The electrons are bound into Cooper pairs, and these pairs are correlated due to the Pauli Exclusion Principle for the electrons, from which they are constructed. Therefore, in order to break a pair, one has to change energies of all other pairs. This means there is an "energy gap" for "single-particle excitation", unlike in the normal metal (where the state of an electron can be changed by adding an arbitrarily small amount of energy). This energy gap is highest at low temperatures but vanishes at the transition temperature when superconductivity ceases to exist. The BCS theory gives an expression that shows how the gap grows with the strength of the attractive interaction and the (normal phase) single particle density of states at the Fermi energy. Furthermore, it describes how the density of states is changed on entering the superconducting state, where there are no electronic states any more at the Fermi energy. The energy gap is most directly observed in tunneling experiments and in reflection of microwaves from the superconductor.

2. BCS theory predicts the dependence of the value of the energy gap E at temperature T on the critical temperature Tc. The ratio between the value of the energy gap at zero temperature and the value of the superconducting transition temperature (expressed in energy units) takes the universal value of 3.5, independent of material. Near the critical temperature the relation asymptotes to:

$$E = 3.25 k_B T_c \sqrt{1 - (T / T_c)} \tag{2.2}$$

which is of the form suggested the previous year by M. J. Buckingham in Very High Frequency Absorption in Superconductors based on the fact that the superconducting phase transition is second order, that the superconducting phase has a mass gap and on Blevins, Gordy and Fairbank's experimental results the previous year on the absorption of millimeter waves by superconducting tin.

3. Due to the energy gap, the specific heat of the superconductor is suppressed strongly (exponentially) at low temperatures, there being no thermal excitations left. However, before reaching the transition temperature, the specific heat of the superconductor becomes even higher than that of the normal conductor (measured immediately above the transition) and the ratio of these two values is found to be universally given by 2.5.

4. BCS theory correctly predicts the Meissner effect, i.e. the expulsion of a magnetic field from the superconductor and the variation of the penetration depth (the extent of the screening currents flowing below the metal's surface) with temperature. This

had been demonstrated experimentally by Walther Meissner and Robert Ochsenfeld in their 1933 article Ein neuer Effekt bei Eintritt der Supraleitfähigkeit.

5. It also describes the variation of the critical magnetic field (above which the superconductor can no longer expel the field but becomes normal conducting) with temperature. BCS theory relates the value of the critical field at zero temperature to the value of the transition temperature and the density of states at the Fermi energy.

6. In its simplest form, BCS gives the superconducting transition temperature in terms of the electron-phonon coupling potential and the Debye cutoff energy:

$$k_B T_c = 1.14 E_D e^{-1/N(o)V} \tag{2.3}$$

7. The BCS theory reproduces the isotope effect, which is the experimental observation that for a given superconducting material, the critical temperature is inversely proportional to the mass of the isotope used in the material. The isotope effect was reported by two groups on the 24th of March 1950, who discovered it independently working with different mercury isotopes, although a few days before publication they learned of each other's results at the ONR conference in Atlanta, Georgia. The two groups are Emanuel Maxwell, who published his results in Isotope Effect in the Superconductivity of Mercury and C. A. Reynolds, B. Serin, W. H. Wright, and L. B. Nesbitt who published their results 10 pages later in Superconductivity of Isotopes of Mercury. The choice of isotope ordinarily has little effect on the electrical properties of a material, but does affect the frequency of lattice vibrations, this effect suggested that

superconductivity be related to vibrations of the lattice. This is incorporated into the BCS theory, where lattice vibrations yield the binding energy of electrons in a Cooper pair.

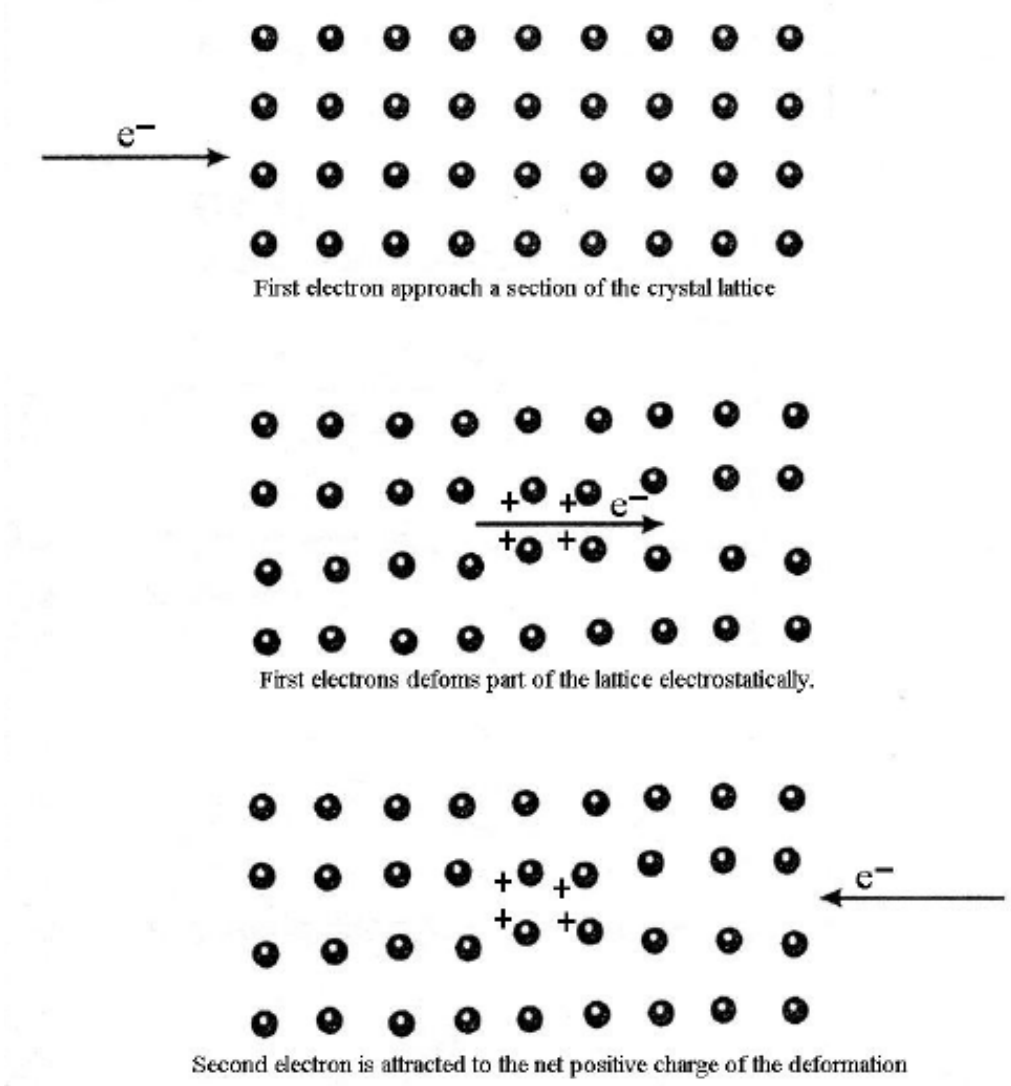

Figure 2.6 Classical description of the coupling of a Cooper pair.

2.1. 5 Cuprate and Iron Pnictides

Cuprate superconductors are generally considered to be quasi-two-dimensional materials with their superconducting properties determined by electrons moving within weakly

coupled copper-oxide (CuO_2) layers. Neighboring layers containing ions such as La, Ba, Sr, or other atoms act to stabilize the structure and dope electrons or holes onto the copper-oxide layers. The undoped 'parent' or 'mother' compounds are Mott insulators with long-range antiferromagnetic order at low enough temperature. Single band models are generally considered to be sufficient to describe the electronic properties.

The cuprate superconductors adopt a perovskite structure. The copper-oxide planes are checkerboard lattices with squares of O^{2-} ions with a Cu^{2+} ion at the centre of each square. The unit cell is rotated by 45° from these squares. Chemical formulae of superconducting materials generally contain fractional numbers to describe the doping required for superconductivity. There are several families of cuprate superconductors and they can be categorized by the elements they contain and the number of adjacent copper-oxide layers in each superconducting block. For example, YBCO and BSCCO can alternatively be referred to as Y123 and Bi2201/Bi2212/Bi2223 depending on the number of layers in each superconducting block (n). The superconducting transition temperature has been found to peak at an optimal doping value (p=0.16) and an optimal number of layers in each superconducting block, typically n = 3.

Possible mechanisms for superconductivity in the cuprates are still the subject of considerable debate and further research. Certain aspects common to all materials have been identified [65]. Similarities between the antiferromagnetic low-temperature state of the undoped materials and the superconducting state that emerges upon doping, primarily

the $d_{x^2-y^2}$ orbital state of the Cu^{2+} ions, suggest that electron-electron interactions are more significant than electron-phonon interactions in cuprates – making the superconductivity unconventional. Recent work on the Fermi surface has shown that nesting occurs at four points in the antiferromagnetic Brillouin zone where spin waves exist and that the superconducting energy gap is larger at these points. The weak isotope effects observed for most cuprates contrast with conventional superconductors that are well described by BCS theory.

Similarities and differences in the properties of hole-doped and electron doped cuprates:

* Presence of a pseudogap phase up to at least optimal doping.

* Different trends in the Uemura plot relating transition temperature to the superfluid density. The inverse square of the London penetration depth appears to be proportional to the critical temperature for a large number of underdoped cuprate superconductors, but the constant of proportionality is different for hole- and electron-doped cuprates. The linear trend implies that the physics of these materials is strongly two-dimensional.

* Universal hourglass-shaped feature in the spin excitations of cuprates measured using inelastic neutron diffraction.

* Nernst effect evident in both the superconducting and pseudogap phases.

Iron-based superconductors contain layers of iron and a pnictogen, such as arsenic, phosphorus, or chalcogens. This is currently the family with the second highest critical

temperature, behind the cuprates. Interest in their superconducting properties began in 2006 with the discovery of superconductivity in LaFePO at 4 K [73] and gained much greater attention in 2008 after the analogous material LaFeAs(O,F) [74] was found to superconduct at up to 43 K under pressure [58].

Since the original discoveries several families of iron-based superconductors have emerged (Figure 2.7):

* LnFeAs(O,F) or $LnFeAsO_{1-x}$ with Tc up to 56 K, referred to as 1111 materials [75] A fluoride variant of these materials was subsequently found with similar Tc values [76].

* (Ba,K)Fe2As2 and related materials with pairs of iron-arsenide layers, referred to as 122 compounds. Tc values range up to 38 K [77, 78] These materials also superconduct when iron is replaced with cobalt

* LiFeAs and NaFeAs with Tc up to around 20 K. These materials superconduct close to stoichiometric composition and are referred to as 111 compounds [79-81]

* FeSe with small off-stoichiometry or tellurium doping [82].

Most undoped iron-based superconductors show a tetragonal-orthorhombic structural phase transition followed at lower temperature by magnetic ordering, similar to the cuprate superconductors [83]. However, they are poor metals rather than Mott insulators and have five bands at the Fermi surface rather than one. The phase diagram emerging as the iron-arsenide layers are doped is remarkably similar, with the superconducting phase close to or overlapping the magnetic phase. Strong evidence that

the Tc value varies with the As-Fe-As bond angles has already emerged and shows that the optimal Tc value is obtained with undistorted $FeAs_4$ tetrahedra [84]. The symmetry of the pairing wave function is still widely debated, but an extended s-wave scenario is currently favored.

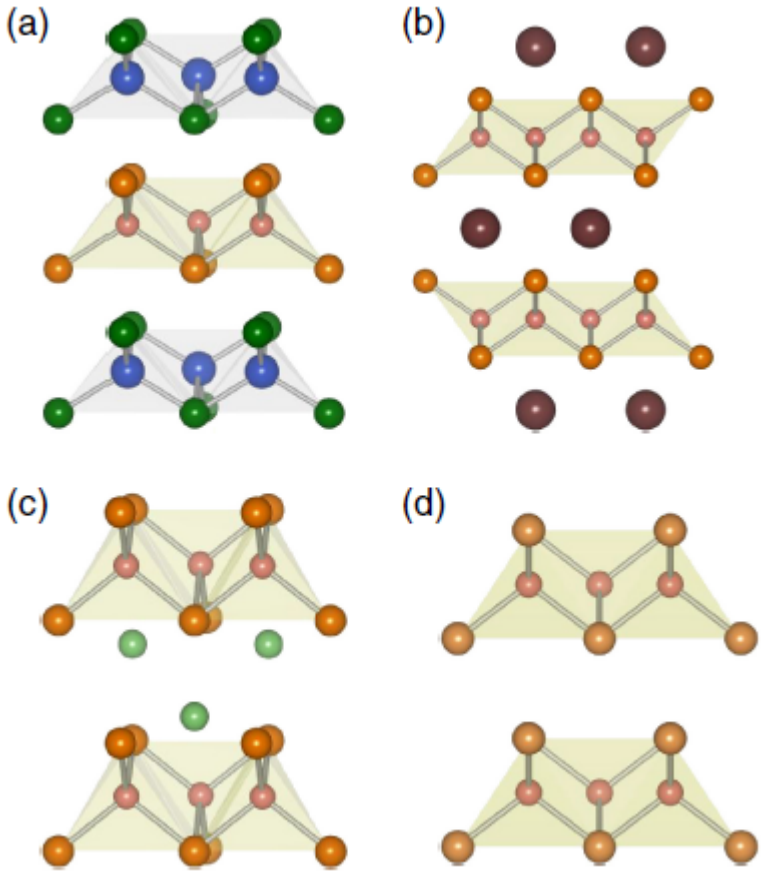

Figure 2.7 Crystal structures of (a) LaFeAsO (refered to as‘‘1111’’ in the article), (b) $BaFe_2As_2$ (‘‘122’’), (c) LiFeAs (‘‘111’’), and (d) FeSe (‘‘11’’).

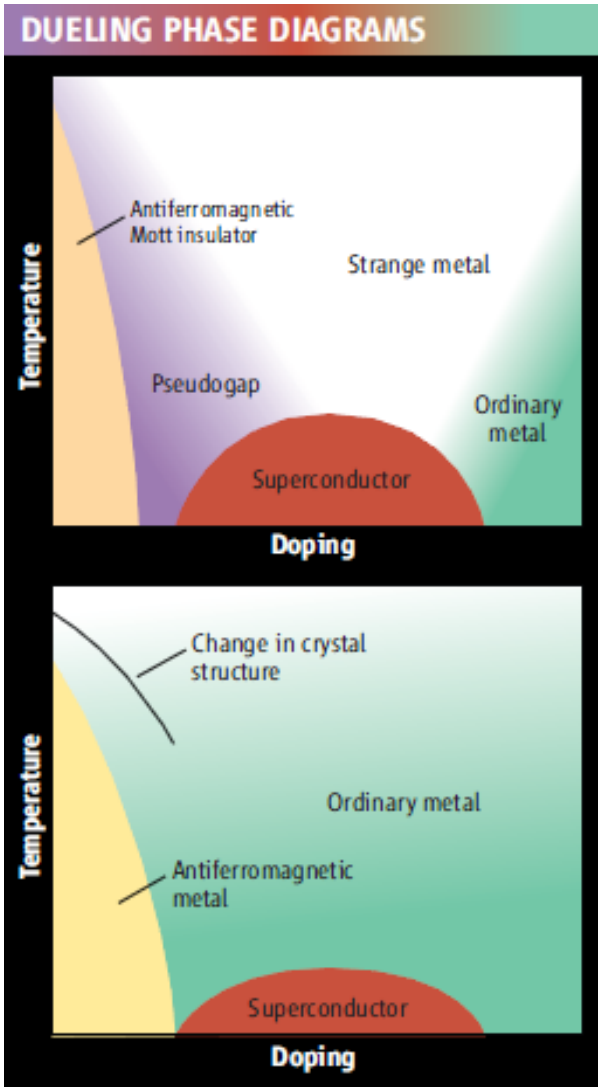

Figure 2.8 Cuprate superconductors (top) and newer ion-based ones (bottom) display some striking similarities as temperature and composition vary.

Cuprates and iron-based superconductors share some striking similarities (Figure 2.8). First of all, they are both quasi-2D (layered) materials with square lattice. They both contain planes of ions magnetized in opposite directions. In the cuprates, electrons hop from copper to copper (arrow). For iron-based superconductors, early results show the As-Fe-As layer is responsible for the superconductivity. Secondly, they have similar phase diagram. Their parent compounds are both AFM ground state and

superconductivity appears only at certain doping level. Above the superconductivity temperature Tc they are both high resistivity strange metals, and beyond the upper doping limit they are both Fermi liquids.

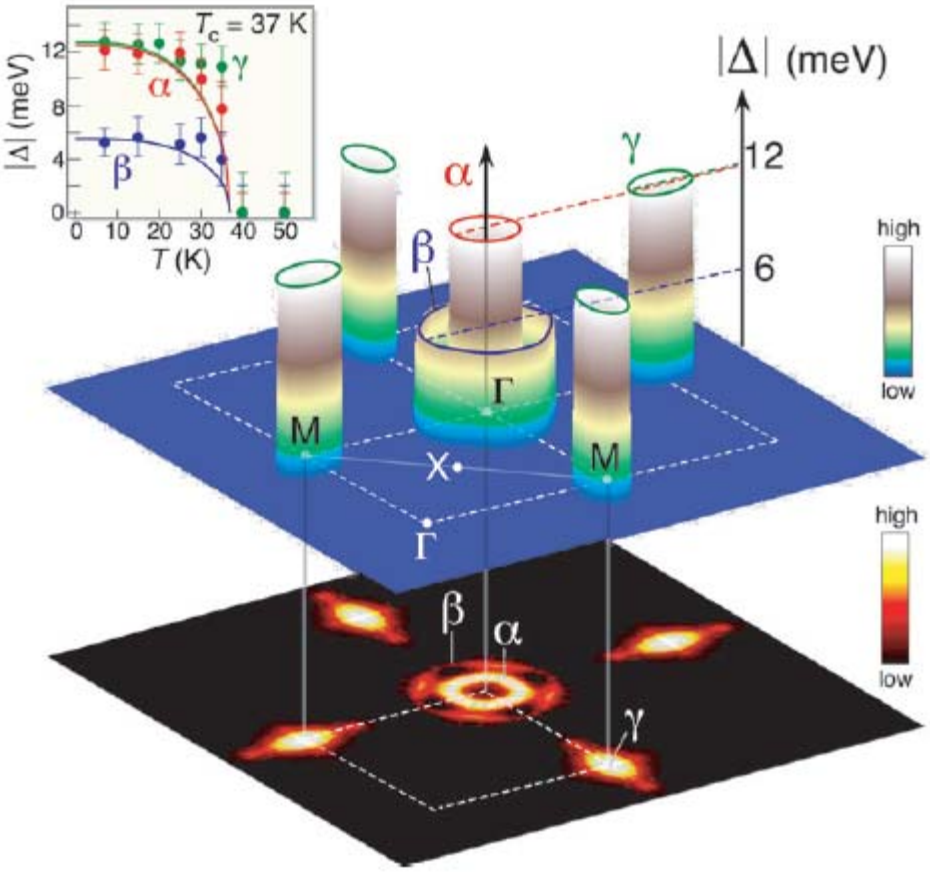

Figure 2.9 Three-dimensional plot of the superconducting-gap size (Δ) measured at 15K on the three observed FS sheets (shown at the bottom as an intensity plot) and their temperature evolutions (inset).

However they are not exactly the same, many differences yet remains. The undoped cuprate is mott insulator, while the parent compound of iron-based superconductor is metal. The cuprates have only one band on Fermi surface whereas iron-based superconductors have five bands (Figure 2.9). The cuprates have d-wave order

parameter, while the order parameter of iron-based superconductor is most possibly spin density wave.

2.1. 6 Raman Spectroscopy

Although the inelastic scattering of light was predicted by Adolf Smekal in 1923, it is not until 1928 that it was observed in practice. The Raman effect was named after one of its discoverers, the Indian scientist Sir C. V. Raman who observed the effect by means of sunlight (1928, together with K. S. Krishnan and independently by Grigory Landsberg and Leonid Mandelstam) [85, 86]. Raman won the Nobel Prize in Physics in 1930 for this discovery accomplished using sunlight, a narrow band photographic filter to create monochromatic light and a "crossed" filter to block this monochromatic light. He found that light of changed frequency passed through the "crossed" filter.

Systematic pioneering theory of the Raman effect was developed by Czechoslovak physicist George Placzek between 1930 and 1934 [87]. The mercury arc became the principal light source, first with photographic detection and then with spectrophotometric detection. At the present time, lasers are used as light sources.

Raman spectroscopy is a spectroscopic technique used to study vibrational, rotational, and other low-frequency modes in a system. It relies on inelastic scattering, or Raman scattering, of monochromatic light, usually from a laser in the visible, near infrared, or near ultraviolet range. The laser light interacts with molecular vibrations, phonons or other excitations in the system, resulting in the energy of the laser photons

being shifted up or down. The shift in energy gives information about the phonon modes in the system. Infrared spectroscopy yields similar, but complementary, information.

Typically, a sample is illuminated with a laser beam. Light from the illuminated spot is collected with a lens and sent through a monochromator. Wavelengths close to the laser line, due to elastic Rayleigh scattering, are filtered out while the rest of the collected light is dispersed onto a detector.

Spontaneous Raman scattering is typically very weak, and as a result the main difficulty of Raman spectroscopy is separating the weak inelastically scattered light from the intense Rayleigh scattered laser light. Historically, Raman spectrometers used holographic gratings and multiple dispersion stages to achieve a high degree of laser rejection. In the past, photomultipliers were the detectors of choice for dispersive Raman setups, which resulted in long acquisition times. However, modern instrumentation almost universally employs notch or edge filters for laser rejection and spectrographs (either axial transmissive (AT), Czerny-Turner (CT) monochromator) or FT (Fourier transform spectroscopy based), and CCD detectors.

The Raman Effect occurs when light impinges upon a molecule and interacts with the electron cloud and the bonds of that molecule. For the spontaneous Raman Effect, a photon excites the molecule from the ground state to a virtual energy state. When the molecule relaxes it emits a photon and it returns to a different rotational or vibrational state. The difference in energy between the original state and this new state leads to a shift in the emitted photon's frequency away from the excitation wavelength.

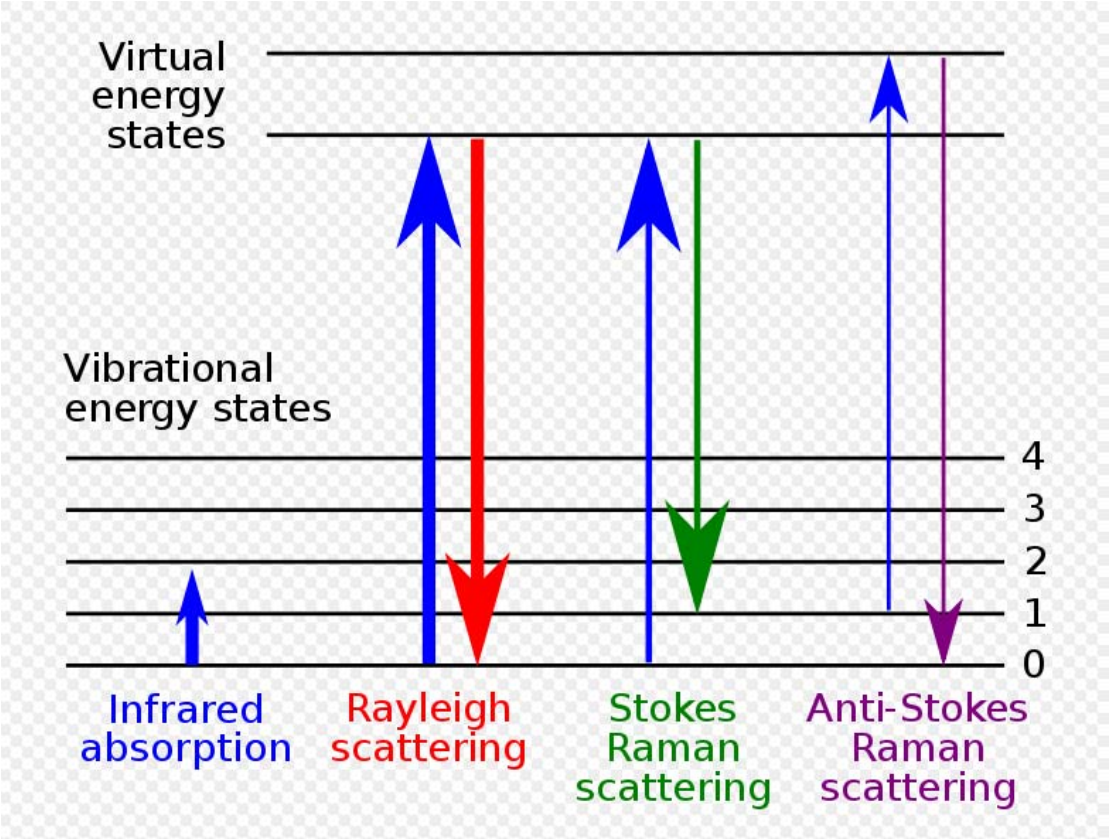

Figure 2.10 Energy level diagram showing the states involved in Raman signal. The line thickness is roughly proportional to the signal strength from the different transitions.

If the final vibrational state of the molecule is more energetic than the initial state, then the emitted photon will be shifted to a lower frequency in order for the total energy of the system to remain balanced. This shift in frequency is designated as a Stokes shift (Figure 2.10). If the final vibrational state is less energetic than the initial state, then the emitted photon will be shifted to a higher frequency, and this is designated as an Anti-Stokes shift. Raman scattering is an example of inelastic scattering because of the energy transfer between the photons and the molecules during their interaction.

A change in the molecular polarization potential — or amount of deformation of the electron cloud — with respect to the vibrational coordinate is required for a molecule to exhibit a Raman Effect. The amount of the polarizability change will determine the Raman scattering intensity. The pattern of shifted frequencies is determined by the rotational and vibrational states of the sample.

Raman spectra are typically expressed in wavenumbers, which have units of inverse length. In order to convert between spectral wavelength and wavenumbers of shift in the Raman spectrum, the following formula can be used:

$$\Delta\omega\left(cm^{-1}\right)=\left(\frac{1}{\lambda_0(nm)}-\frac{1}{\lambda_1(nm)}\right)\times 10^7 \qquad (2.4)$$

where Δw is the Raman shift expressed in wavenumber, λ_0 is the excitation wavelength, and λ_1 is the Raman spectrum wavelength. Here the units chosen for expressing wavenumber in Raman spectra is inverse centimeters (cm^{-1}), and wavelength is expressed in units of nanometers (nm).

Raman spectroscopy is commonly used in chemistry, since vibrational information is specific to the chemical bonds and symmetry of molecules. Therefore, it provides a fingerprint by which the molecule can be identified. For instance, the vibrational frequencies of SiO, Si_2O_2, and Si_3O_3 were identified and assigned on the basis of normal coordinate analyses using infrared and Raman spectra [88]. The fingerprint region of organic molecules is in the (wavenumber) range 500–2000 cm^{-1}. Another way

that the technique is used is to study changes in chemical bonding, e.g., when a substrate is added to an enzyme.

Raman gas analyzers have many practical applications. For instance, they are used in medicine for real-time monitoring of anaesthetic and respiratory gas mixtures during surgery.

In solid state physics, spontaneous Raman spectroscopy is used to, among other things, characterize materials, measure temperature, and find the crystallographic orientation of a sample. As with single molecules, a given solid material has characteristic phonon modes that can help an experimenter identify it. In addition, Raman spectroscopy can be used to observe other low frequency excitations of the solid, such as plasmons, magnons, and superconducting gap excitations. The spontaneous Raman signal gives information on the population of a given phonon mode in the ratio between the Stokes (downshifted) intensity and anti-Stokes (upshifted) intensity.

Raman scattering by an anisotropic crystal gives information on the crystal orientation. The polarization of the Raman scattered light with respect to the crystal and the polarization of the laser light can be used to find the orientation of the crystal, if the crystal structure (to be specific, its point group) is known.

Raman active fibers, such as aramid and carbon, have vibrational modes that show a shift in Raman frequency with applied stress. Polypropylene fibers also exhibit similar shifts. The radial breathing mode is a commonly used technique to evaluate the

diameter of carbon nanotubes. In nanotechnology, a Raman microscope can be used to analyze nanowires to better understand the composition of the structures.

Spatially-offset Raman spectroscopy (SORS), which is less sensitive to surface layers than conventional Raman, can be used to discover counterfeit drugs without opening their internal packaging, and for non-invasive monitoring of biological tissue [89]. Raman spectroscopy can be used to investigate the chemical composition of historical documents such as the Book of Kells and contribute to knowledge of the social and economic conditions at the time the documents were produced [90]. This is especially helpful because Raman spectroscopy offers a non-invasive way to determine the best course of preservation or conservation treatment for such materials.

Raman spectroscopy is being investigated as a means to detect explosives for airport security. Raman spectroscopy has also been used to confirm the prediction of existence of low-frequency phonons in proteins and DNA.

Raman spectroscopy offers several advantages for microscopic analysis. Since it is a scattering technique, specimens do not need to be fixed or sectioned. Raman spectra can be collected from a very small volume (< 1 μm in diameter); these spectra allow the identification of species present in that volume. Water does not generally interfere with Raman spectral analysis. Thus, Raman spectroscopy is suitable for the microscopic examination of minerals, materials such as polymers and ceramics, cells and proteins. A Raman microscope begins with a standard optical microscope, and adds an excitation laser, a monochromator, and a sensitive detector (such as a charge-coupled device (CCD),

or photomultiplier tube (PMT)). FT-Raman has also been used with microscopes.

In direct imaging, the whole field of view is examined for scattering over a small range of wavenumbers (Raman shifts). For instance, a wavenumber characteristic for cholesterol could be used to record the distribution of cholesterol within a cell culture.

The other approach is hyperspectral imaging or chemical imaging, in which thousands of Raman spectra are acquired from all over the field of view. The data can then be used to generate images showing the location and amount of different components. Taking the cell culture example, a hyperspectral image could show the distribution of cholesterol, as well as proteins, nucleic acids, and fatty acids. Sophisticated signal- and image-processing techniques can be used to ignore the presence of water, culture media, buffers, and other interferents.

Raman microscopy, and in particular confocal microscopy, has very high spatial resolution. For example, the lateral and depth resolutions were 250 nm and 1.7 μm, respectively, using a confocal Raman microspectrometer with the 632.8 nm line from a Helium-Neon laser with a pinhole of 100 μm diameter. Since the objective lenses of microscopes focus the laser beam to several micrometres in diameter, the resulting photon flux is much higher than achieved in conventional Raman setups. This has the added benefit of enhanced fluorescence quenching. However, the high photon flux can also cause sample degradation, and for this reason some setups require a thermally conducting substrate (which acts as a heat sink) in order to mitigate this process.

By using Raman microspectroscopy, in vivo time- and space-resolved Raman spectra of microscopic regions of samples can be measured. As a result, the fluorescence of water, media, and buffers can be removed. Consequently in vivo time- and space-resolved Raman spectroscopy is suitable to examine proteins, cells and organs.

Raman microscopy for biological and medical specimens generally uses near-infrared (NIR) lasers (785 nm diodes and 1064 nm Nd:YAG are especially common). This reduces the risk of damaging the specimen by applying higher energy wavelengths. However, the intensity of NIR Raman is low (owing to the $\omega 4$ dependence of Raman scattering intensity), and most detectors required very long collection times. Recently, more sensitive detectors have become available, making the technique better suited to general use. Raman microscopy of inorganic specimens, such as rocks and ceramics and polymers, can use a broader range of excitation wavelengths [91].

The polarization of the Raman scattered light also contains useful information. This property can be measured using (plane) polarized laser excitation and a polarization analyzer. Spectra acquired with the analyzer set at both perpendicular and parallel to the excitation plane can be used to calculate the depolarization ratio. Study of the technique is useful in teaching the connections between group theory, symmetry, Raman activity, and peaks in the corresponding Raman spectra.

The spectral information arising from this analysis gives insight into molecular orientation and vibrational symmetry. In essence, it allows the user to obtain valuable information relating to the molecular shape, for example in synthetic chemistry or

polymorph analysis. It is often used to understand macromolecular orientation in crystal lattices, liquid crystals or polymer samples.

Several variations of Raman spectroscopy have been developed. The usual purpose is to enhance the sensitivity (e.g., surface-enhanced Raman), to improve the spatial resolution (Raman microscopy), or to acquire very specific information (resonance Raman).

* Surface Enhanced Raman Spectroscopy (SERS) - Normally done in a silver or gold colloid or a substrate containing silver or gold. Surface plasmons of silver and gold are excited by the laser, resulting in an increase in the electric fields surrounding the metal. Given that Raman intensities are proportional to the electric field, there is large increase in the measured signal (by up to 10^{11}). This effect was originally observed by Martin Fleischmann but the prevailing explanation was proposed by Van Duyne in 1977 [92].

* Resonance Raman spectroscopy - The excitation wavelength is matched to an electronic transition of the molecule or crystal, so that the vibrational modes associated with the excited electronic state are greatly enhanced. This is useful for studying large molecules such as polypeptides, which might show hundreds of bands in "conventional" Raman spectra. It is also useful for associating normal modes with their observed frequency shifts [93].

* Surface-Enhanced Resonance Raman Spectroscopy (SERRS) - A combination of SERS and resonance Raman spectroscopy that uses proximity to a surface to increase

Raman intensity, and excitation wavelength matched to the maximum absorbance of the molecule being analyzed.

* Hyper Raman - A non-linear effect in which the vibrational modes interact with the second harmonic of the excitation beam. This requires very high power, but allows the observation of vibrational modes that are normally "silent". It frequently relies on SERS-type enhancement to boost the sensitivity [94].

* Spontaneous Raman Spectroscopy - Used to study the temperature dependence of the Raman spectra of molecules.

* Optical Tweezers Raman Spectroscopy (OTRS) - Used to study individual particles, and even biochemical processes in single cells trapped by optical tweezers.

* Stimulated Raman Spectroscopy - A spatially coincedent, two color pulse (with polarization either parallel or perpendicular) transfers the population from ground to a rovibrationally excited state, if the difference in energy corresponds to an allowed Raman transition, and if neither frequency corresponds to an electronic resonance. Two photon UV ionization, applied after the population transfer but before relaxation, allows the intra-molecular or inter-molecular Raman spectrum of a gas or molecular cluster (indeed, a given conformation of molecular cluster) to be collected. This is a useful molecular dynamics technique.

* Spatially Offset Raman Spectroscopy (SORS) - The Raman scatter is collected from regions laterally offset away from the excitation laser spot, leading to significantly lower contributions from the surface layer than with traditional Raman spectroscopy [95].

* Coherent anti-Stokes Raman spectroscopy (CARS) - Two laser beams are used to generate a coherent anti-Stokes frequency beam, which can be enhanced by resonance.

* Raman optical activity (ROA) - Measures vibrational optical activity by means of a small difference in the intensity of Raman scattering from chiral molecules in right- and left-circularly polarized incident light or, equivalently, a small circularly polarized component in the scattered light [96].

* Transmission Raman - Allows probing of a significant bulk of a turbid material, such as powders, capsules, living tissue, etc. It was largely ignored following investigations in the late 1960s but was rediscovered in 2006 as a means of rapid assay of pharmaceutical dosage forms [97] There are also medical diagnostic applications [98].

* Inverse Raman spectroscopy. Suppose a material is irradiated simultaneously by intense monochromatic light of frequency ν_L (typically a laser beam) and light with a continuum of higher frequencies. Among the possibilities for light scattering are scattering: (1) from the monochromatic beam at ν_L to the continuum at $\nu_L + \nu_M$ (anti-Stokes Raman scattering), (2) from the continuum at $\nu_L + \nu_M$ to the monochromatic beam at ν_L (Stokes Raman scattering), where ν_M is a Raman frequency of the material. The strength of these two scatterings depends (among other things) on the energy levels of the material, their occupancy, and the intensity of the continuum. In some circumstances, Stokes scattering can exceed anti-Stokes scattering, in which case, the continuum, upon leaving the material, is observed to have an absorption line (a dip in intensity) at $\nu_L + \nu_M$. This phenomenon is referred to as the

inverse Raman effect, application of the phenomenon is referred to as inverse Raman spectroscopy.

*Tip-Enhanced Raman Spectroscopy (TERS) - Uses a metallic (usually silver-/gold-coated AFM or STM) tip to enhance the Raman signals of molecules situated in its vicinity. The spatial resolution is approximately the size of the tip apex (20-30 nm). TERS has been shown to have sensitivity down to the single molecule level.

The Raman effect differs from the process of fluorescence [99]. For the latter, the incident light is completely absorbed and the system is transferred to an excited state from which it can go to various lower states only after a certain resonance lifetime. The result of both processes is essentially the same: A photon with the frequency different from that of the incident photon is produced and the molecule is brought to a higher or lower energy level. But the major difference is that the Raman effect can take place for any frequency of the incident light. In contrast to the fluorescence effect, the Raman effect is therefore not a resonant effect. In practice, this means that a fluorescence peak is anchored at a specific excitation frequency, whereas a Raman peak maintains a constant separation from the excitation frequency. Another, related distinction is that Raman scattering is a coherent process, whereas fluorescence is not [100]. This means that the measured intensity is the square of a coherent sum of scattering amplitudes. In practice, this means that different paths to the excitation of the same mode may interfere, leading to Fano effects: asymmetries in the shape of the scattering peaks.

There are many sources of Raman excitations, like phonon excitation, magnon excitation, crystal excitation, electronic Raman and many more (Figure 2.11).

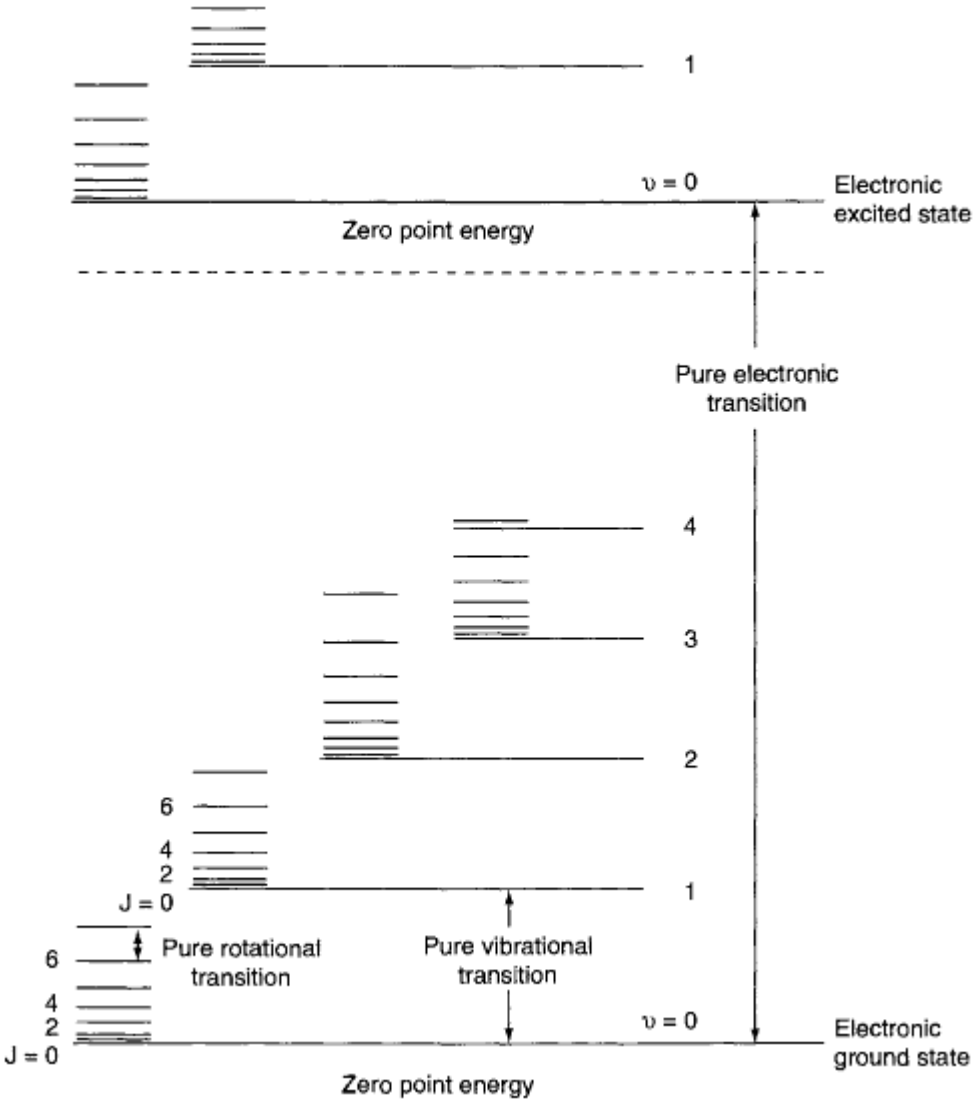

Figure 2.11 Three types of transitions for a diatomic molecule.

Raman excitations should follow selection rule [101-106]. According to classical theory, Raman scattering can be explained as follows: The electric field strength (E) of the electromagnetic wave (laser beam) fluctuates with time (t):

$$E = E_0 \cos 2\pi \nu_0 t \tag{2.5}$$

where E_0 is the vibrational amplitude and ν_0 is the frequency of the laser. If a diatomic molecule is irradiated by this fight, an electric dipole moment P is induced:

$$P = \alpha E = \alpha E_0 \cos 2\pi \nu_0 t \tag{2.6}$$

Here, α is a proportionality constant and is called polarizability. If the molecule is vibrating with a frequency ν_m, the nuclear displacement q is written as:

$$q = q_0 \cos 2\pi \nu_m t \tag{2.7}$$

Where q_0 is the vibrational amplitude. For a small amplitude of vibration, α is a linear function of q. Thus, we can write:

$$\alpha = \alpha_0 + \left(\frac{\partial \alpha}{\partial q}\right)_0 q_0 + \ldots \tag{2.8}$$

Here, α_0 is the polarizability at the equilibrium position, and $\left(\frac{\partial \alpha}{\partial q}\right)_0$ is the rate of change of α with respect to the change in q, evaluated at the equilibrium position.

Combing (2.6), (2.7), (2.8), we obtain:

$$\begin{aligned} P &= \alpha_0 E_0 \cos 2\pi \nu_0 t + \left(\frac{\partial \alpha}{\partial q}\right)_0 q_0 E_0 \cos 2\pi \nu_0 t \cos 2\pi \nu_m t \\ &= \alpha_0 E_0 \cos 2\pi \nu_0 t + \frac{1}{2}\left(\frac{\partial \alpha}{\partial q}\right)_0 q_0 E_0 \{\cos[2\pi(\nu_0 + \nu_m)t] + \cos[2\pi(\nu_0 - \nu_m)t]\} \end{aligned} \tag{2.9}$$

According to classical theory, the first term represents an oscillating dipole that radiates light of frequency ν_0 (Rayleigh scattering), while the second term corresponds to the Raman scattering of frequency $\nu_0 + \nu_m$ (anti-Stokes) and $\nu_0 - \nu_m$ (Stokes). If $\left(\frac{\partial \alpha}{\partial q}\right)_0$ is zero, the vibration is not Raman-active. Namely, to be Raman-active, the rate of change of polarizability (α) with the vibration must not be zero. Since the origins of IR and Raman spectra are markedly different, their selection rules are also distinctively different. According to quantum mechanics a vibration is IR-active if the dipole moment is changed during the vibration and is Raman-active if the polarizability is changed during the vibration. When a molecule is placed in an electric field (laser beam), it suffers distortion since the positively charged nuclei are attracted toward the negative pole, and electrons toward the positive pole (Fig.). This charge separation produces an induced dipole moment (P) given by:

$$P = \alpha E \tag{2.10}$$

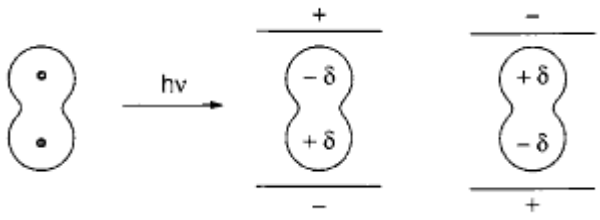

Figure 2.12 Polarization of a diatomic molecule in an electric field.

In actual molecules, such a simple relationship does not hold since both P and E are vectors consisting of three components in the x, y and z directions. Thus, Eq. (2.10) must be written as:

$$\begin{aligned} P_x &= \alpha_{xx}E_x + \alpha_{xy}E_y + \alpha_{xz}E_z \\ P_y &= \alpha_{yx}E_x + \alpha_{yy}E_y + \alpha_{yz}E_z \\ P_z &= \alpha_{zx}E_x + \alpha_{zy}E_y + \alpha_{zz}E_z \end{aligned} \tag{2.11}$$

In matrix form, this is written as:

$$\begin{bmatrix} P_x \\ P_y \\ P_z \end{bmatrix} = \begin{bmatrix} \alpha_{xx} & \alpha_{xy} & \alpha_{xz} \\ \alpha_{yx} & \alpha_{yy} & \alpha_{yz} \\ \alpha_{zx} & \alpha_{zy} & \alpha_{zz} \end{bmatrix} \begin{bmatrix} E_x \\ E_y \\ E_z \end{bmatrix} \tag{2.12}$$

The first matrix on the right-hand side is called the polarizability tensor. In normal Raman scattering, this tensor is symmetric: $\alpha_{xy} = \alpha_{yz}$, $\alpha_{xz} = \alpha_{zx}$ and $\alpha_{yz} = \alpha_{zy}$. According to quantum mechanics, the vibration is Raman-active if one of these components of the polarizability tensor is changed during the vibration. In the case of small molecules, it is easy to see whether or not the polarizability changes during the vibration. Consider linear molecules such as CO_2. Their electron clouds have an elongated water melon like shape with circular cross-sections. In these molecules, the electrons are more polarizable (a larger α) along the chemical bond than in the direction perpendicular to it. If we plot α_i (α in the i-direction) from the center of gravity in all directions, we end up with a three-dimensional surface. Conventionally, we plot $1/\sqrt{\alpha_i}$ rather than α_i itself and call the resulting three-dimensional body a polarizability ellipsoid.

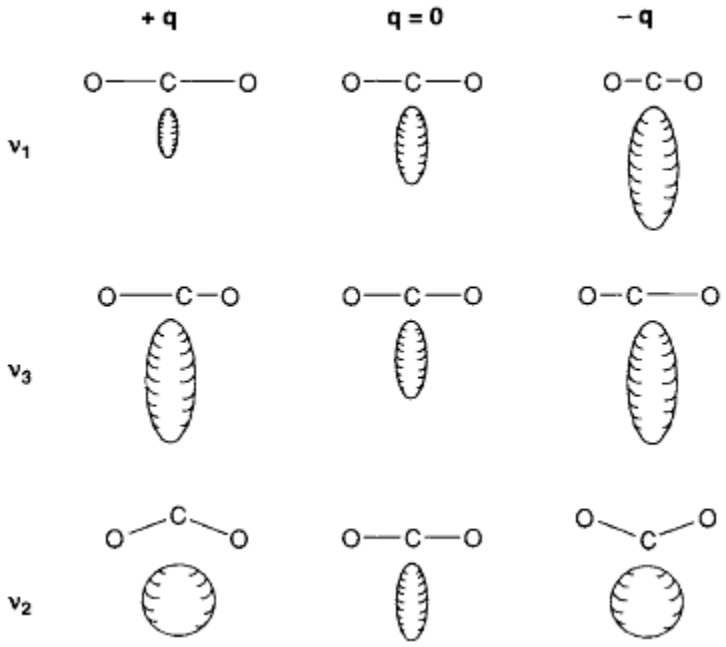

Figure 2.13 Changes in polarizability ellipsoids during vibration of CO_2 molecule.

In terms of the polarizability ellipsoid, the vibration is Raman-active if the size, shape or orientation changes during the normal vibration. In the ν_1 vibration, the size of the ellipsoid is changing; the diagonal elements (α_{xx}, α_{yy} and α_{zz}) are changing simultaneously. Thus, it is Raman-active. Although the size of the ellipsoid is changing during the ν_3 vibration, the ellipsoids at two extreme displacements ($+q$ and $-q$) are exactly the same in this case. Thus, this vibration is not Raman-active if we consider a small displacement. The difference between the ν_1 and ν_3 is shown in Fig. Note that the Raman activity is determined by $\left(\frac{d\alpha}{dq}\right)_0$ (slope near the equihbrium position). During the ν_2 vibration, the shape of the ellipsoid is sphere-hke at two extreme configurations. However, the size and shape of the elhpsoid are exactly the same at $+q$

and $-q$. Thus, it is not Raman-active for the same reason as that of ν_3. As these examples show, it is not necessary to figure out the exact size, shape or orientation of the ellipsoid to determine Raman activity.

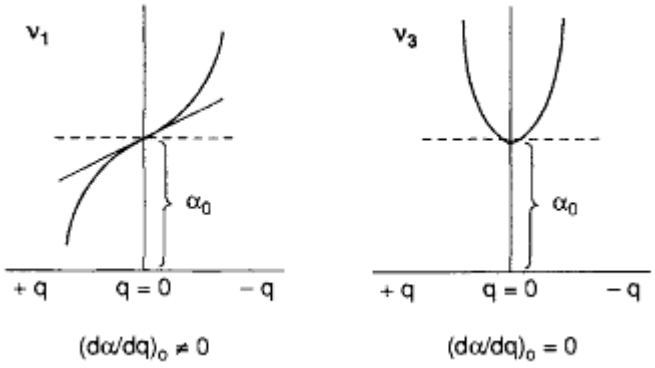

Figure 2.14 Difference between ν_1 and ν_3 vibrations in CO_2 molecule.

One should note that, in CO_2, the vibration that is symmetric with respect to the center of symmetry (ν_1) is Raman-active but not IR-active, whereas those that are antisymmetric with respect to the center of symmetry (ν_2 and ν_3) are IR-active but not Raman-active. This condition is called the mutual exclusion principle and holds for any molecules having a center of symmetry.

Although IR and Raman spectroscopies are similar in that both techniques provide information on vibrational frequencies, there are many advantages and disadvantages unique to each spectroscopy. Some of these are listed here.

1. As stated above, selection rules are markedly different between IR and Raman spectroscopies. Thus, some vibrations are only Raman-active while others are only IR-active. Typical examples are found in molecules having a center of symmetry for

which the mutual exclusion rule holds. In general, a vibration is IR-active, Raman-active, or active in both; however, totally symmetric vibrations are always Raman-active.

2. Some vibrations are inherently weak in IR and strong in Raman spectra. Examples are the stretching vibrations of the C≡C, C=C, P=S, S—S and C—S bonds. In general, vibrations are strong in Raman if the bond is covalent and strong in IR if the bond is ionic (O—H, N—H). For covalent bonds, the ratio of relative intensities of the C≡C, C = C and C—C bond stretching vibrations in Raman spectra is about 3:2:1. Bending vibrations are generally weaker than stretching vibrations in Raman spectra.

3. Measurements of depolarization ratios provide reliable information about the symmetry of a normal vibration in solution. Such information can not be obtained from IR spectra of solutions where molecules are randomly orientated.

4. Using the resonance Raman effect, it is possible to selectively enhance vibrations of a particular chromophoric group in the molecule. This is particularly advantageous in vibrational studies of large biological molecules containing chromophoric groups.

5. Since the diameter of the laser beam is normally 1-2mm, only a small sample area is needed to obtain Raman spectra. This is a great advantage over conventional IR spectroscopy when only a small quantity of the sample (such as isotopic chemicals) is available.

6. Since water is a weak Raman scatterer, Raman spectra of samples in aqueous solution can be obtained without major interference from water vibrations. Thus, Raman

spectroscopy is ideal for the studies of biological compounds in aqueous solution. In contrast, IR spectroscopy suffers from the strong absorption of water.

7. Raman spectra of hygroscopic and/or air-sensitive compounds can be obtained by placing the sample in sealed glass tubing. In IR spectroscopy, this is not possible since glass tubing absorbs IR radiation.

8. In Raman spectroscopy, the region from 4,000 to 50 cm^{-1} can be covered by a single recording. In contrast, gratings, beam splitters, filters and detectors must be changed to cover the same region by IR spectroscopy.

Some disadvantages of Raman spectroscopy are the following:

1. A laser source is needed to observe weak Raman scattering. This may cause local heating and/or photodecomposition, especially in resonance Raman studies where the laser frequency is deliberately tuned in the absorption band of the molecule.

2. Some compounds fluoresce when irradiated by the laser beam.

3. It is more difficult to obtain rotational and rotation-vibration spectra with high resolution in Raman than in IR spectroscopy. This is because Raman spectra are observed in the UV-visible region where high resolving power is difficult to obtain.

4. The state of the art Raman system costs much more than a conventional FT-IR spectrophotometer although less expensive versions have appeared which are smaller and portable and suitable for process applications.

2.1.7 Reaction Rate Theory

A simple reaction between two species, A and B, to form a third species, C, is described by [107]:

$$aA + bB \leftrightarrow cC \tag{2.13}$$

where a, b, and c are the numbers of atoms or molecules of each species that are involved in the reaction. The equilibrium constant, K, for the reaction is given by:

$$K = \frac{[C]^c}{[A]^a [B]^b} \tag{2.14}$$

where the square brackets indicate the number of atoms or molecules of the species per unit volume, for example:

$$[C] = \frac{n_c}{V} \tag{2.15}$$

The equilibrium constant, K, gives the ratio of the concentration of the product to the concentrations of the reactants.

The reaction path between the reactants and the product for the reaction:

$aA + bB \leftrightarrow cC$

is illustrated schematically in Figure 2.15.

G_1 and G_2 are the free energies in the initial and final states, respectively, and G* is the highest free energy along the reaction path. G* depends on the reaction path as A and B come together, and can be different for different conditions, for example, when a catalyst is present. For simple cases, the energy along the reaction path can be calculated from quantum mechanics. The reaction rate for the reaction in Figure 2.15 is proportional

to the number of A atoms per unit volume, times the probability that a B atom will be next to it, times the probability that they will have enough energy to get over the barrier to the reaction:

$$[A][B]\exp[-(G^*-G1)/kT] \tag{2.16}$$

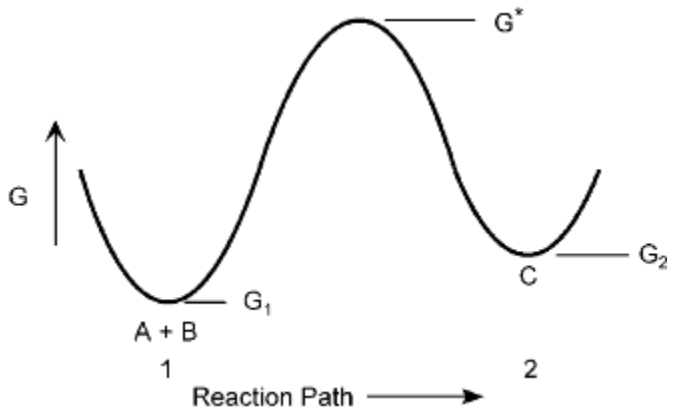

Figure 2.15 Free-energy variation along the reaction path.

where kT is Boltzmann's constant times the temperature. At equilibrium, this forward rate will be equal to the reverse rate:

$$[C]\exp[-(G^*-G2)/kT] \tag{2.17}$$

Therefore we have:

$$[C]=[A][B]\exp[-(G2-G1)/kT]=[A][B]\exp(-\frac{\Delta G}{kT}) \tag{2.18}$$

Where $\Delta G = G2 - G1$.

The equilibrium constant is thus:

$$K=\exp(-\Delta G/kT) \tag{2.19}$$

It depends only on the free energies of the initial and final states. It does not depend on the reaction path, which determines the rates, or on how long it takes to reach equilibrium. In a reaction starting with only reactants A and B present, the number of product species will increase and the number of reactants will decrease until the net rate is zero.

For a reaction

$$aA + bB \rightarrow cC \tag{2.20}$$

with no back flux, the rate of production of C is:

$$\frac{1}{V}\frac{dn_c}{dt} = \frac{d}{dt}[C] = k^* [A]^{\alpha} [B]^{\beta} \tag{2.21}$$

where k* is the reaction rate constant. α and β are not necessarily equal to a and b, but they are usually close. Valuable information about many reactions can be obtained from the order of the reaction, which is defined as follows:

The overall reaction is of order α+β.

The reaction is of order α in A.

The reaction is of order β in B.

For the reaction:

$aA + bB \rightarrow cC$

There will be no back flux if the free energy in state 2 is very low, so that G*–G2 is large, as illustrated in Figure 2.16.

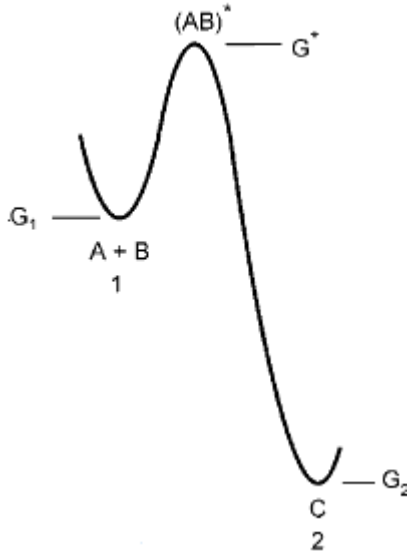

Figure 2.16 Free-energy variation along the reaction path with no back flux.

We assume that there is a transition state complex (AB)* that has free energy corresponding to the maximum along the reaction path, and that the concentration of this complex is in equilibrium with the reactants. The equilibrium constant for this transition state is:

$$K^*[A][B] = [(AB)^*] = [A][B]\exp[-(G^* - G1)/kT] \tag{2.22}$$

The rate of formation of the product C is a frequency times the concentration of the transition state. The frequency is usually taken to be approximately the Debye frequency, kT/h, where h is Planck's constant.

$$\frac{d[C]}{dt} = k^*[A][B] = \frac{kT}{h}[(AB)^*] \tag{2.23}$$

So the reaction rate constant, k*, is approximately given by:

$$k^* = \frac{kT}{h}K^* = \frac{kT}{h}\exp(-\Delta G^*/kT) \tag{2.24}$$

Where $\Delta G^* = G^* - G1$.

Writing $\Delta G^* = \Delta H^* - T\Delta S^*$, the reaction rate constant can be written as k_0^* times a Boltzmann factor:

$$k^* = k_0^* \exp(-\Delta H^* / kT) \tag{2.25}$$

Where:

$$k_0^* = \frac{kT}{h} \exp(\Delta S^* / R) \tag{2.26}$$

2.1.8 Phase Equilibrium, Supersaturation and Nucleation

The equilibrium between two infinitely large phases α and β is determined by the equality of their chemical potentials μ_α and μ_β. The latter represent the derivation of the Gibbs free energies with respect to the number of particles in the system at constant pressure P and temperature T. $\mu = (\partial G / \partial n)_{P,T}$, or in other words, the work which has to be done in order to change the number of particles in the phase by unity. In the simplest case of a single component system we have

$$\mu_\alpha(P,T) = \mu_\beta(P,T) \tag{2.27}$$

The above equation means that the pressure and the temperatures in both phases are equal. The requirement $P_\alpha = P_\beta = P$ is equivalent to the condition that the boundary dividing both phases is flat or, in other words, that the phase are infinitely large.

Now assume that the pressure and the temperature are infinitesimally changed in such a way that the two phases remain in equilibrium, i.e.

$$\mu_\alpha + d\mu_\alpha = \mu_\beta + d\mu_\beta \tag{2.28}$$

Combine (2.27) and (2.28) we have:

$$d\mu_\alpha(P,T) = d\mu_\beta(P,T) \tag{2.29}$$

Recalling the properties of the Gibbs free energy ($dG = VdP - SdT$), (2.29) can be rewritten in the form of:

$$-s_\alpha dT + v_\alpha dP = -s_\beta dT + v_\beta dP \tag{2.30}$$

Where s_α and s_β are the molar entropies, and v_α and v_β are the molar volumes of the two phases in equilibrium with each other.

Rearranging (2.30) gives the well-known equation of Clapeyron:

$$\frac{dP}{dT} = \frac{\Delta s}{\Delta v} = \frac{\Delta h}{T\Delta v} \tag{2.31}$$

Where $\Delta s = s_\alpha - s_\beta$, $\Delta v = v_\alpha - v_\beta$, and $\Delta h = h_\alpha - h_\beta$ is the enthalpy of the corresponding phase transition.

Consider the first case when the phase β is one of the condensed phase, say, the liquid phase and the phase α is the vapor phase. Then the enthalpy change Δh will be the enthalpy of evaporation $\Delta h_{ev} = h_v - h_l$ and v_l and v_v will be the molar volumes of the liquid and the vapor phases, respectively. The enthalpy of evaporation is always positive and the molar volume of the vapor v_v is usually much greater than that of liquid v_l. In other words the slope dP/dT will be positive. We can neglect the molar volume of the crystal with respect to that of the vapor and to assume that the vapor behaves as an ideal gas, i.e. $P = RT/v_v$. The Eq. (2.31) attains the form:

$$\frac{d\ln P}{dT} = \frac{\Delta h_{ev}}{RT^2} \tag{2.32}$$

Which is well-known as the equation of Clapeyron-Clausius. Replacing Δh_{ev} with the enthalpy of sublimation Δh_{sub} we obtain the equation which describes the crystal-vapor equilibrium.

Assuming Δh_{ev} (or Δh_{sub}) does not depend on the temperature, Eq. (2.32) can be easily integrated to:

$$\frac{P}{P_0} = \exp\left[-\frac{\Delta h_{ev}}{R}\left(\frac{1}{T} - \frac{1}{T_0}\right)\right] \tag{2.33}$$

Where P_0 is the equilibrium pressure at some temperature T_0.

In the case of the crystal melt equilibrium the enthalpy Δh is equal to the enthalpy of melting Δh_m which is always positive and the equilibrium temperature is the melting point T_m.

As a result of the above considerations we can conduct the phase diagram of our single component system in co-ordinates P and T (Figure 2.17).

The enthalpy of sublimation of crystals Δh_{sub} is greater than the enthalpy of evaporation Δh_{ev} of liquid and hence the slope of the curve in the phase diagram giving the crystal-vapor equilibrium is greater than the slope of the curve of the liquid vapor equilibrium. On the other hand the molar volume v_l of the liquid phase is usually greater than that of the crystal phase v_c (with some very rare but important exceptions, for example, in the case of water and bismuth), but the difference is small so that the slope dP/dT is great, in fact, much greater than that of the other two cases and is also positive with the exception of the cases mentioned above. Thus the $P-T$ space is

divided into three parts. The crystal phase is thermodynamically favored at high pressure and low temperatures. The liquid phase is stable at high temperatures and high pressures and the vapor phase is stable at high temperatures and low pressures. Two phases are in equilibrium along the lines and the three phases are simultaneously in equilibrium in the so-called triple point O. The liquid-vapor line terminates at the so-called critical point O' beyond which the liquid phase does not exist any more because the surface energy of the liquid becomes equal to zero and the phase boundary between both phases disappears.

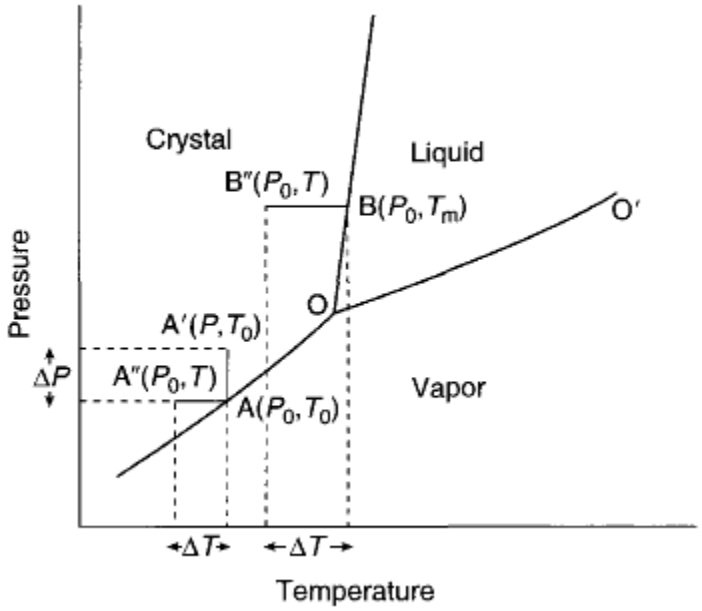

Figure 2.17 Phase diagram of a single component system in $P-T$ coordinates. O and O' denote the triple point and the critical point, respectively. The vapor phase becomes supersatured or undercooled with respect to the crystalline phase if one moves along the line AA' or AA''. The liquid phase becomes undercooled with respect to the crystalline phase if one moves along the line BB''. ΔP and ΔT are the supersaturation and undercooling.

When moving along the dividing lines the corresponding phases are in equilibrium, i.e. Eq. (2.27) is strictly fulfilled. If the pressure or the temperature is changed in such a way that we deviate from the lines of the phase equilibrium one or another phase becomes stable. This means that its chemical potential becomes smaller than the chemical potentials of the phases in the other regions. Any change of the temperature and/or pressure which leads to change of the the region of stability leads in turn to transition from one phase to another. Thus the decrease of the temperature or the increase of the pressure leads to crystallization or liquefaction of the vapor, the decrease of the temperature leads to solidification of the liquids. Figure 2.18 shows the variation of the chemical potentials of the crystal and vapor phases with the pressure at a constant temperature.

The chemical potential of the vapor increases with the pressure following the logarithmic law which corresponds to a shift along the line AA' in Figure 2.17. At the same time the chemical potential of the crystal phase is a linear function of the pressure its slope being given by the molecular volume v_c. Both curves intersect at the equilibrium pressure P_0. At pressure smaller than P_0 the chemical potential of the crystal is greater than that of the vapor and the crystal should sublimate. In the opposite case $P > P_0$ the vapor should crystallize. The difference of the chemical potentials, which is a function of the pressure, represents the thermodynamic driving force for crystallization to occur. It is called supersaturation and is defined as the difference of the

chemical potentials $\Delta\mu$ of the infinitely large mother and new phases at the particular value of the temperature. In other words we have (Figure 2.18):

$$\Delta\mu = \mu_v(P) - \mu_c(P) \tag{2.34}$$

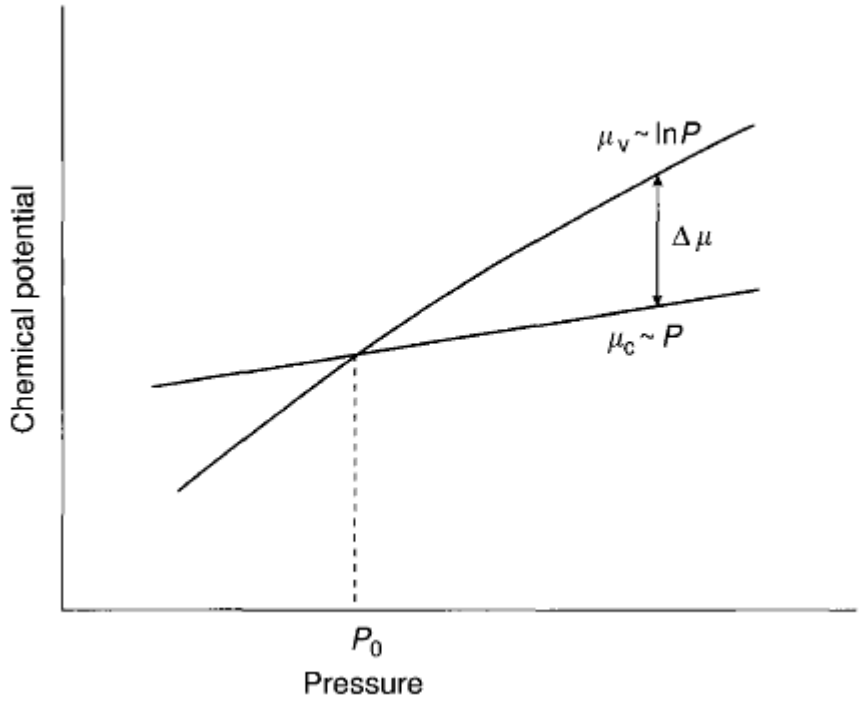

Figure 2.18 Dependance of the chemical potentials of the vapor, μ_v, and the crystal, μ_c on the pressure when one moves along the line AA' in Figure 2.17. P_0 denotes the equilibrium pressure.

Bearing in mind Eq. (2.27), or $\mu_v(P_0) = \mu_c(P_0)$, we can rewrite Eq. (2.34) in the form:

$$\Delta\mu = \left[\mu_v(P) - \mu_v(P_0)\right] - \left[\mu_c(P) - \mu_c(P_0)\right] \tag{2.35}$$

For small deviations from equilibrium the above equation turns into

$$\Delta\mu \cong \int_{P_0}^{P} \frac{\partial\mu_v}{\partial P} dP - \int_{P_0}^{P} \frac{\partial\mu_c}{\partial P} dP = \int_{P_0}^{P} \left(v_v - v_c\right) dP \cong \int_{P_0}^{P} v_v dP \tag{2.36}$$

Treating the vapor as an ideal gas ($v_v = kT / P$) we obtain upon integration

$$\Delta\mu = kT \ln \frac{P}{P_0} \tag{2.37}$$

Where P_0 is the equilibrium vapor pressure of the infinitely large crystal phase at the given temperature.

Without going into details we can write an expression for the supersaturation in the case of crystallization from solution, when the solution is treated as ideal, in the form

$$\Delta\mu = kT \ln \frac{C}{C_0} \tag{2.38}$$

Where C and C_0 are, respectively, the real and the equilibrium concentrations of the solute. In fact a more rigorous treatment requires the condensation of multicomponent systems.

Figure 2.19 shows the variation of the chemical potentials of the crystal and liquid phases with the temperature at a constant pressure (the line BB'' in Figure 2.17). The supersaturation which in this case is frequently called undercooling is again defined as the difference of the chemical potentials of the infinitely large liquid and crystal phases, μ_l and μ_c, respectively, at a given temperature

$$\Delta\mu = \mu_l(T) - \mu_c(T) \tag{2.39}$$

Following the same procedure as above we obtain:

$$\Delta\mu = \left[\mu_l(T) - \mu_l(T_m)\right] - \left[\mu_c(T) - \mu_c(T_m)\right] \cong \int_{T_m}^{T} \frac{\partial \mu_l}{\partial T} dT - \int_{T_m}^{T} \frac{\partial \mu_c}{\partial T} dT = \int_{T}^{T_m} \Delta s_m dT \tag{2.40}$$

Assuming the entropy of melting $\Delta s_m = s_l - s_c$ is independent of the temperature one obtains after integration

$$\Delta\mu = \Delta s_m (T_m - T) = \frac{\Delta h_m}{T_m}\Delta T \tag{2.41}$$

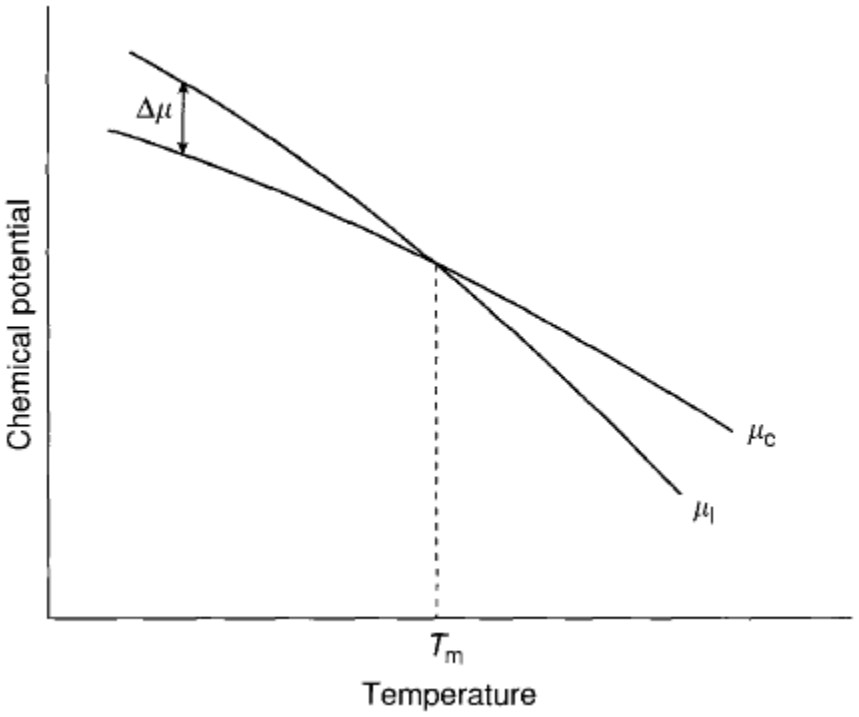

Figure 2.19 Dependance of the chemical potentials of the liquid phase, μ_l, and the crystal phase, μ_c, on the temperature when one moves along the line BB'' in Figure 2.17. The melting point is denoted by T_m.

Obviously, Eq. (2.41) is also applicable to the case of crystallization of undercooled vapor after the enthalpy of melting is replaced by the enthalpy of sublimation (the line AA' in Figure 2.17).

Finally, in the particular case of electrocrystallization of metals the supersaturation is given by:

$$\Delta\mu = ze\eta \tag{2.42}$$

Where z denotes the valence of the neutralizing ions, $e = 1.60219 \times 10^{-19} C$ is the elementary electric charge and $\eta = E - E_0$ is the so-called overvoltage or overpotential given by the difference of the equilibrium potential E_0 of the deposited metal in the solution and the electrical potential E applied from outside.

It was Max Volmer who introduced the term "Überschreitung" or "step across" for both the supersaturation and the undercooling to denote the transition through the line of co-existence of the two phases. Thus, the difference of the chemical potentials of the infinitely large new and mother phases appears as a measure of deviation from the phase equilibrium and determines the rate of the transition from one phase to another.

Nucleation is the extremely localized budding of a distinct thermodynamic phase. There is usually a barrier to the formation of a new phase: the formation of a liquid in a gas, a solid in a gas, bubbles in a liquid, crystals in a liquid, precipitates in a solid, domains of reverse magnetization, etc. The formation of a new phase begins with a small nucleus, which grows by atoms joining and leaving it. This barrier controls the rate of formation of the new phase. (In some instances, there is no barrier to the formation of a new phase, for example, in systems with a critical point, it is possible to go continuously from one phase to another. There is also a process known as phase separation where one phase spontaneously decomposes into two phases.)

There are two classes of nucleation events, known as homogeneous and heterogeneous nucleation. Homogeneous nucleation involves the spontaneous formation and subsequent growth of small particles of the new phase. In heterogeneous nucleation, the new phase is initiated on a foreign material such as a particle or a surface layer. Homogeneous nucleation occurs when there are no heterogeneous nuclei present. A heterogeneous nucleating agent provides a lower barrier to the initial formation of the new phase. Most nucleation processes in the real world are heterogeneous, but the process depends on the nucleating agent involved, and so the details defy a generic description. The homogeneous nucleation process involves only the one material, and so it is intrinsic to the material. The conditions for homogeneous nucleation in to occur represent a limit on the stability of the phase. It can be analyzed more readily than heterogeneous nucleation that involves a foreign, often unknown, material. Volmer [108] invented nucleation theory to explain the strange melting and freezing behavior of materials. Most materials melt at their melting points. Theories of phase-transformation kinetics were available, but some liquids could be undercooled a lot, and others could be undercooled only little, or not at all. The behavior of various materials was different, and even the behavior of one material was erratic and could vary from one sample to another. Volmer addressed the question: Why can liquids be undercooled?

Volmer started from the fact that small particles are less stable than the bulk phase because of their surface tension, and so it is difficult to form a small particle. And this

creates a barrier to the formation of a new phase. He suggested that the formation of small particles depends on fluctuations.

A supercooled liquid is metastable. It is stable in the absence of the solid phase, but it is not the lowest free energy state. Volmer considered the question: What is the probability of a fluctuation that is big enough to make a stable bit of the new phase?

He assumed that the change in free energy when a cluster of atoms of the new phase formed could be described by two contributions, one from the decreased free energy associated with the formation of the new phase, and the other from the surface tension of the small cluster. Assuming that the cluster of atoms of the new phase is a sphere of radius r, the change in free energy when the cluster forms can be written in terms of these two contributions:

$$\Delta G_r = -\Delta G_V \frac{4}{3}\pi r^3 + \sigma 4\pi r^2 \qquad (2.43)$$

Here ΔG_V is the change in free energy per unit volume associated with the transformation, and σ is the surface tension, or specific surface free energy. For a liquid that is supercooled below its melting point, we can write $\Delta G_V \approx L\Delta T / T_M$, where ΔT is the undercooling, and L is the latent heat.

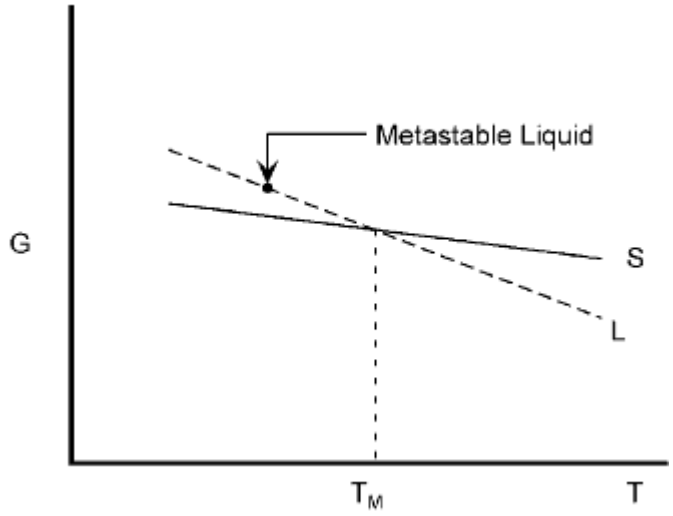

Figure 2.20 Free energy versus temperature for a solid and a liquid.

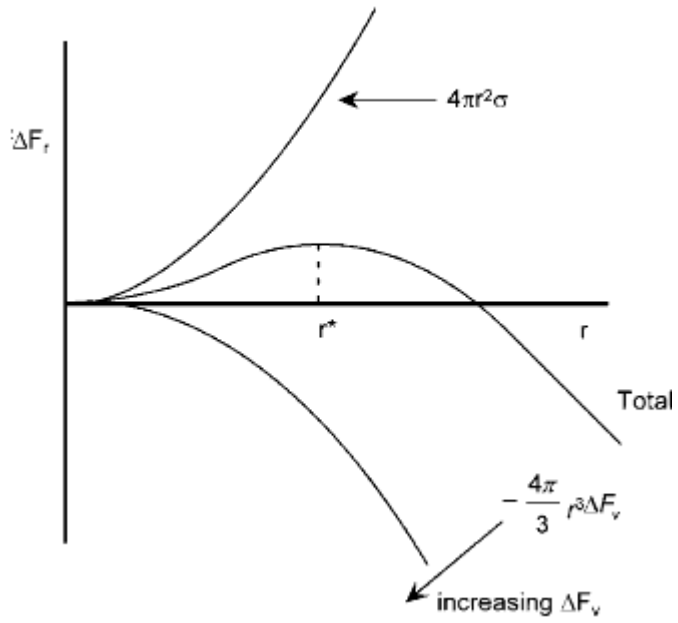

Figure 2.21 Free energy of a cluster of atoms for various radii of the cluster.

Figure 2.21 is a plot of the total free energy of the cluster, ΔG_r, for various sizes of cluster. The total surface area of the cluster increases as r^2, and the volume free-energy

term decreases as r^3. The magnitude of the volume term depends on the undercooling. For a finite undercooling, the volume free-energy term will dominate for large radius: a large enough crystal will grow. Very small crystals can reduce their free energy by shrinking. The transition between these two regions is at the maximum in the total free-energy curve, which occurs at the critical radius, r*. The value of r*, which is the radius corresponding to the maximum in the free energy, is given by:

$$\frac{\Delta G_r}{dt} = 0 = -4\pi r^2 \Delta G_V + 8\pi r\sigma \tag{2.44}$$

So that the critical radius is:

$$r^* = \frac{2\sigma}{\Delta G_V} = \frac{2\sigma T_M}{L\Delta T} \tag{2.45}$$

Volmer made use of the fact that the probability of finding a fluctuation of energy, W, is given by a Boltzmann factor:

$$\exp(-W/kT) \tag{2.46}$$

The probability of finding a cluster of size r* should then be given Eq. 2.46 with W given by the free energy required to from the cluster. The free energy to form a cluster of size r* is obtained by substituting the value for r* from Eq 2.45 into Eq. 2.43:

$$\Delta G_{r^*} = \frac{16}{3}\frac{\pi\sigma^3}{(\Delta G_V)^2} \tag{2.47}$$

and so the probability of finding a cluster of size r* among N atoms is:

$$\frac{N_{r^*}}{N} = \exp\left(-\frac{\Delta G_{r^*}}{kT}\right) = \exp\left(-\frac{16\pi\sigma^3}{3kT(\Delta G_V)^2}\right) \tag{2.48}$$

In general, the total free energy of a critical cluster, ΔG_{r*}, includes strain energy, magnetic energy, electrical energy, etc., in addition to the volume free-energy and surface free-energy terms. If they are relevant, these contributions should be added to obtain the total free energy of the critical cluster. The free energy in Eq. 2.48 was calculated for a spherical cluster, but the energy in the exponent should always be simply the total free energy to form the critical nucleus.

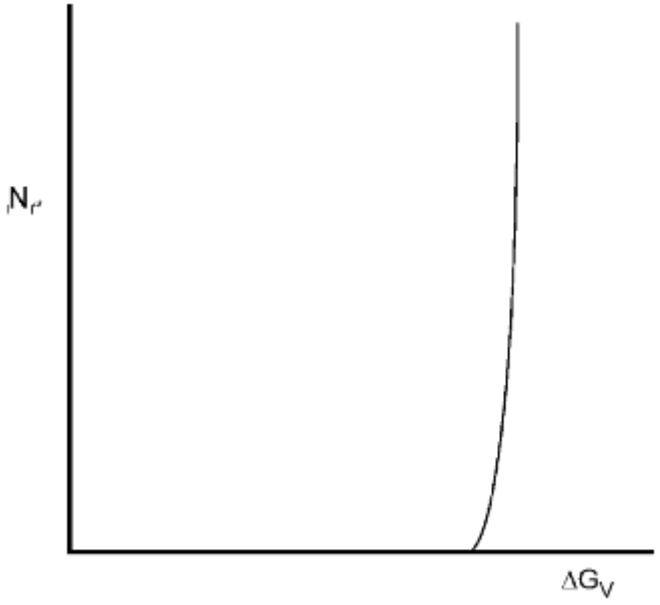

Figure 2.22 Number of critical nuclei as a function of undercooling.

For homogeneous nucleation of a solid in an undercooled liquid, there are typically about 300 atoms in a cluster of critical size. The total free energy to form a cluster is the total change in free energy for all 300 atoms. So the number in the exponent can be very large. For small undercooling, ΔG_V is small, so the exponent is large and negative, implying very few critical nuclei. For larger undercooling, the volume free

energy becomes comparable to the surface free energy. When this happens, the exponent switches from being large to being small in a small temperature interval. The probability of finding a nucleus of critical size increases abruptly in a small temperature interval, as illustrated in Figure 2.22.

For undercooled metals, the mobility of the atoms in the liquid is large, so the distribution of solid-like clusters in the liquid can change rapidly. Nucleation occurs very rapidly once the critical supercooling is reached. Supercritical clusters grow very rapidly, and their growth rate will be limited by heat flow. The latent heat of a typical metal is enough to raise its temperature by an amount that is about one third of its melting point. For most materials, homogeneous nucleation occurs at a supercooling of about 20%, that is, at a temperature that is about 0.8 T_M . The latent heat released by freezing of a sample at 0.8 T_M is more than enough to heat the sample to the melting point. And so the nucleation process is terminated after a few nucleation events by the rapid growth and the associated heating of the sample.

In a glass, the situation is quite different. The rate at which the cluster distributions can change is slow, and the growth rate of critical nuclei is also slow. The growth rate is so slow that heat flow is not an issue. So a nucleus can form at one place and the supercooling is still maintained in another part of the glass sample. And so the nucleation rate can be measured. Nucleation of a new solid phase in a solid is usually similar to this. There is usually a difficulty in fitting the nucleation data to the expected nucleation rate for glasses. But there are often defects in solids, and irregularities in the

structure of glasses. It is also difficult to measure surface tensions and to determine strain energy contributions in order to estimate the work required to form the nucleus.

For precipitation of oxygen in silicon, the oxygen moves interstitially through the lattice. The growth rate of the precipitate depends on the rate of motion of oxygen through the lattice. The oxygen precipitates as crystoballite, a form of SiO_2. An SiO_2 molecule occupies about the same volume as two silicon atoms in a silicon crystal. There is a significant stress generated at the precipitate, and the energy in the stress field is a major component of the total energy of the precipitate. Silicon atoms are forced into an interstitial position, and the precipitate blows out dislocation loops to relieve the stress. The stresses generated and the effects of the stress-relief mechanisms all contribute to the total work to form the precipitate.

Detailed experiments have been carried out studying the nucleation of liquid droplets in clean vapor. The surface tension of the liquid can be measured readily, and the clusters of liquid in the vapor phase are likely to be spherical. The experimental data on these systems verify the validity of the nucleation equations.

Continuous nucleation of particles can occur in a stream of hot atoms or molecules coming from a high-temperature source, or expanding and cooling in a jet coming from a high-pressure source. There can be a steady-state nucleation process where particles nucleate continuously at some distance down stream from the source.

Producing good quality crystals of a suitable size is the first and most important step in determining any crystal structure. Crystallization is the process of arranging atoms

or molecules that are in a fluid or solution state into an ordered solid state. This process occurs in two steps--nucleation and growth. Nucleation may occur at a seed crystal, but in the absence of seed crystals usually occurs at some particle of dust or at some imperfection in the surrounding vessel. Crystals grow by the ordered deposition of material from the fluid or solution state to a surface of the crystal.

The shapes of crystals depend on both the internal symmetry of the material and on the relative growth rate of the faces. In general, the faces of the crystal that grow most rapidly are those to which the crystallizing particles are bound most securely. These rapidly growing faces are usually the smaller, less well developed faces. Thus, the larger faces are usually associated with directions in the crystal where there are only weak intermolecular interactions.

There are numerous ways to grow crystals [109-118]. The choice of method depends greatly upon the physical and chemical properties of the sample. For solution methods of crystallization, the solubility of the sample in various solvent systems must be explored. If heating methods are selected for growing crystals, the thermal stability and melting point of the sample should be determined.

There are a few general points that apply to all crystallization methods.

* It is important that the sample be as pure as possible. When crystallization attempts consistently yield oils, the sample is probably not pure. The solvents or cocrystallizing materials should be as pure as possible. Contaminants may often break down the desired sample.

* It is important for most solution methods that the glassware be thoroughly clean and "old" or "used." New glassware is so smooth that there are no nucleation sites available on the exposed surfaces. Also, new glassware from the manufacturer usually has a variety of dusty contaminants.

* If a sample only yields small crystals, the method should be altered so as to slow down the growth step. Slowing the crystal growth sometimes requires changing the method used to grow the crystals.

* Avoid vibrations near growing crystals.

* Some methods work in a few hours, and other methods require weeks or even months for success.

2.1. 9 Crystal Growth Techniques

Crystal can be grown from melt, solution or vapor phase. Crystals will grow from a melt much more rapidly than they will grow from the vapor phase or from a solution. This is simply because the density of material in the melt is comparable to that in a crystal, so the atoms or molecules are essentially there already to grow the crystal. For both vapor and solution growth, the density of atoms or molecules in the mother phase is much lower, and the growth rate depends on the rate at which they arrive at the surface of the crystal. For the commercial growth of crystals, the faster those crystals of acceptable quality can be grown, the better. This is also true for the non-commercial growth of experimental crystals. So melt growth is the preferred method. There are various reasons why many

crystals cannot be grown from the melt, but if a crystal can be grown from its melt, it will be.

(1) Melt Growth

There are several different schemes for melt growth [119, 120]. In melt growth, the intrinsic growth process is usually so rapid that the growth is controlled by heat flow. The various schemes differ primarily in the configuration of the growth apparatus.

Czochralski Growth

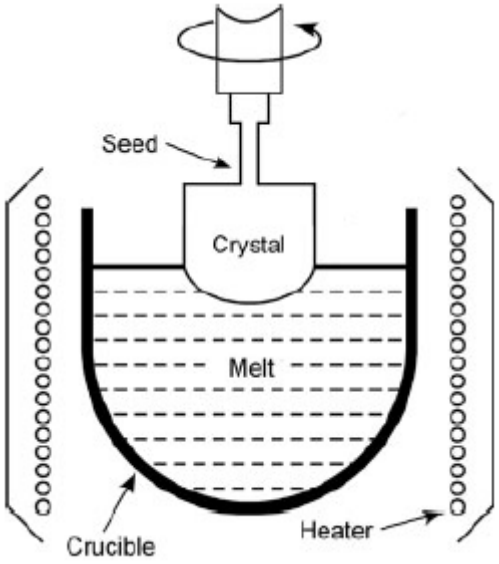

Figure 2.23 Schematic drawing of Czochralski crystal growth apparatus.

The Czochralski process (Figure 2.23) is a method of crystal growth used to obtain single crystals of semiconductors (e.g. silicon, germanium and gallium arsenide), metals (e.g. palladium, platinum, silver, gold), salts, and synthetic gemstones. The process is named

after Polish scientist Jan Czochralski, who discovered the method in 1916 while investigating the crystallization rates of metals.

The most important application may be the growth of large cylindrical ingots, or boules, of single crystal silicon. Other semiconductors, such as gallium arsenide, can also be grown by this method, although lower defect densities in this case can be obtained using variants of the Bridgman-Stockbarger technique.

Floating Zone

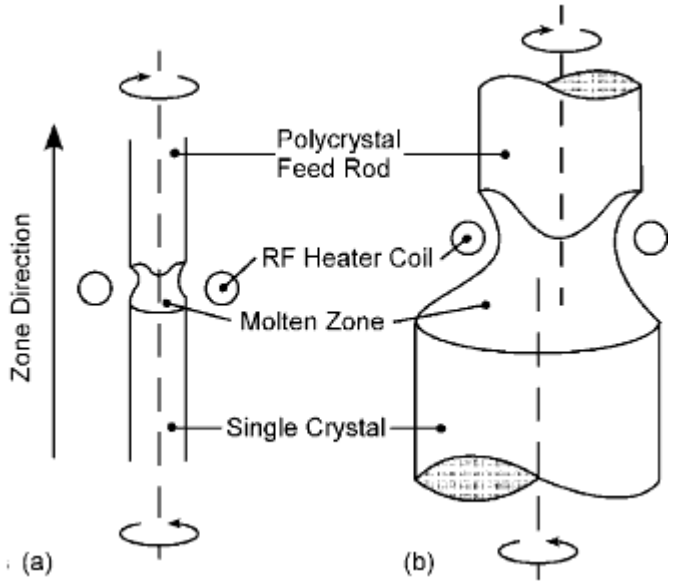

Figure 2.24 Floating zone crystal growth.

The floating zone method is used to make high-resistivity silicon crystals, which are used to make power-handling devices. The crystals do not contain oxygen, and so have resistivities as high as 10,000 ohm-centimeters, instead of 10 ohm-centimeters, which is typical for Czochralski silicon. This method does not require a container for the liquid.

Instead, the liquid is held in place by surface tension, as illustrated in Figure 2.24. Growth proceeds by moving the heater coil, which moves the liquid zone, upwards.

On the left is axi-symmetric growth with the feed rod the same diameter as the final crystal. This method usually results in a single torroidal flow pattern in the liquid, and so the center of the liquid zone is not heated very efficiently. In the scheme shown on the right, which is the more usual configuration, the feed rod has a smaller diameter than the growing crystal. The smaller diameter feed rod is off-center, and this configuration results in a single horizontal convective roll in the melt, which heats the center of the liquid efficiently. The feed rod must be moved relative to the growing crystal at a different rate from that of the heater coil.

This method requires the preparation of the seed rod of appropriate diameter in a separate zone melting run, making this a more costly process than Czochraski growth. Semiconductor device people have learned to live with the oxygen in Cz silicon, and even turn it to advantage for internal gettering. For power-transmission devices, the higher resistivity of floating zone silicon results in a higher breakdown voltage, which makes the extra cost worthwhile.

A variant on the floating zone method has been used to grow single crystal rods with small cross sections of high melting point oxides. A high-power laser or lasers are focused onto the rod to create a molten zone, and the molten zone is moved along the rod to achieve growth. This is usually done for high melting point oxide materials that are

stable in air. The temperature gradients in the rod during growth are very large, because heat is lost rapidly by radiation.

Bridgman Method

In the simple version of Bridgman growth the sample is contained in a tube, as illustrated schematically in Figure 2.25.

Initially the sample is heated in the furnace, and melted completely. It is then lowered slowly from the furnace. The crystal nucleates when the bottom end of the container gets cold enough. The bottom end of the container is usually tapered to a point to minimize the probability of forming many nuclei. In principle, a seed crystal can be used in the bottom end of the container, but in practice, it is difficult to see the interface in the seed in order to determine when it is partly melted. If the starting material, which is usually polycrystalline, is not all melted, or if the seed melts completely, then the seeding process fails. And usually the time interval between these two events is short. So Bridgman growth is usually unseeded, and the orientation of the resultant crystal is random.

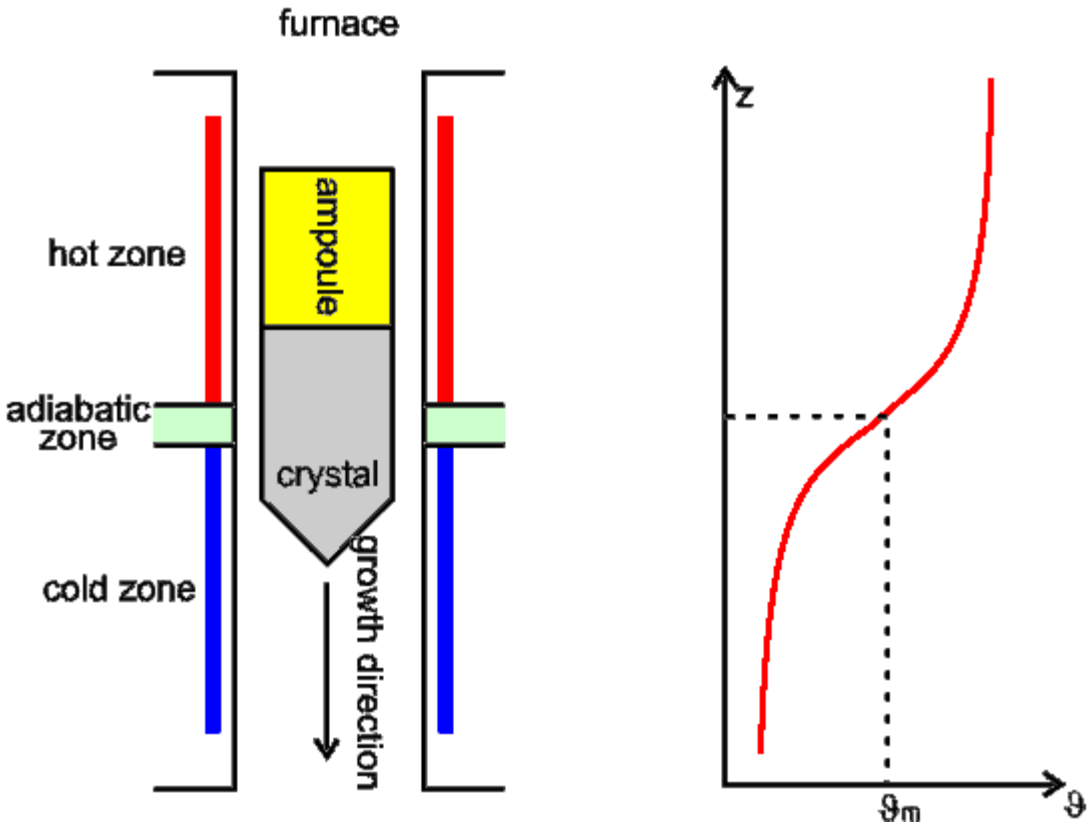

Figure 2.25 Schematics of Bidgman furnace and heating distribution

In more sophisticated setups, baffles or multi-zone heaters are used to control the temperature of the sample. Special precautions are usually necessary to remove the crystal from the tube after growth.

Chalmers Method

The Chalmers method is similar to the Bridgman method, except that the sample is held in an open, horizontal boat rather than in a vertical tube. Either the boat is withdrawn from a stationary furnace, or the furnace is withdrawn slowly from around the boat. In this configuration, the position of the interface can be observed on the top surface of the

sample. This permits the use of a seed in one end of the boat, so that the partial melting of the seed can be controlled. The boat can be made with sloping sides to facilitate the removal of the crystal.

Horizontal Gradient Freeze

This method is similar to the Chalmers method, except that the sample is contained in a multi-zone furnace. The temperature gradient in the crystal is imposed by the various heating zones. The boat and furnace are not moved relative to each other, but rather the crystal is grown by lowering the temperature of each zone in the furnace, usually with computer control.

There is also a method called vertical gradient freeze, which is a vertical version of this scheme; the Bridgman method without any moving parts.

(2) Solution Growth

Crystals are grown from solution only if they cannot be grown from their melt. There are several reasons why certain crystals cannot be grown from their melt. Crystal growth from the melt requires that the molecules that make up the crystal should not decompose below the melting point. It requires that the material not sublime below the melting point, although this can be circumvented for some materials with a high pressure growth apparatus. It requires that the material should melt congruently. It requires that there

should not be a solid-state phase transformation between the melting point and room temperature that will destroy the single crystal on cooling.

A variety of solvents are used for growing crystals from solution.

Growth from Aqueous Solutions

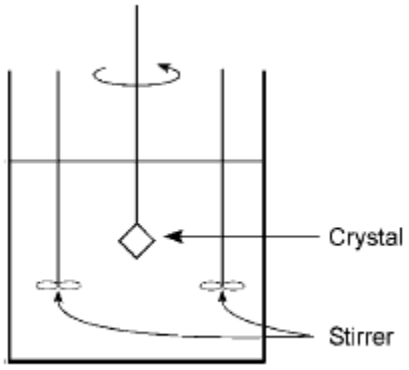

Figure 2.26 Apparatus for growth from an aqueous solution.

Water-soluble crystals are grown from aqueous solutions, in an apparatus such as is illustrated in Figure 2.26.

The growth is isothermal, and usually several weeks of growth is required to obtain a crystal of reasonable size. The growth is started from a seed that is suspended from a rod. The crystal is rotated, and the solution is stirred. The temperature of the solution may be lowered progressively to compensate for the depletion of the solution.

Flux Growth

Flux growth is solution growth where the solvent is a low-melting oxide. Often the flux is a mixture of boron oxide and lead oxide, and it is used to grow crystals of oxides, such as garnets. Many garnets cannot be grown directly from the melt, but the components of the garnet are soluble in the flux. The growth temperatures are usually much higher than the boiling point of water, so crystals cannot be grown from aqueous solutions. The growth crucible, which is usually platinum, is placed in a constant temperature furnace, without stirring. A cold finger is attached to the bottom of crucible to promote localized nucleation. Growth of a crystal of reasonable size usually takes several weeks.

Hydrothermal Growth

Hydrothermal growth uses superheated steam as the solvent. The crystals are grown in an autoclave, at a temperature and pressure above the critical point for water. Quartz crystals are grown hydrothermally because there is a transition from alpha to beta quartz at about 580 ℃, which destroys the crystal, so a crystal grown from the melt at 1700 ℃ does not survive on cooling to room temperature. Superheated steam is used as the solvent because SiO_2 is minimally soluble in anything else.

There are usually two temperature zones in the autoclave, separated by a perforated baffle. Nutrient material is placed in the higher-temperature zone, which is in the lower part of the chamber to promote convection, and seed crystals are suspended in the upper zone, at a lower temperature. The pressure is determined by the amount of

water added to the chamber. When heated to the operating temperature, this turns into pressurized, superheated steam. Typical operating conditions for growing quartz are 400 ℃ in the dissolving zone, 350 ℃ in the growth zone, with a pressure of about 2000 bars. The growth of a crystal of reasonable size takes several weeks. Natural quartz crystals and natural crystals of many other minerals are believed to have grown under conditions like this, well below the surface of the earth.

(3) Vapor-Phase Growth

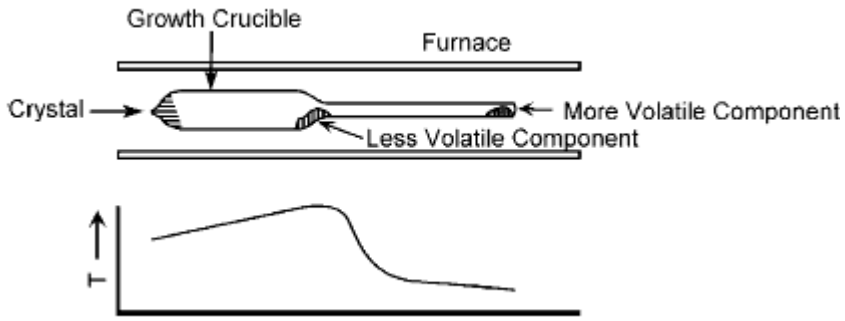

Figure 2.27 Vapor-phase growth of a compound from its components.

Growth from the vapor phase is very slow, so that only a few bulk crystals are grown by this method. On the other hand, thin films are usually deposited from the vapor phase, where deposition rates of a fraction of a micrometer per minute are tolerable. For growth from the vapor phase, the material should have high vapor pressure, and it should not decompose on vaporization if it is a compound. Alternatively, if the components have high vapor pressures, the desired compound can be assembled during deposition. One

such scheme is illustrated in Figure 2.27, where two components are vaporized separately, and combine at the growing crystal.

2.2 Experimental Method

Polycrystalline $FeSe_{1-x}$ samples were synthesized using the solid-state reaction method similar to that used in Ref [82]. High purity powder of desired selenium and iron compositions ($FeSe_{1-x}$ with $x \sim 0.03$) were mixed and grounded. The grounded powder was cold-pressed into discs, and the discs were sealed in an evacuated quartz tube and heat treated at 700 ℃ for 24 h. Samples were reground and sintered again at 700 ℃ for 24 h, and then annealed at 400 ℃ for 36 h. The last step was critical for avoiding the NiAs phase of FeSe. All samples were kept in vacuum desiccators before being put into the vacuum of the cryostat for measurement.

Raman scattering measurements were performed on a SPEX 500 M spectrometer combined with two Kaiser SuperNotch-plus notch filters and a Jobin-Yvon-Spex Spectrum one liquid nitrogen-cooled, back-illuminated CCD detector. A X10 long working distance Mitotoyo objective was employed to focus the laser beam from a Spectra Physics Ar^+ laser into a spot of about 10 mm in diameter on the sample surfaces, and to collect the scattered light. The 514.5 nm line, with plasmon lines filtered out by a bandpass filter, was used in this experiment. The laser beam is always kept below 10 mW to avoid laser heating. A Janis ST-300 liquid He continuous flow cryostat was used to control the temperature from 300 K to 5 K.

2.3 Result and Discussion

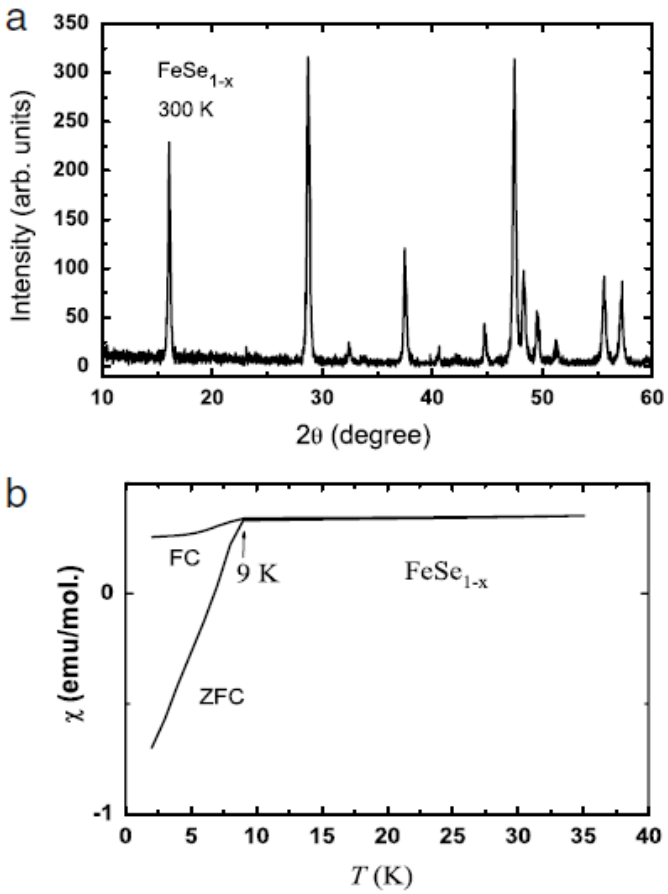

Figure 2.28 (a) The upper panel shows the X-ray diffraction pattern of $FeSe_{1-x}$ taken at room temperature. (b) The lower panel shows the temperature dependence of magnetization of $FeSe_{1-x}$ taken in zero-field cooling (ZFC) and field cooling (FC) with H = 10 Oe.

Fig. 2.28(a) shows the powder X-ray diffraction diagram of the sample that has been measured. It clearly shows a PbO-type structure and no trace of the NiAs phase. The low temperature magnetic susceptibility result, displayed in Figure 2.28(b), indicates that the superconducting transition occurs around 9 K, consistent with others' results [82,121,122]. Raman scattering experiments were subsequently performed on this sample down to 5 K, using the setup mentioned above, and the Raman spectra at a selected number of

temperatures are displayed in Figure 2.29. Below 200 cm^{-1}, one mode near 185 cm^{-1} was observed at room temperature. With decreasing temperature, this mode becomes sharper and more prominent, and its frequency increases slightly, as shown in the inset of Figure 2.30. Yet there is no noticeable discontinuity across the structural phase transition at 105 K and the superconducting transition around 9 K. The temperature dependences of frequency and line shape of this mode are very consistent with the Raman modes observed in the 1111 and 122 systems [123-125]. The mode frequency is also very close to the B1g phonon observed in $FeSe_{0.3}Te_{0.7}$ [126]. As mentioned above, systematic studies and assignments of Raman active phonons have been performed on the 1111 and 122 families based on single crystals data and factor group analysis [123-125], and they consistently show that the strongest two modes are the B_{1g} phonon near 200 cm^{-1} and a A_{1g} mode around 170 cm^{-1}.

In the Raman spectra of single crystal $FeSe_{0.3}Te_{0.7}$, only the B_{1g} mode near 190cm^{-1} has been observed. The mode around 185 cm^{-1} was thus assigned as the B_{1g} phonon mode in $FeSe_{1-x}$. The definitive assignment needs to wait for polarization-dependent Raman measurements on single crystal FeSe.

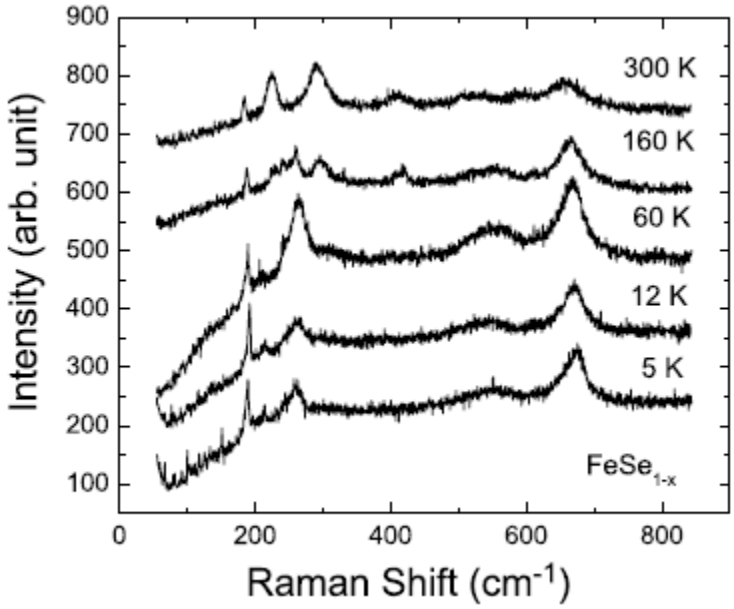

Figure 2.29 Raman spectra of $FeSe_{1-x}$ taken at five different temperatures from 300 K to 5 K. The spectra have been shifted vertically from each other for better view.

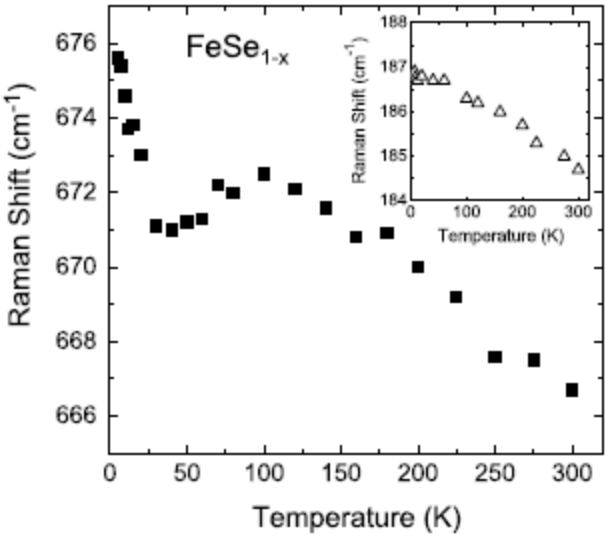

Figure 2.30 The temperature dependence of the highest frequency mode observed in the Raman spectra of $FeSe_{1-x}$. The Raman shift is obtained by a Lorentzian fitting of the mode. The inset shows the temperature dependence of the phonon mode. The phonon frequency is also obtained by fitting the spectra with a Lorentzian function.

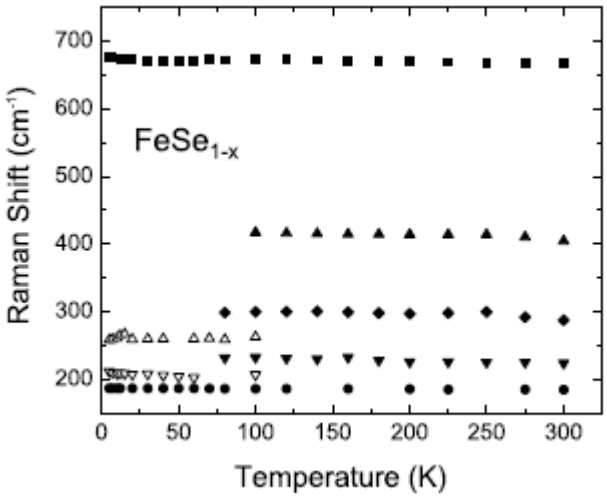

Fig. 2.31 The temperature dependence of all the Raman active modes observed in the Raman spectra of $FeSe_{1-x}$.

However, besides this phonon mode, a number of other modes that appear at higher frequency, as high as 670 cm^{-1}, were observed. Some of these modes are more prominent than the phonon mode, and their line widths are considerably broader. Using Lorentzian function to fit these modes, their frequencies at different temperatures were determined, and the temperature dependence of all the mode frequencies are displayed in Figure 2.31. The temperature dependence of the high frequency mode is displayed in Figure 2.30. Other than the highest frequency mode and the lowest frequency phonon mode, both of them persisting throughout the whole 5-300 K range, there are five modes that are narrow enough to be fitted. Three of them appear at room temperature and disappear around 100 K. The other two only appear below 100 K. There is also a very broad feature between 500 cm^{-1} and 600 cm^{-1}.

The origin of these modes apparently cannot be assigned to lattice vibrations since Fe and Se atoms are too heavy to produce such high frequency phonon modes. They

cannot be assigned to magnon-related modes either. The reason is that there is no static magnetic ordering observed in this material [127]. The mode around 230 cm^{-1} has a line width of about 10 cm^{-1}, which is too narrow to be explained by any dynamic magnetic fluctuation. From 300 K to 5 K, the line widths of all the modes except the phonon mode show rather weak temperature dependence. This is also rather inconsistent with excitations of magnetic origin [128].

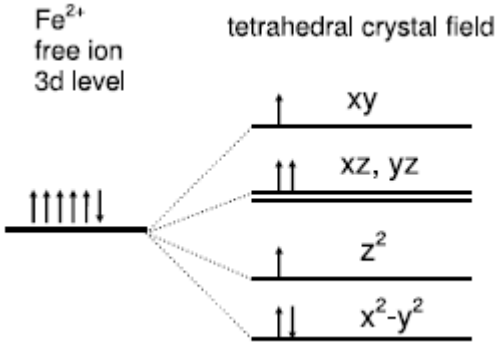

Figure 2.32 Schematics of the 3d electronic level splitting of Fe^{2+} ion in a tetrahedral crystal field.

These modes were assigned to excitations between the splitting 3d electronic levels of Fe^{2+} ions in a tetrahedral crystal field, as illustrated in the schematics of Figure 2.32. The reason is as follows. In transition metal compounds, the unfilled 3d level can be split due to the crystal field around the 3d ions. Since the Raman operator has even parity, the transitions between these split 3d levels are thus Raman active and can be quite strong.

This is in contrast to the rather weak infrared electronic lines due to the magnetic dipole interactions [128]. In the 1970s, Lockwood et al. studied the electronic and magnetic Raman scattering of transition metal halides extensively [128]. They found Raman excitations in $FeBr_2$ and $Fe_{1-x}Mn_xCl_2$ crystals between the range of 200 cm^{-1} and 700 cm^{-1} that were attributed to the Fe^{2+} crystal field splitting [129,130]. Theoretical calculations of the Fe^{2+} ion energy levels in a trigonal field were also carried out, and the overall splitting is about 700 cm^{-1}, consistent with experimental findings. In $FeSe_{1-x}$, the Fe ion is also 2+. The overall frequency range (200 to 700 cm^{-1}) and the weak temperature dependence of these excitations that have been observed are all very consistent with the crystal field excitations observed in the Raman spectra of $FeBr_2$ and $Fe_{1-x}Mn_xCl_2$ crystals [129,130]. These modes were thus assigned to the crystal field excitations of the Fe^{2+} ions in $FeSe_{1-x}$. A theoretical calculation of the crystal field splitting of Fe^{2+} ion in a tetrahedral field will be very helpful to confirm such assignments. Raman measurements on single crystal $FeSe_{1-x}$ in combination with such theoretical calculation can provide definitive assignments of these modes.

As mentioned above, there is discontinuity in the temperature dependence of these modes near 100 K, around which a high T tetragonal to low T monoclinic phase transition occurs in the polycrystalline samples [122]. Three modes appear at room temperature and disappear around 100 K. The other two only appear below 100 K. The most interesting one is the highest frequency mode, which can be seen in all temperatures. As shown in Fig. 2.30, it hardens with decreasing temperature, until about 100 K when it

softens. Around 25 K it hardens again, and there is no noticeable discontinuity across the 9 K superconducting transition. Crystal field splitting is expected to be rather sensitive to structural phase transitions since any small distance change between the ions changes the crystal field splitting immediately. Different phonons have different corresponding atomic movements, so some phonons can be rather insensitive to certain atomic movements. The insensitivity of the Raman phonons in the 1111 and 122 systems to the structural and superconducting phase transitions is well documented [123-125], and this is also consistent with what have been observed of the B_{1g} phonon in $FeSe_{1-x}$. The abrupt change around 100 K in the Raman active modes above 200 cm^{-1}, on the other hand, is consistent with crystal field excitations responding to structural phase transitions; thus, it provides additional support for the assignments. The hardening of the highest frequency mode at about 672 cm^{-1} below 25 K may indicate that local atomic movements reverse the trend set between 100 K and 25 K. At the moment, the itinerant or localized nature of the magnetic spins in Fe-based superconductors is still under debate and of great interest [131]. The crystal field splitting of Fe^{2+} is a rather important parameter to help settle this debate [132].

2.4 Conclusion

In summary, Raman spectra of polycrystalline $FeSe_{1-x}$ ($x \sim 0.03$) was measured from room temperature down to 5 K for the first time. One B_{1g} phonon mode has been observed around 185 cm^{-1}, and this mode hardens with decreasing temperature. This

phonon mode undergoes no noticeable change across both the structural phase transition and the superconducting transition, which is similar to the Raman phonon modes observed in the 1111 and 122 systems. In addition, several Raman excitations between 200 cm^{-1} and 700 cm^{-1} were also observed, and they were assigned as Fe^{2+} ions' crystal field excitations. These modes undergo abrupt change near the structural phase transition around 100 K, but do not exhibit much change across the superconducting transition. The exact magnitude of the crystal field splitting of Fe^{2+} is a rather important parameter, and it is estimated to be at about 670 cm^{-1}. Theoretical calculation of tetrahedral crystal field splitting of Fe^{2+} ions will help confirming this finding.

CHAPTER 3

MULTI-LAYER DIELECTRIC/METAL COMPOSITE FILM FOR CONTACT PHOTOLITHOGRAPHY SUB-WAVELENGTH FABRICATION

3.1 Introduction

3.1.1 Evanescent Wave

An evanescent wave is a near field standing wave with an intensity that exhibits exponential decay with distance from the boundary at which the wave was formed [133]. Evanescent waves are a general property of wave-equations, and can in principle occur in any context to which a wave-equation applies. They are formed at the boundary between two media with different wave motion properties, and are most intense within one-third of a wavelength from the surface of formation. In particular, evanescent waves can occur in the contexts of: optics and other forms of electromagnetic radiation, acoustics, quantum mechanics, and "waves on strings" [134, 135].

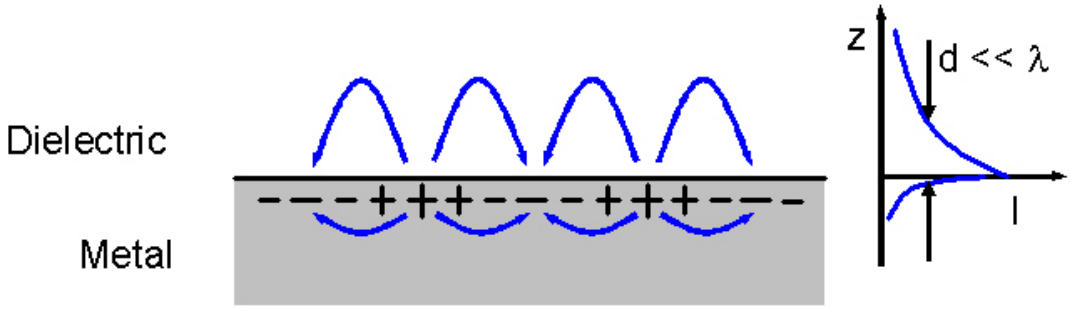

Figure 3.1 Schematic representation of evanescent waves propagating along a metal-dielectric interface.

Figure 3.1 shows the Schematic representation of evanescent waves propagating along a metal-dielectric interface. The charge density oscillations, when associated with

electromagnetic fields, are called surface plasmon-polariton waves. The exponential dependence of the electromagnetic field intensity on the distance away from the interface is shown on the right. These waves can be excited very efficiently with light in the visible range of the electromagnetic spectrum.

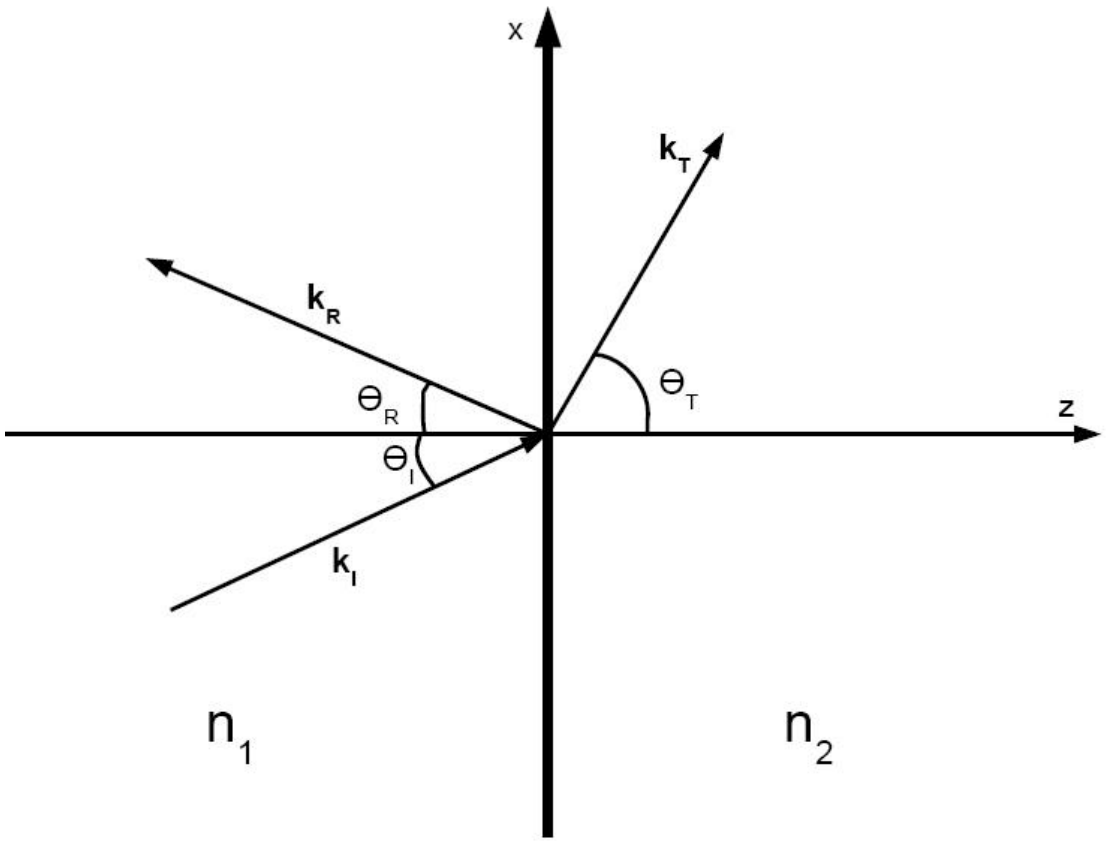

Figure 3.2 Configuration of a total internal reflection.

If a plane wave, confined to the xz plane, is incident on a dielectric with an angle θ_I and wave vector K_I then a transmitted ray will be created with a corresponding angle of transmittance as shown in Figure 3.2. The transmitted wave vector is given by:

$$K_T = k_T \sin(\theta_T)\vec{x} + k_T \cos(\theta_T)\vec{z} \tag{3.1}$$

If $n_1 > n_2$, then $\sin(\theta_T) > 1$ since the relationship $\sin(\theta_T) = \frac{n_1}{n_2}\sin(\theta_I)$ obtained from Snell's law. $\frac{n_1}{n_2}\sin(\theta_I)$ is greater than one while θ_I exceeds the critical angle. As a result of this $\cos(\theta_T)$ becomes complex:

$$\cos(\theta_T) = \sqrt{1-\sin^2(\theta_T)} = i\sqrt{\sin^2(\theta_T)-1} \tag{3.2}$$

The electric field of the transmitted plane wave is given by

$$E_T = E_0 e^{i(K_T \bullet r - \omega t)} \tag{3.3}$$

and so evaluating this further one obtains:

$$E_T = E_0 e^{i(K_T \bullet r - \omega t)} = E_0 e^{i(xk_T \sin(\theta_T) + zk_T \cos(\theta_T) - \omega t)} = E_0 e^{i\left(xk_T \sin(\theta_T) + zk_T i\sqrt{\sin^2(\theta_T)-1}\right)} \tag{3.4}$$

Using the fact that $k_T = \frac{\omega n_2}{c}$ and Snell's law one can finally obtain:

$$E_T = E_0 e^{-\alpha z} e^{i(kx-\omega t)} \tag{3.5}$$

Where $\alpha = \frac{\omega}{c}\sqrt{(n_1 \sin(\theta_I))^2 - n_2^2}$ and $k = \frac{\omega n_1}{c}\sin(\theta_I)$

This wave in the optically less dense medium is known as the evanescent wave. It's characterized by its propagation in the x direction and its exponential attenuation in the z direction. Another unique feature of evanescent waves is that on average no energy will be transmitted perpendicular to the face of the medium.

Evanescent waves could happen in optics and acoustics, the physical explanation for the existence of the evanescent wave is that the electric and magnetic fields (or

pressure gradients, in the case of acoustical waves) cannot be discontinuous at a boundary, as would be the case if there were no evanescent wave-field. In quantum mechanics, the physical explanation is exactly analogous—the Schrödinger wave-function representing particle motion normal to the boundary cannot be discontinuous at the boundary.

Electromagnetic evanescent waves have been used to exert optical radiation pressure on small particles in order to trap them for experimentation, or to cool them to very low temperatures, and to illuminate very small objects such as biological cells for microscopy (as in the total internal reflection fluorescence microscope). The evanescent wave from an optical fiber can be used in a gas sensor, and evanescent waves figure in the infrared spectroscopy technique known as attenuated total reflectance.

In electrical engineering, evanescent waves are found in the near field region within one-third wavelength of any radio antenna. During normal operation, an antenna emits electromagnetic fields into the surrounding near field region, and a portion of the field energy is re-absorbed, while the remainder is radiated as EM waves.

In quantum mechanics, the evanescent-wave solutions of the Schrödinger equation give rise to the phenomenon of wave-mechanical tunneling.

In microscopy, systems which capture the information contained in evanescent waves can be used to create super resolution images. Matter radiates both propagating and evanescent electromagnetic waves. Conventional optical systems capture only the information in the propagating waves and hence are subject to the diffraction limit. Systems which capture the information contained in evanescent waves, such as the

superlens and near field scanning optical microscopy, can overcome the diffraction limit; however these systems are then limited by the system's ability to accurately capture the evanescent waves [136]. The limitation on their resolution is given by

$$k \propto \frac{1}{d} \ln \frac{1}{\delta} \tag{3.6}$$

where k is the maximum wave vector that can be resolved, d is the distance between the object and the sensor, and δ is a measure of the quality of the sensor.

More generally, practical applications of evanescent waves can be classified in the following way. (1) Those in which the energy associated with the wave are used to excite some other phenomenon within the region of space where the original travelling wave becomes evanescent (for example, as in the total internal reflection fluorescence microscope). (2) Those in which the evanescent wave "couples" two media in which travelling waves are allowed, and hence permits the transfer of energy or a particle between the media (depending on the wave-equation in use), even though no travelling-wave solutions are allowed in the region of space between the two media. An example of this is so-called wave-mechanical tunneling. This second type of application is known generally as evanescent wave coupling.

Evanescent wave coupling is a process by which electromagnetic waves are transmitted from one medium to another by means of the evanescent, exponentially decaying electromagnetic field.

Coupling is usually accomplished by placing two or more electromagnetic elements such as optical waveguides close together so that the evanescent field generated

by one element does not decay much before it reaches the other element. With waveguides, if the receiving waveguide can support modes of the appropriate frequency, the evanescent field gives rise to propagating wave modes, thereby connecting (or coupling) the wave from one waveguide to the next.

Evanescent wave coupling is fundamentally identical to near field interaction in electromagnetic field theory. Depending on the impedance of the radiating source element, the evanescent wave is either predominantly electric (capacitive) or magnetic (inductive), unlike in the far field where these components of the wave eventually reach the ratio of the impedance of free space and the wave propagates radioactively. The evanescent wave coupling takes place in the non-radioactive field near each medium and as such is always associated with matter, i.e. with the induced currents and charges within a partially reflecting surface. This coupling is directly analogous to the coupling between the primary and secondary coils of a transformer, or between the two plates of a capacitor. Mathematically, the process is the same as that of quantum tunneling, except with electromagnetic waves instead of quantum-mechanical wave functions.

3.1.2 Hafnium (IV) Oxide

Hafnium (IV) oxide is the inorganic compound with the formula HfO_2 [137]. Also known as hafnia, this colorless solid is one of the most common and stable compounds of hafnium. It is an electrical insulator with a band gap of approximately 6 eV. Hafnium dioxide is an intermediate in some processes that give hafnium metal.

Hafnium (IV) oxide is quite inert. It reacts with strong acids such as concentrated sulfuric acid and with strong bases. It dissolves slowly in hydrofluoric acid to give fluorohafnate anions. At elevated temperatures, it reacts with chlorine in the presence of graphite or carbon tetrachloride to give hafnium tetrachloride.

Hafnia is used in optical coatings, and as a high-k dielectric in DRAM capacitors. Hafnium-based oxides are currently leading candidates to replace silicon oxide as a gate insulator in field effect transistors. The advantage for transistors is its high dielectric constant: The dielectric constant of HfO_2 is 25, while the dielectric constant of SiO_2 is only 3.9 [138].

The compound appears to have been chosen by both IBM and Intel as a substrate for future integrated circuits, where it may help in the continuing effort to increase logic density and clock speeds, or to lower power consumption, in computer processors.

Because of its very high melting point, hafnia is also used as a refractory material in the insulation of such devices as thermocouples, where it can operate at temperatures up to 2500 °C.

Hafnium Oxide is applied to carbon nanotube-based Non-Volatile RAM (NVRAM), where it replaces silicon dioxide as the insulating layer. This switch in material decreased the amount of time to access the memory from several milliseconds to just around 100 nanoseconds thereby potentially increasing the reading and writing to NVRAM by a factor of 100,000.

3.1.3 Evaporation Deposition

Evaporation deposition, sometimes called vacuum deposition (or vacuum evaporation) is a PVD process in which the atoms or molecules from a thermal vaporization source reach the substrate without collisions with residual gas molecules in the deposition chamber [139-141]. This type of PVD process requires a relatively good vacuum. Although sputtering and sputter deposition were reported in the mid-1800s using oil-sealed piston pumps, vacuum evaporation had to await the better vacuums provided by the Springer mercury-column vacuum pumps. In 1879, Edison used this type of pump to evacuate the first carbon-filament incandescent lamps and in 1887 Nahrwold performed the first vacuum evaporation. Vacuum deposition of metallic thin films was not common until the 1920s. Optically transparent vacuum-deposited antireflection (AR) coatings were patented by Macula (Zeus Optical) in 1935 [142]. The subject of early vacuum evaporation was reviewed by Glang in 1970 [143] and most review articles and book chapters on the subject since that time have drawn heavily on his work.

Vacuum deposition normally requires a vacuum of better than 10^{-4} Torr in order to have a long mean free path between collisions. At this pressure there is still a large amount of concurrent impingement on the substrate by potentially undesirable residual gases that can contaminate the film. If film contamination is a problem, a high (10^{-7} Torr) or ultrahigh (10^{-9} Torr) vacuum environment can be used to produce a film with the desired purity, depending on the deposition rate, reactivities of the residual gases and depositing species, and the tolerable impurity level in the deposit.

A material vaporizes freely from a surface when the vaporized material leaves the surface with no collisions above the surface. The free surface vaporization rate is proportional to the vapor pressure and is given by the Hertz–Knudsen vaporization equation:

$$dN/dt = C(2\pi mKT)^{-1/2}(p^* - p)\sec^{-1} \quad (3.7)$$

where

dN = number of evaporating atoms per cm^2 of surface area

C = constant that depends on the rotational degrees of freedom in the liquid and the vapor

p* = vapor pressure of the material at temperature

p = pressure of the vapor above the surface

k = Boltzmann's constant

T = absolute temperature

m = mass of the vaporized species

The maximum vaporization rate occurs when p = 0 and C = 1. In vacuum evaporation, the actual vaporization rate will be a third to a tenth of this maximum rate because of collisions in the vapor above the surface (i.e. $p > 0$ and $C \neq 1$), surface contamination, and other effects.

For low vaporization rates the flux distribution can be described by a cosine distribution (Figure 3.3). With no collisions in the gas phase, the material travels in a straight line between the source and the substrate (i.e. line-of-sight deposition). The

material from a point source deposits on a surface with a distance and substrate orientation dependence given by the cosine deposition distribution equation:

$$dm / dA = \left(E / \pi r^2\right)\cos\varphi\cos\theta \qquad (3.8)$$

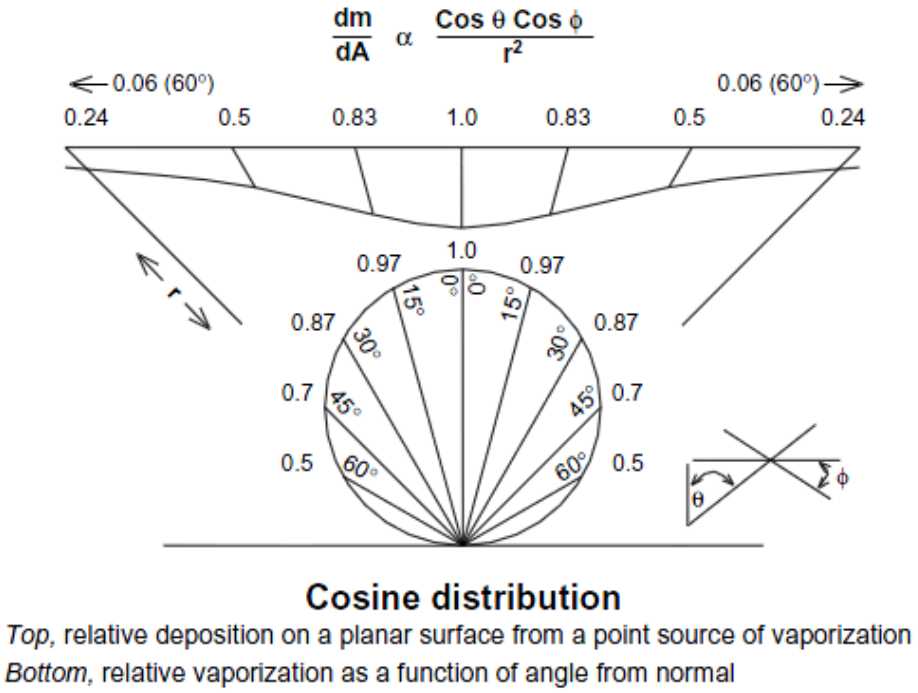

Figure 3.3 The Distribution of Atoms Vaporized from a Point Source and the Thickness Distribution of the Film Formed on a Planar Surface Above the Source.

Where:

dm/dA is the mass per unit area

E = the total mass evaporated

r = the distance from the source to the substrate

θ = the angle from the normal to the vaporizing surface

φ = the angle from a line from the source to a point on the substrate

At any point on the surface the angular distribution of the depositing flux is small since the flux originates from a point vaporization source. Generally, the total area of vaporization in thermal evaporation is small, giving a small angular distribution of the incident atomic flux on a point on the substrate. In actuality, the flux distribution from a free surface may not be cosine but can be modified by source geometry, collisions associated with a high vaporization rate, level of evaporant in the source, etc. In such cases, the flux distribution must be measured directly. A more complete model for the flux distribution from a Knudson (orifice) source is given by the Knudsen effusion model proposed by Ruth and Hirth [144]. Atoms leave a hot surface with thermal energies given by 3⁄2 kT where k is Boltzmann's constant and T is the absolute temperature. The atoms have a Maxwell–Boltzmann distribution in velocities. For example, for a 1500°C evaporation temperature of copper, the mean kinetic energy of the vaporized copper atoms is 0.2 eV and the mean atom velocity is about 1 km/sec.

Thermal vaporization requires that the surface and generally a large volume of material be heated to a temperature at which there is an appreciable vapor pressure. Common heating techniques for evaporation/sublimation include resistive heating, high energy e-beams, low energy e-beams, and inductive (rf) heating.

Focused high energy e-beams are necessary for the evaporation of refractory materials such as most ceramics, glasses, carbon, and refractory metals. This e-beam ("e-beam") heating is also useful for evaporating large quantities of materials. When vaporizing solid surfaces of electrically insulating materials, local surface charge buildup

can occur on the source surface, leading to surface arcing, which can produce particulate contamination in the deposition system.

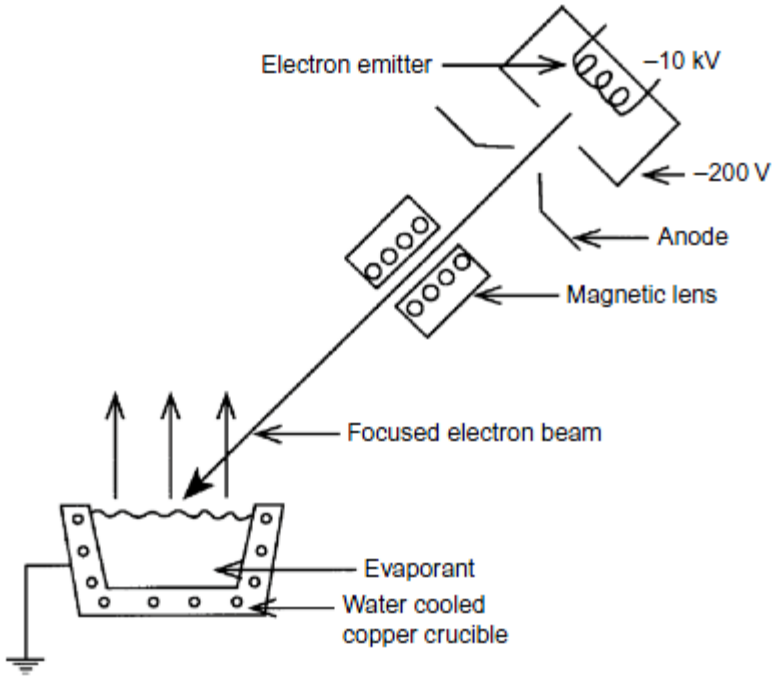

Figure 3.4 Focused Linear Electron Beam (e-beam) Vaporization Sources.

Electron beam deposition of dielectric materials can generate insulating surfaces that can build up a charge that causes arcing and particulate formation in the deposition system. With the e-beam evaporation of some materials, such as beryllium, significant numbers of ions are produced and they can be accelerated to the substrate, causing self-sputtering, and be used to modify the film microstructure [145]. The high energy electron bombardment of the source material can produce soft X-rays, which can be detrimental to sensitive semiconductor devices.

The long-focus gun uses electron optics to focus the e-beam on a surface, which can be an appreciable distance from the electron emitter. The optic axis is often a straight line from the emitter to the evaporant and therefore the gun must be mounted off-axis from the source–substrate axis.

Unfocused high energy e-beam heating can be accomplished with an electron source by applying a voltage between the electron emitter and the source material or source container, which is usually at ground potential. Such a source is referred to as a work-accelerated gun. High current, low energy e-beam (anodic arc vaporization) sources may be produced by thermoelectron-emitting surfaces such as hollow cathodes [146, 147]. The electrons can be accelerated to several hundred volts and magnetically deflected onto the source, which is at ground potential. Low energy e-beams are typically not very well focused but can have high current densities. The vaporization of a surface by the low energy e-beam can provide appreciable ionization of the vaporized material since the vaporized atoms pass through a high density low energy electron cloud as they leave the surface. These “film ions” can be used in ion plating. Magnetic confinement of the electrons along the emitter–source axis can also be used to increase the electron path length so as to increase the ionization probability.

Vacuum deposition has advantages and disadvantages compared to other PVD techniques.

Advantages in some cases:

* Line-of-sight deposition allows the use of masks to define areas of deposition.

* Large-area sources can be used for some materials (e.g. “hog trough” crucibles for Al and Zn, multiple sources

* High deposition rates can be obtained.

* Deposition rate monitoring is relatively easy.

* Vaporization source material can be in many forms, such as chunks, powder, wire, chips, etc.

* Vaporization source material of high purity is relatively inexpensive.

* High purity films are easily deposited from high purity source material since the deposition ambient can be made as non-contaminating as is desired.

* The technique is relatively inexpensive compared to other PVD techniques. Disadvantages in some cases:

* Line-of-sight deposition gives poor surface coverage – elaborate tooling and fixturing is needed.

* Line-of-sight deposition provides poor deposit uniformity over a large surface area without complex fixturing and tooling.

* Poor ability to deposit many alloys and compounds.

* High radiant heat loads during processing.

* Poor utilization of vaporized material.

* Non-optimal film properties – e.g. pinholes, less than bulk density, columnar morphology, high residual film stress.

* Few processing variables available for film property control.

Vacuum deposition is the most widely used of the PVD deposition processes. Applications of vacuum deposition include:

* Electrically conductive coatings – ceramic metallization (e.g. Ti–Au, Ti–Pd–Au, Al, Al–Cu–Si, Cr–Au, Ti–Ag), semiconductor metallization (e.g. Al : Cu (2%) on silicon), metallization of capacitor foils (e.g. Zn, Al).

* Optical coatings – reflective and AR multilayer coatings, heat mirrors, abrasion resistant topcoats.

* Decorative coatings (e.g. Al, Au on plastics).

* Moisture and oxygen permeation barriers – packaging materials (e.g. Al and $SiO_{1.8}$ on polymer webs).

* Corrosion-resistant coatings (e.g. Al on steel).

* Insulating layers for microelectronics.

* Selenium coatings for electrography or xerography.

* Avoidance of many of the pollution problems associated with electroplating (“dry processing”).

* Fabrication of free-standing structures.

* Vacuum plating of high strength steels to avoid the hydrogen embrittlement associated with electroplating (e.g. Cd on steel – “vacuum cad plating”).

Vacuum deposition is the most energy-efficient of the PVD processes. Where the substrate coverage, adhesion, process throughput, and film properties are acceptable, it is generally the PVD process of choice.

3.1.4 Chemical Mechanical Polishing

Chemical Mechanical Polishing/Planarization is a process of smoothing surfaces with the combination of chemical and mechanical forces [148], it can be thought of as a hybrid of chemical etching and free abrasive polishing.

The process uses abrasive and corrosive chemical slurry (commonly a colloid) in conjunction with a polishing pad and retaining ring, typically of a greater diameter than the wafer. The pad and wafer are pressed together by a dynamic polishing head and held in place by a plastic retaining ring. The dynamic polishing head is rotated with different axes of rotation (i.e., not concentric). This removes material and tends to even out any irregular topography, making the wafer flat or planar. This may be necessary in order to set up the wafer for the formation of additional circuit elements. For example, this might be necessary in order to bring the entire surface within the depth of field of a photolithography system, or to selectively remove material based on its position. Typical depth-of-field requirements are down to Angstrom levels for the latest 65 nm technology.

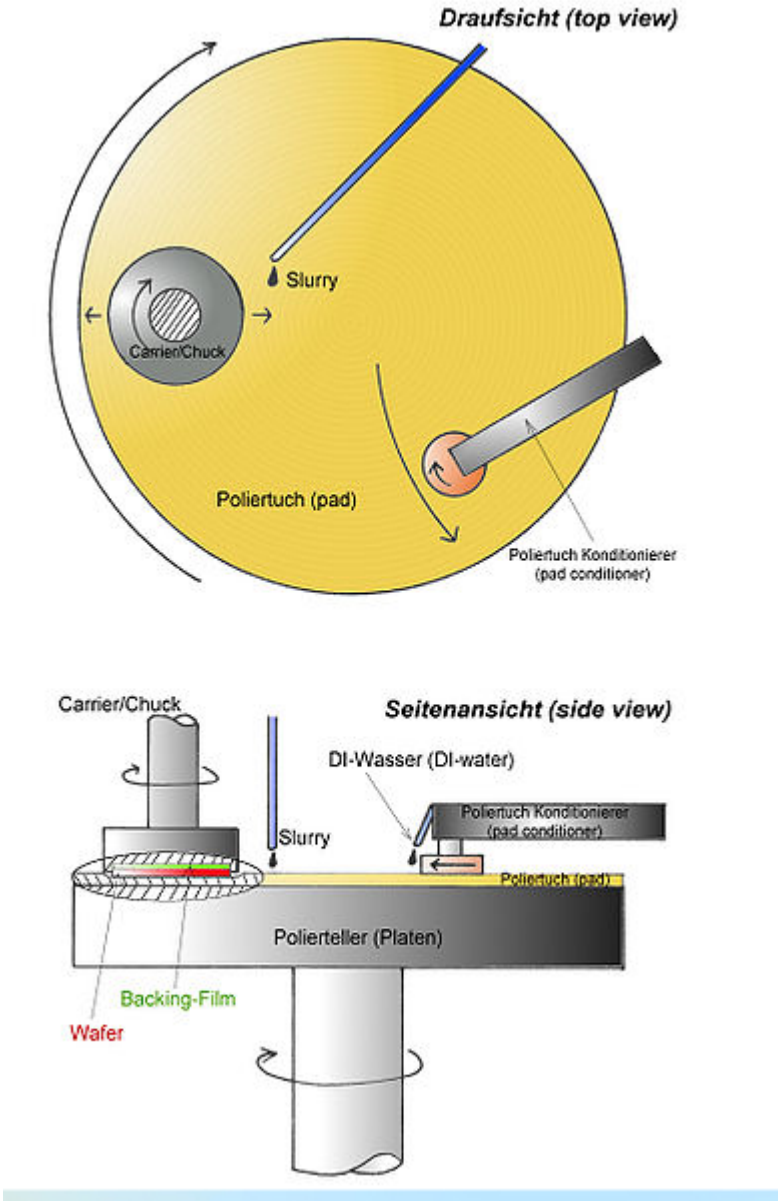

Figure 3.5 Functional principle of Chemical Mechanical Polishing.

Typical CMP tools, such as the ones seen on the next page (Figures 3.5) consist of a rotating and extremely flat platen which is covered by a pad. The wafer that is being polished is mounted upside-down in a carrier/spindle on a backing film. The retaining ring keeps the wafer in the correct horizontal position. During the process of loading and

unloading the wafer onto the tool, the wafer is held by vacuum by the carrier to prevent unwanted particles from building up on the wafer surface. A slurry introduction mechanism deposits the slurry on the pad; this is represented by the slurry supply in Figures 3.5. Both the platen and the carrier are then rotated and the carrier is kept oscillating as well; this can be better seen in the top view of Figures 3.5. A downward pressure/down force is applied to the carrier, pushing it against the pad; typically the down force is an average force, but local pressure is needed for the removal mechanisms. Down force depends on the contact area which, in turn, is dependent on the structures of both the wafer and the pad. Typically the pads have a roughness of 50 μm; contact is made by asperities (which typically are the high points on the wafer) and, as a result, the contact area is only a fraction of the wafer area. In CMP, the mechanical properties of the wafer itself must be considered too. If the wafer has a slightly bowed structure, the pressure will be greater on the edges than it would on the center, which causes non-uniform polishing. In order to compensate for the wafer bow, pressure can be applied to the wafer's backside which, in turn, will equalize the centre-edge differences. The pads used in the CMP tool should be rigid in order to uniformly polish the wafer surface. However, these rigid pads must be kept in alignment with the wafer at all times. Therefore, real pads are often just stacks of soft and hard materials that conform to wafer topography to some extent. Generally, these pads are made from porous polymeric materials with a pore size between 30-50 μm, are consumed in the process, and must be regularly reconditioned. In most cases the pads are very much proprietary, and are

usually referred to by their trademark names rather than their chemical or other properties.

Before about 1990 CMP was looked on as too "dirty" to be included in high-precision fabrication processes, since abrasion tends to create particles and the abrasives themselves are not without impurities. Since that time, the integrated circuit industry has moved from aluminum to copper conductors. This required the development of an additive patterning process, which relies on the unique abilities of CMP to remove material in a planar and uniform fashion and to stop repeatably at the interface between copper and oxide insulating layers. Adoption of this process has made CMP processing much more widespread. In addition to aluminum and copper, CMP processes have been developed for polishing tungsten, silicon dioxide, and (recently) carbon nanotubes.

Nowadays, several limitations of CMP appear during the polishing process. A new technology needs to be optimized. Consequently, this process is immaturity requiring an increase of wafer metrology to attain the desired results. In addition, it was discovered that CMP process has several potential defects, such as, stress cracking, delaminating at weak interfaces, and corrosive attacks from slurry chemicals. The oxide polishing process, which is the oldest and most used in today’s industry, has one problem: a lack of end points creates blind spot polishing, making it hard to determine when the desired amount of material has been removed or the desired degree of planarization has been obtained. If the oxide layer has not been sufficiently thinned and/or the desired degree of planarity has not been obtained during this process, then the wafer must be

repolished. If the oxide thickness is too thin or too non-uniform, then the wafer must be reworked. Obviously, this method is time-consuming and costly since technicians have to be more attentive while performing this process.

Shallow trench isolation, a process used to fabricate semiconductor devices, is a technique used to enhance the isolation between devices and active areas. Moreover, STI has a higher degree of planarity making it essential in photolithographic applications, depth of focus budget by decreasing minimum line width. To planarize shallow trenches, a common method should be used such as the combination of resist etching-back (REB) and chemical mechanical polishing (CMP). This process comes in a sequence pattern as follows. First, the isolation trench pattern is transferred to the silicon wafer. Oxide is deposited on the wafer in the shape of trenches. A photo mask, composed of silicon nitrate, is patterned on the top of this sacrificial oxide. A second layer is added to the wafer to create a planar surface. After that, the silicon is thermally oxidized, so the oxide grows in regions where there is no SiN_4 and the growth is between 0.5 and 1.0 μm thick. Since the oxidizing species such as water or oxygen are unable to diffuse through the mask, the nitride prevents the oxidation. Next, the etching process is used to etch the wafer and leave a small amount of oxide in the active areas. In the end, CMP is used to polish the SiO_2 overburden with an oxide on the active area.

3.1.5 Sub-wavelength Imaging

Optical imaging is usually subject to fundamental diffraction limit: whenever an object is imaged by an optical system, such as the lens of a camera, fine features, i.e., those smaller than half the wavelength of the light, are permanently lost in the image. The loss of information arises because light emerging from the object's fine features carries components with high spatial frequency, i.e., evanescent waves that exponentially decay, resulting in an imperfect image. The lost subwavelength details are the fundamental reason for Abbe's diffraction limit, which determines the smallest features that one can see through even the best of lenses. Practically speaking, this limits the resolution of all photolithography systems, which are the basis of modern electronics industry.

To beat the diffraction limit, one has to get access to the evanescent light which carries the subwavelength information. One way to get around this problem is to utilize the so called negative refractive index material (NIM) [149]. If a lens made of NIM is placed close to an object, the near-field evanescent waves can be strongly enhanced across the lens [150]. Such intriguing behavior relies on the fact that the NIM supports resonant surface waves, one example of which is surface plasmon polaritons. Evanescent waves can be efficiently coupled into surface modes and enhanced by their resonant nature when their wave vectors are matched. Resonance-based negative-refractive-index media constructed from realistic materials, however, are inherently associated with substantial energy dissipation or loss (that is, the imaginary part of ε and μ), which hinders the resolution of the 'perfect image'. Another consequence of the material loss

and imperfections is that the distance between the slab and both the object and its image, as well as the slab's thickness, must all be small compared with the wavelength if we are to obtain meaningful resonant enhancement of the evanescent waves [151]. When their scale is deeply subwavelength, the electrostatic limit can be applied. In this case, the electric and magnetic responses of a material decouple, and only one material property (ε or μ) needs to be negative to support resonant surface waves for one specific polarization (transverse magnetic, TM, or transverse electric, TE mode). In this special case, the subwavelength imaging effect therefore remains valid in a single negative index medium for one polarization of light. As a natural candidate having negative ε at optical frequencies, a slab of silver (because of low loss in metal) was suggested for achieving the superlens effect for TM waves in optics [150].

Soon after Pendry's theoretical proposal, experimental attempts to test this concept began. In 2005, the optical superlensing effect was observed using a thin slab of silver, a single negative-ε material, which could effectively image 60-nm features ($\lambda/6$), well below the diffraction limit [152]. The sub-diffraction-limited image was recorded by optical lithography at 365 nm wavelength. The presence of the silver superlens improved the image resolution remarkably in the near field by excitation of surface plasmons. Using a similar scheme, another group also confirmed the superlensing effect in silver films [153]. These experimental realizations of the optical subwavelength imaging effect clearly showed the potential for imaging and lithography below the diffraction limit, yet there are some fundamental obstacles for practical photolithography application.

Fabricating ultra-flat surfaces on either side of the superlens remains extremely challenging, with surfaces roughness being detrimental to the surface resonances and enhancement. Optical loss on the silver thin film surface remains large, and dependence on the intrinsic optical properties of silver means the applicable light spectral range is quite narrow.

At the same time when NIM properties become very topical, another line of research showed some remarkable effect when metal and dielectric materials are thrown together. Bloemer et al. found that by stacking metal/dielectrics layers alternatively into a periodic multilayer structure, or the so called 1D photonic crystal structure, even though the thickness of the metal layer can add up to more than 100 times of metal skin depths, the total transmission through the multilayer structure can be above 50% [154]. This is truly remarkable, considering light decays exponentially inside metal, and after several skin depths light intensity usually is considered negligible.

In this work, the subwavelength imaging capability of the metal layer is combined with the remarkable large transmission of the 1d periodic metal/insulator photonic crystal structure to design a novel multilayer metal/dielectric composite thin film. After these structures were fabricated, the transmission and sub-wavelength capability of the design were confirmed by the experimental results. A novel photo-mask fabrication process around this thin film structure was then developed. This makes it possible to fabricate sub-100 nm structure using conventional contact mask aligner with the H or I-line of mercury lamp.

3.2 Experimental Methods

HfO_2 was used as the dielectric and silver as the metal, taking advantage of the relative uniform and high refractive index of HfO_2 (about 2 from UV to IR). Table 3.1 is the thickness of this multilayer structure while Figure 3.6 shows its schematics. A 4-pocket rotating-turret Temescal e-beam evaporator was used to deposit this metal/insulator composite structure on glass substrate (Figure 3.6). Figure 3.7a shows the simulated transmittance while Figure 3.7b shows the measured transmittance. They agree with each other within about 10%, which is rather impressive considering all the imperfection of layer thickness in real experiments. Several series across the glass substrate were measured, and the transmittance is quite uniform. This film is designed so that it has high transmittance of above 50% between 320 nm to 470 nm, exactly the spectral range where the mercury lamp of conventional photolithography works. Considering the optical skin depth of silver is about 13 nm, and here the total silver thickness is 88 nm, a transmittance above 50% is truly remarkable, thanks to the resonant tunneling effect, where light intensity is mostly concentrated in the dielectric layers.

Table 3.1 Thickness of each layer

Layer #	Substrate	Layer 1	Layer 2	Layer 3	Layer 4	Layer 5	Layer 6	Layer 7
Material	Glass Slide	HfO2	Silver	HfO2	Silver	HfO2	Silver	HfO2
Thickness (nm)		22.5	22	45	22	45	22	45
		Layer 8	Layer 9					
		Silver	HfO2					
		22	22.5					

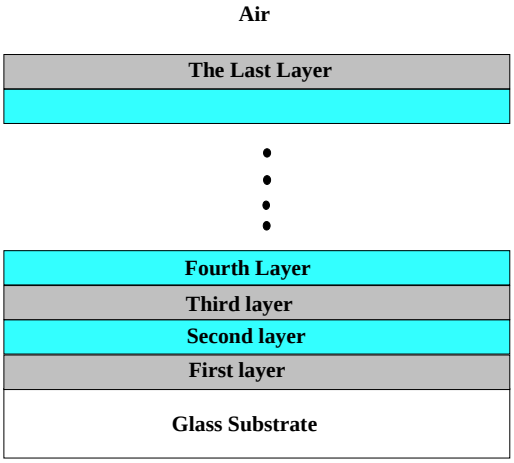

Figure 3.6 Schematic of the metal/dielectric multilayer.

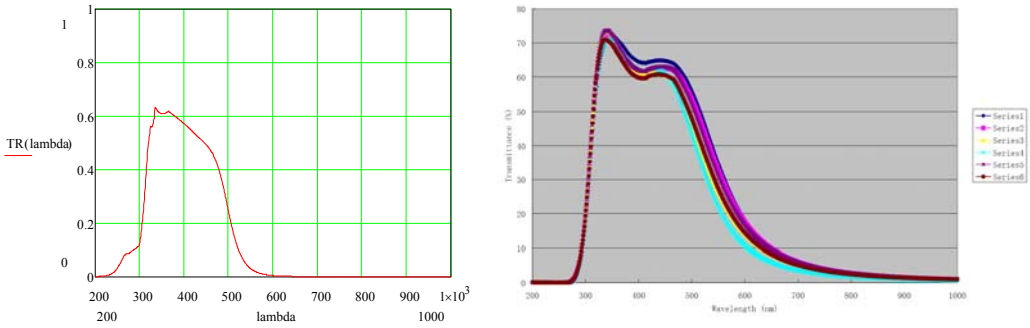

(a) (b)

Figure 3.7 (a) Transmittance by simulation (b) Transmittance measured.

Figure 3.8 shows the schematics of the processing steps we developed to fabricate the photomask with subwavelength photolithography capability. As noted above, with the designed multilayer structure, the optical loss problem has been solved. The other big obstacle is surface roughness. To meet this challenge a step called chemical-mechanical polish (CMP) was used. After using e-beam to write features as small as 45 nm on SiO_2 layer, chromium was deposited on the SiO_2 layer, and use CMP to polish the surface

roughness. In the end a surface roughness below 3 nm across a 4 mm diameter structure was achieved, therefore effectively solved this problem.

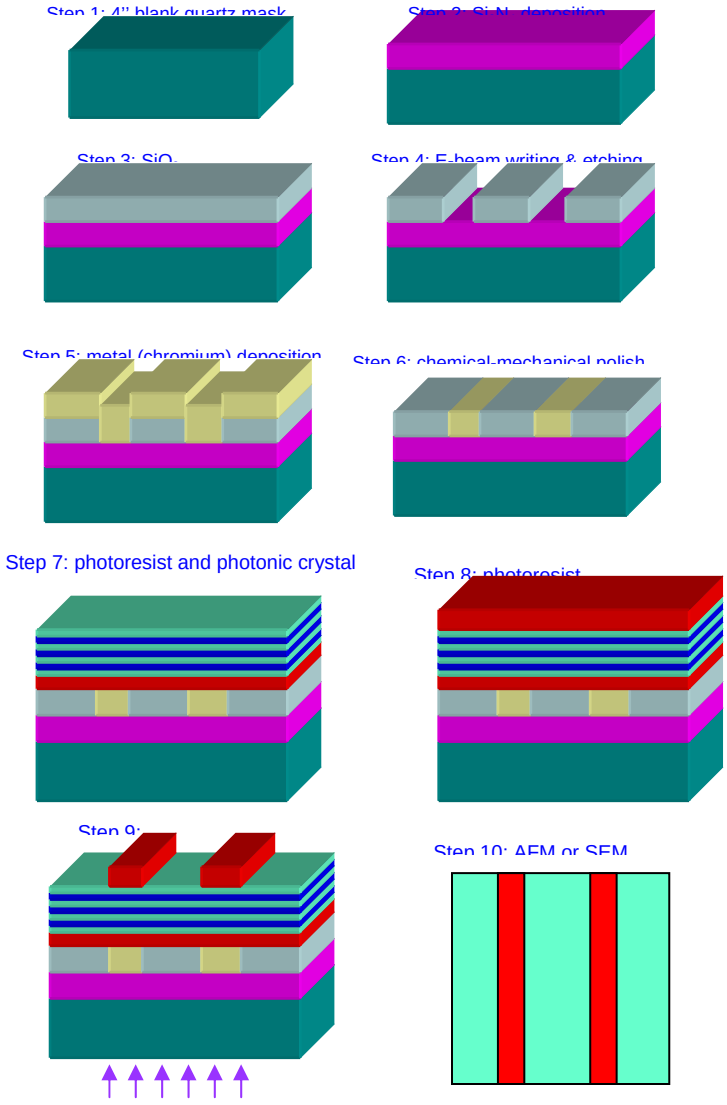

Figure 3.8 Schematics of the photo-mask processing steps.

3.3 Result and Discussion

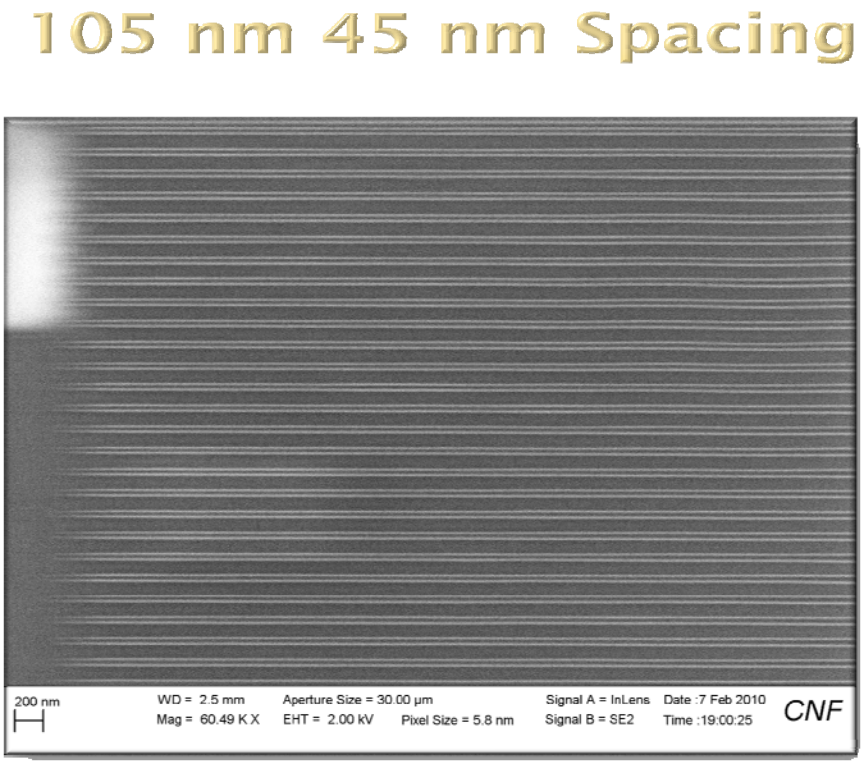

Figure 3.9 SEM image of the developed photoresist layer.

Figure 3.9 shows the SEM image of a photoresist layer, developed with the photomask shown in Figure 3.8 with the multilayer deposition illustrated in Figure 3.6. A conventional MA-6 Karl-Zeiss contact mask aligner with the mercury lamp H-line with a wavelength of 405 nm was used. The smallest feature achieved is about 45 nm, as shown in Figure 3.9. Thus, not only subwavelength photolithography was achieved, more importantly, a very practical way of fabricating sub-100 nm structures using the conventional contact aligner has been developed. The only thing different from

conventional photolithography is the photomask, which can be fabricated separately and without too many special arrangements.

3.4 Conclusion

Not only subwavelength photolithography was achieved, more importantly, a very practical way of fabricating sub-100 nm structures using the conventional contact aligner has been developed, further applications of this research could be expected.

REFERENCES

[1] *Transition metal*. Retrieved October 20, 2010, from http://en.wikipedia.org/wiki/Transition_metal

[2] J. M. D. Coey, M. Viret, S. von Molnar. (1999). Mixed-valence manganites. *Advances in Physics*, 48, 167-293.

[3] Masatoshi Imada, Atsushi Fujimori, Yoshinori Tokura. (1998). Metal-insulator transitions. *Reviews of Modern Physics*, 70, 1039-1263.

[4] *Giant magnetoresistance*. Retrieved October 20, 2010, from http://en.wikipedia.org/wiki/Giant_magnetoresistance

[5] A P Ramirez. (1997). Colossal magnetoresistance. *Journal of Physics: Condensed Matter*, 9, 8171–8199.

[6] C. Zener. (1951). Interaction Between the d Shells in the Transition Metals. *Physical Review*, 81, 440-444.

[7] P. W. Anderson, H. Hasegawa. (1955). Considerations on Double Exchange. *Physical Review*, 100, 675-681.

[8] P. G. de Gennes. (1960). Effects of Double Exchange in Magnetic Crystals. *Physical Review*, 118, 141-154.

[9] A. J. Millis, P. B. Littlewood, and B. I. Shraiman. (1995). Double Exchange Alone Does Not Explain the Resistivity of $La_{1-x}Sr_xMnO_3$. *Physical Review Letters*, 74, 5144-5147.

[10] Y. Tomioka1, A. Asamitsu1, Y. Moritomo1, H. Kuwahara1, and Y. Tokura. (1995). Collapse of a Charge-Ordered State under a Magnetic Field in $Pr_{1/2}Sr_{1/2}MnO_3$. *Physical Review Letters*, 74, 5108-5111.

[11] E. O. Wollan and W. C. Koehler. (1955). Neutron Diffraction Study of the Magnetic Properties of the Series of Perovskite-Type Compounds [(1-x)La, xCa]MnO_3. *Physical Review*, 100, 545-563.

[12] A. P. Ramirez, P. Schiffer, S-W. Cheong, C. H. Chen, W. Bao, T. T. M. Palstra, P. L. Gammel, D. J. Bishop, and B. Zegarski. (1996). Thermodynamic and Electron Diffraction Signatures of Charge and Spin Ordering in $La_{1-x}Ca_xMnO_3$. *Physical Review Letters*, 76, 3188-3196.

[13] A. J. Millis, Boris I. Shraiman, and R. Mueller. (1996). Dynamic Jahn-Teller Effect and Colossal Magnetoresistance in $La_{1-x}Sr_xMnO_3$. *Physical Review Letters*, 77, 175-178.

[14] H. Röder, Jun Zang, and A. R. Bishop. (1996). Lattice Effects in the Colossal-Magnetoresistance Manganites. *Physical Review Letters*, 76, 1356-1359.

[15] Guo-meng Zhao, K. Conder, H. Keller, K. A. Müller. (1996). Giant oxygen isotope shift in the magnetoresistive perovskite $La_{1-x}Ca_xMnO_{3+y}$. *Nature*, 381, 676-678

[16] Dai P, Zhang J, Mook H A, Liou S-H, Dowben P A and Plummer E W. Experimental evidence for the dynamic Jahn-Teller effect in $La_{0.65}Ca_{0.35}MnO_3$. *Physical Review B*, 54, R3694–R3697.

[17] J R Fletcher and K W H Stevens. (1969). The Jahn-Teller effect of octahedrally co-ordinated $3d^4$ ions. *Journal of Physics C: Solid State Physics*, 2, 444-456.

[18] Y. Shimakawa, Y. Kubo, T. Manako. (1996). Giant magnetoresistance in $Ti_2Mn_2O_7$ with the pyrochlore structure. *Nature* 379, 53-55.

[19] Elbio DAGOTTO, Takashi HOTTA, Adriana MOREO. (2001). COLOSSAL MAGNETORESISTANT MATERIALS: THE KEY ROLE OF PHASE SEPARATION. *Physics Reports*, 344, 1-153.

[20] Junjiro Kanamori. (1959). Superexchange interaction and symmetry properties of electron orbitals. *Journal of Physics and Chemistry of Solids*, 10, 87-98.

[21] M. Uehara, S. Mori, C. H. Chen, S.-W. Cheong. (1999). Percolative phase separation underlies colossal magnetoresistance in mixed-valentmanganites. *Nature*, 399, 560-563.

[22] Jin, S.,Tiefel, T. H. (1994). Thousandfold change in resistivity in magnetoresistive La-Ca-Mn-O films. *Science*, 264, 413-414.

[23] S-W. Cheong and C. H. Chen. (1998). *Colossal Magnetoresistance, Charge Ordering and Related Properties of Manganese Oxides.* World Scientific, London. (pp.241-278).

[24] Allodi, G., Renzi, R. D., Guidi, G., Licci, F., and Pieper, M. W. (1997). Electronic phase separation in lanthanum manganites: Evidence from ^{55}Mn NMR. *Physical Review B*, 56, 6036-6046.

[25] Jacqueline B. A. A. ElemansB. Van Laar, K. R. Van Der Veen and B. O. Loopstra. (1971). The crystallographic and magnetic structures of $La_{1-x}Ba_xMn_{1-x}Me_xO_3$ (Me = Mn or Ti). *Journal of Solid State Chemistry*, 3, 238-242.

[26] M. Hennion, F. Moussa1, G. Biotteau, J. Rodríguez-Carvajal, L. Pinsard, and A. Revcolevschi. (1998). Liquidlike Spatial Distribution of Magnetic Droplets Revealed by Neutron Scattering in $La_{1-x}Ca_xMnO_3$. *Physical Review Letters*, 81, 1957-1960.

[27] P. G. Radaelli, D. E. Cox, M. Marezio, S -W. Cheong, P. E. Schiffer, and A. P. Ramirez. (1995). Simultaneous Structural, Magnetic, and Electronic Transitions in $La_{1-x}Ca_xMnO_3$ with x=0.25 and 0.50. *Physical Review Letters*, 75, 4488-4491.

[28] C. H. Chen and S-W. Cheong. (1996). Commensurate to Incommensurate Charge Ordering and Its Real-Space Images in $La_{0.5}Ca_{0.5}MnO_3$. *Physical Review Letters*, 76, 4042-4045.

[29] John B. Goodenough. (1955). Theory of the Role of Covalence in the Perovskite-Type Manganites [La, M(II)]MnO_3. *Physical Review*, 100, 564-573.

[30] D. I. Khomskii and G. A. Sawatzky. (1997). Interplay between spin, charge and orbital degrees of freedom in magnetic oxides. *Solid State Communications*, 102, 87-99.

[31] A. J. Millis. (1997). Orbital ordering and superexchange in manganite oxides. *Physical Review B*, 55, 6405-6408.

[32] Knizek, K., Jirak, Z., Pollert, E., and Zounova, F. (1992). Structure and magnetic properties of $Pr_{1-x}Sr_xMnO_3$ perovskites. *Journal of Solid State Chemistry*, 100, 292-300.

[33] Y. Tomioka, A. Asamitsu, H. Kuwahara, Y. Moritomo, Y. Tokura. (1996). Magnetic-field-induced metal-insulator phenomena in $Pr_{1-x}Ca_xMnO_3$ with controlled charge-ordering instability. *Physical Review B*, 53, R1689-R1692.

[34] Yoshizawa, H., Kajimoto, R., Kawano, H., Toimioka, T., and Tokura, Y. (1997). Bandwidth-control-induced insulator-metal transition in $Pr_{0.65}(Ca_{1-y}Sr_y)_{0.35}MnO_3$ and $Pr_{0.7}Ca_{0.3}MnO_3$. *Physical Review B*, 55, 2729-2732.

[35] Jirak, Z., Krupicka, S., Simsa, Z., Dlouha, M., and Vratislav, S. (1985). Neutron diffraction study of $Pr_{1-x}Ca_xMnO_3$ perovskites. *Journal of Magnetism and Magnetic Materials*, 53, 153-166.

[36] Takayoshi Takeda, Yasuo Yamaguchi, Hiroshi Watanabe. (1972). Magnetic Structure of $SrFeO_3$. *Journal of the Physical Society of Japan*, 33, 967-969.

[37] P. A. Sharma, Sung Baek Kim, T. Y. Koo, S. Guha, and S-W. Cheong. (2005). Reentrant charge ordering transition in the manganites as experimental evidence for a strain glass. *Physical Review B*, 71, 224416.

[38] *Superconductivity*, Retrieved October 20, 2010, from http://en.wikipedia.org/wiki/Superconductivity

[39] Jun Nagamatsu, Norimasa Nakagawa, Takahiro Muranaka, Yuji Zenitani and Jun Akimitsu. (2001). Superconductivity at 39 K in magnesium diboride. *Nature*, 410, 63-64.

[40] Johnston, Hamish. (2009). *Type-1.5 superconductor shows its stripes*. Retrieved October 20, 2010, from http://physicsworld.com/cws/article/news/37806

[41] R. L. Dolecek. (1954). Adiabatic Magnetization of a Superconducting Sphere. *Physical Review*, 96, 25-28.

[42] H. Kleinert. (1982). Disorder version of the Abelian Higgs model and the order of the superconductive phase transition. *Lettere Al Nuovo Cimento*, 35, 405-412.

[43] J. Hove, S. Mo, and A. Sudbø. (2002). Vortex interactions and thermally induced crossover from type-I to type-II superconductivity. *Physical Review B*, 66, 064524.

[44] Landau, L. D (1984). *Electrodynamics of Continuous Media: Volume 8 (Course of Theoretical Physics)*. Oxford: Butterworth-Heinemann.

[45] David J. E. Callaway. (1990). On the remarkable structure of the superconducting intermediate state. *Nuclear Physics B*, 344, 627-645.

[46] *Josephson effect*. Retrieved October 20, 2010, from http://en.wikipedia.org/wiki/Josephson_effect

[47] *Type-I superconductor*. Retrieved October 20, 2010, from http://en.wikipedia.org/wiki/Type_I_superconductor

[48] *Type-II superconductor*. Retrieved October 20, 2010, from http://en.wikipedia.org/wiki/Type_II_superconductor

[49] *Conventional superconductor*. Retrieved October 20, 2010, from http://en.wikipedia.org/wiki/Conventional_superconductor

[50] *Unconventional superconductor*. Retrieved October 20, 2010, from http://en.wikipedia.org/wiki/Unconventional_superconductor

[51] F. Steglich, J. Aarts, C. D. Bredl, W. Lieke, D. Meschede, W. Franz, H. Schäfer. (1979). Superconductivity in the Presence of Strong Pauli Paramagnetism: $CeCu_2Si_2$. *Physical Review Letters*, 43, 1892-1896.

[52] H. R. Ott, H. Rudigier, Z. Fisk, J. L. Smith. (1983). UBe_{13}: An Unconventional Actinide Superconductor. *Physical Review Letters*, 50, 1595-1598.

[53] G. R. Stewart, Z. Fisk, J. O. Willis, J. L. Smith. (1984). Possibility of Coexistence of Bulk Superconductivity and Spin Fluctuations in UPt_3. *Physical Review Letters*, 52, 679-682.

[54] T. T. M. Palstra, A. A. Menovsky, J. van den Berg, A. J. Dirkmaat, P. H. Kes, G. J. Nieuwenhuys, J. A. Mydosh. (1985). Superconducting and Magnetic Transitions in the Heavy-Fermion System URu_2Si_2. *Physical Review Letters*, 55, 2727-2730.

[55] D. J. Bishop, C. M. Varma, B. Batlogg, E. Bucher, Z. Fisk, J. L. Smith. (1984). Ultrasonic Attenuation in UPt_3. *Physical Review Letters*, 53, 1009-1011.

[56] D. Jérome, A. Mazaud, M. Ribault, K. Bechgaard. (1980). Superconductivity in a synthetic organic conductor $(TMTSF)_2PF_6$. *Journal de Physique Lettres*, 41, 95-98.

[57] Bechgaard, Klaus; Carneiro, Claus S.; Olsen, Malte; Rasmussen, Finn; Jacobsen, Claus. (1981). Zero-Pressure Organic Superconductor: Di-(Tetramethyltetraselenafulvalenium)-Perchlorate $[(TMTSF)_2ClO_4]$. *Physical Review Letters*, 46, 852-855.

[58] Hiroki Takahashi, Kazumi Igawa, Kazunobu Arii, Yoichi Kamihara, Masahiro Hirano, Hideo Hosono. (2008). Superconductivity at 43 K in an iron-based layered compound $LaO_{1-x}F_xFeAs$. *Nature*, 453, 376-378.

[59] Charles Q. Choi. (2008). *Iron Exposed as High-Temperature Superconductor.* Retrieved October 20, 2010, from http://www.scientificamerican.com/article.cfm?id=iron-exposed-as-high-temp-superconductor

[60] X. H. Chen, T. Wu, G. Wu, R. H. Liu, H. Chen, D. F. Fang. (2008). *Superconductivity at 43 K in Samarium-arsenide Oxides* $SmFeAsO_{1-x}F_x$. Retrieved October 20, 2010, from http://arxiv.org/PS_cache/arxiv/pdf/0803/0803.3603v2.pdf

[61] F. Hunte, J. Jaroszynski, A. Gurevich, D. C. Larbalestier, R. Jin, A. S. Sefat, M. A. McGuire, B. C. Sales, D. K. Christen, D. Mandrus. (2008). Two-band superconductivity in $LaFeAsO_{0.89}F_{0.11}$ at very high magnetic fields. *Nature*, 453, 903-905

[62] *High-temperature superconductivity*. Retrieved October 20, 2010, from http://en.wikipedia.org/wiki/High_temperature_superconductivity

[63] J. G. Bednorz and K. A. Müller. (1986). Possible high Tc superconductivity in the Ba−La−Cu−O system. *Zeitschrift für Physik B Condensed Matter*, 64, 189-193.

[64] Mark Buchanan. (2001). Mind the pseudogap. *Nature*, 409, 8-11.

[65] Anthony J. Leggett. (2006). What DO we know about high Tc? *Nature Physics*, 2, 134 - 136

[66] S. Sanna, G. Allodi, G. Concas, A. D. Hillier, R. De Renzi. (2004). Nanoscopic Coexistence of Magnetism and Superconductivity in $YBa_2Cu_3O_{6+x}$ Detected by Muon Spin Rotation. *Physical Review Letters*, 93, 207001.

[67] A. F. Hebard, M. J. Rosseinsky, R. C. Haddon, D. W. Murphy, S. H. Glarum, T. T. M. Palstra, A. P. Ramirez, and A. R. Kortan. (1991). Superconductivity at 18 K in potassium-doped C_{60}. *Nature*, 350, 600 – 601.

[68] A. Y. Ganin, Y. Takabayashi, Y. Z. Khimyak, S. Margadonna, A. Tamai, M. J. Rosseinsky, and K. Prassides. (2008). Bulk superconductivity at 38 K in a molecular system. *Nature Materials*, 7, 367 – 371.

[69] N. W. Ashcroft. (1968). Metallic Hydrogen: A High-Temperature Superconductor? *Physical Review Letters*, 21, 1748-1749.

[70] J. Bardeen, L. N. Cooper, J. R. Schrieffer. (1957). Microscopic Theory of Superconductivity. *Physical Review*, 106, 162-164.

[71] J. Bardeen, L. N. Cooper, J. R. Schrieffer. (1957). Theory of Superconductivity. *Physical Review*, 108, 1175-1204.

[72] *BCS theory*. Retrieved October 20, 2010, from http://en.wikipedia.org/wiki/BCS_theory

[73] Yoichi Kamihara, Hidenori Hiramatsu, Masahiro Hirano, Ryuto Kawamura, Hiroshi Yanagi, Toshio Kamiya, and Hideo Hosono. (2006). Iron-Based Layered Superconductor: LaOFeP. *Journal of the American Chemical Society*, 128, 10012–10013.

[74] Yoichi Kamihara, Takumi Watanabe, Masahiro Hirano, and Hideo Hosono. (2008). Iron-Based Layered Superconductor $La[O_{1-x}F_x]FeAs$ (x = 0.05−0.12) with Tc = 26 K. *Journal of the American Chemical Society*, 130, 3296–3297.

[75] Zhi-An Ren, Guang-Can Che, Xiao-Li Dong, Jie Yang, Wei Lu, Wei Yi, Xiao-Li Shen, Zheng-Cai Li, Li-Ling Sun, Fang Zhou and Zhong-Xian Zhao. (2008). Superconductivity and phase diagram in iron-based arsenic-oxides $ReFeAsO_{1-\delta}$ (Re = rareearth metal) without fluorine doping. Europhysics Letters, 83, 17002.

[76] G. Wu, Y. L. Xie, H. Chen, M. Zhong, R. H. Liu, B. C. Shi, Q. J. Li, X. F. Wang, T. Wu, Y. J. Yan, J. J. Ying, X. H. Chen. (2009). *Superconductivity at 56 K in Samarium-doped SrFeAsF.* Retrieved October 20, 2010, from http://arxiv.org/PS_cache/arxiv/pdf/0811/0811.0761v3.pdf

[77] Marianne Rotter, Marcus Tegel, Dirk Johrendt. (2008). Superconductivity at 38 K in the Iron Arsenide $(Ba_{1-x}K_x)Fe_2As_2$. *Physical Review Letters*, 101, 107006.

[78] Kalyan Sasmal, Bing Lv, Bernd Lorenz, Arnold M. Guloy, Feng Chen, Yu-Yi Xue, and Ching-Wu Chu. (2008). Superconducting Fe-Based Compounds $(A_{1-x}Sr_x)Fe_2As_2$ with A=K and Cs with Transition Temperatures up to 37 K. *Physical Review Letters*, 101, 107007.

[79] Michael J. Pitcher, Dinah R. Parker, Paul Adamson, Sebastian J. C. Herkelrath, Andrew T. Boothroyd, Richard M. Ibberson, Michela Brunelli and Simon J. Clarke.

(2008). Structure and superconductivity of LiFeAs. *Chemical Communications*, issue 45, 5918-5920.

[80] Joshua H. Tapp, Zhongjia Tang, Bing Lv, Kalyan Sasmal, Bernd Lorenz, Paul C. W. Chu, and Arnold M. Guloy. (2008). LiFeAs: An intrinsic FeAs-based superconductor with Tc=18 K. *Physical Review B*, 78, 060505.

[81] Dinah R. Parker, Michael J. Pitcher, Peter J. Baker, Isabel Franke, Tom Lancaster, Stephen J. Blundell and Simon J. Clarke. (2009). Structure, antiferromagnetism and superconductivity of the layered iron arsenide NaFeAs. *Chemical Communications*, issue 16, 2189-2191.

[82] Fong-Chi Hsu, Jiu-Yong Luo, Kuo-Wei Yeh, Ta-Kun Chen, Tzu-Wen Huang, Phillip M. Wu, Yong-Chi Lee, Yi-Lin Huang, Yan-Yi Chu, Der-Chung Yan, and Maw-Kuen Wu. (2008). Superconductivity in the PbO-type structure α-FeSe. *Proceedings of the National Academy of Sciences*, 105, 14262–14264.

[83] Jun Zhao, Q. Huang, Clarina de la Cruz, Shiliang Li, J. W. Lynn, Y. Chen, M. A. Green, G. F. Chen, G. Li, Z. Li, J. L. Luo, N. L. Wang, Pengcheng Dai. (2008). Structural and magnetic phase diagram of $CeFeAsO_{1-x}F_x$ and its relation to high-temperature superconductivity. *Nature Materials*, 7, 953 – 959.

[84] Chul-Ho Lee, Akira Iyo, Hiroshi Eisaki, Hijiri Kito, Maria Teresa Fernandez-Diaz, Toshimitsu Ito, Kunihiro Kihou, Hirofumi Matsuhata, Markus Braden, Kazuyoshi Yamada. (2008). Effect of Structural Parameters on Superconductivity in Fluorine-Free $LnFeAsO_{1-y}$ (Ln = La, Nd). *Journal of the Physical Society of Japan*, 77, 083704.

[85] *Raman spectroscopy*. Retrieved October 20, 2010, from http://en.wikipedia.org/wiki/Raman_spectroscopy

[86] Gardiner, D.J. (1989). *Practical Raman spectroscopy*. Springer-Verlag.

[87] Placzek G. (1934). *Rayleigh Streeung und Raman Effekt*. Hdb. der Radiologie. (pp.209)

[88] R. K. Khanna, D. D. Stranz, and B. Donn. (1981). A spectroscopic study of intermediates in the condensation of refractory smokes: Matrix isolation experiments of SiO. *Journal of Chemical Physics,* 74, 2108-2115.

[89] BBC News. (2007). *Fake drugs caught inside the pack.* Retrieved October 20, 2010, from http://news.bbc.co.uk/2/hi/health/6314287.stm

[90] EAMON QUINN. (2007). *Irish Classic Is Still a Hit (in Calfskin, Not Paperback).* Retrieved October 20, 2010, from http://www.nytimes.com/2007/05/28/world/europe/28kells.html?_r=1

[91] David I. Ellis, Royston Goodacre. (2006). Metabolic fingerprinting in disease diagnosis: biomedical applications of infrared and Raman spectroscopy. *Analyst*, 131, 875-885.

[92] David L. Jeanmaire, Richard P. Van Duyne. (1977). Surface raman spectroelectrochemistry: Part I. Heterocyclic, aromatic, and aliphatic amines adsorbed on the anodized silver electrode. *Journal of Electroanalytical Chemistry*, 84, 1-20.

[93] R. S. Chao, R. K. Khanna, E. R. Lippincott. Theoretical and experimental resonance Raman intensities for the manganate ion. *Journal of Raman Spectroscopy*, 3, 121-131.

[94] Katrin Kneipp, Harald Kneipp, Irving Itzkan, Ramachandra R. Dasari, Michael S. Feld. (1999). Surface-enhanced non-linear Raman scattering at the single-molecule level. *Chemical Physics*, 247, 155-162.

[95] Matousek, P., Morris, M.D., Everall, N., Clark, I.P., Towrie, M., Draper, E., Goodship, A., Parker, A.W. (2005). Numerical Simulations of Subsurface Probing in Diffusely Scattering Media Using Spatially Offset Raman Spectroscopy. *Applied Spectroscopy*, 59, 288-308.

[96] Laurence D. Barron, Lutz Hecht, Iain H. McColl, Ewan W. Blanch. (2004). Raman optical activity comes of age. *Molecular Physics*, 102, 731-744.

[97] Matousek, P., Parker, A.W. (2006). Bulk Raman Analysis of Pharmaceutical Tablets. *Applied Spectroscopy*, 60, 1353-1357.

[98] P. Matousek, N. Stone. (2007). Prospects for the diagnosis of breast cancer by noninvasive probing of calcifications using transmission Raman spectroscopy. *Journal of Biomedical Optics*, 12, 024008.

[99] *Raman scattering*. Retrieved October 20, 2010, from http://en.wikipedia.org/wiki/Raman_scattering

[100] *Interaction of Light with Matter*. Retrieved October 20, 2010, from http://www.files.chem.vt.edu/chem-ed/light/light-ma.html

[101] John R. Ferraro, Kazuo Nakamoto and Chris W. Brown. (2003). *Introductory Raman Spectroscopy (Second edition)*. Elsevier. (pp.7).

[102] Ewen Smith, Geoffrey Dent. (2005). *Modern Raman Spectroscopy - A Practical Approach*. John Wiley & Sons Ltd.

[103] George Turrell, Jacques Corset. (1996). *Raman Microscopy: Developments and Applications.* Elsevier Ltd.

[104] Richard L. McCreery. (2000). *Raman Spectroscopy for Chemical Analysis.* John Wiley & Sons Ltd.

[105] Maher S. Amer. (2009). *Raman Spectroscopy for Soft Matter Applications.* John Wiley & Sons Ltd.

[106] David W. Hahn. (2007). *Raman Scattering Theory*. Retrieved October 20, 2010, from http://plaza.ufl.edu/dwhahn/Raman%20Scattering%20Theory.pdf

[107] Ivan V. Markov. (2003). *Crystal Growth for Beginners: Fundamentals of Nucleation, Crystal Growth, and Epitaxy.* World Scientific Publishing Co. Pte. Ltd.

[108] Kenneth A. Jackson. (2004). *Kinetic Processes: Crystal Growth, Diffusion, and Phase Transitions in Materials.* WILEY-VCH Verlag GmbH & Co. KGaA, Weinheim.

[109] K. Sato, Y. Furukawa, K. Nakajima. (2001). *Advances in Crystal Growth Research.* ELSEVIER SCIENCE B.V.

[110] Zahid Amjad. (2002). *Advances in Crystal Growth Inhibition Technologies.* Kluwer Academic Publishers.

[111] Peter Capper. (2005). *Bulk Crystal Growth of Electronic, Optical & Optoelectronic Materials.* John Wiley & Sons, Ltd.

[112] Georg Müller, Jean-Jacques Métois, Peter Rudolph. (2004). *Crystal Growth - From Fundamentals to Technology*. ELSEVIER B.V.

[113] Kullaiah Byrappa, Tadashi Ohachi. (2003). *Crystal Growth Technology (Springer Series in Materials Processing).* Springer.

[114] H. J. Scheel, T. Fukuda. (2003). *Crystal Growth Technology.* John Wiley & Sons, Ltd.

[115] Robert S. Feigelson. (2004). *50 Years Progress in Crystal Growth: A Reprint Collection.* ELSEVIER B.V.

[116] K. Byrappa, Masahiro Haber. (2001). *Handbook of Hydrothermal Technology (Materials and Processing Technology).* Noyes Publications / William Andrew Publishing, LLC.

[117] Sadik Dost, Brian Lent. (2007). *Single Crystal Growth of Semiconductors from Metallic Solutions.* Elsevier B.V.

[118] Ichiro Sunagawa. (2005). *Crystals: Growth, Morphology, & Perfection.* Cambridge University Press.

[119] R. A. Laudise. (1970). *The Growth of Single Crystals*. Prentice-Hall.

[120] Kenneth A. Jackson. (2000). *Handbook of Semiconductor Technology, Vol. 2, Processing of Semiconductors.* Wiley-VCH.

[121] A.J. Williams, T.M. McQueen, R.J. Cava. (2009). The stoichiometry of FeSe. *Solid State Communications*, 149, 1507-1509.

[122] M.K. Wu, F.C. Hsu, K.W. Yeh, T.W. Huang, J.Y. Luo, M.J. Wang, H.H. Chang, T.K. Chen, S.M. Rao, B.H. Mok, C.L. Chen, Y.L. Huang, C.T. Ke, P.M. Wu, A.M. Chang, C.T. Wu, T.P. Perng. (2009). The development of the superconducting PbO-type β-FeSe and related compounds. *Physica C: Superconductivity*, 469, 340-349.

[123] V.G. Hadjiev, M.N. Iliev, K. Sasmal, Y.-Y. Sun, C.W. Chu. (2008). Raman spectroscopy of RFeAsO (R=Sm, La). *Physical Review B*, 77, 220505.

[124] S.C. Zhao, D. Hou, Y. Wu, T.-L. Xia, A.M. Zhang, G.F. Chen, J.L. Luo, N.L. Wang, J.H. Wei, Z.Y. Lu, Q.M. Zhang. (2009). Raman spectra in iron-based quaternary $CeO_{1-x}F_xFeAs$ and $LaO_{1-x}F_xFeAs$. *Superconductor Science and Technology,* 22, 015017.

[125] A.P. Litvinchuk, V.G. Hadjiev, M.N. Iliev, B. Lv, A.M. Guloy, C.W. Chu. (2008). Raman-scattering study of $K_xSr_{1-x}Fe_2As_2$ (x=0.0,0.4). *Physical Review B*, 78, 060503.

[126] T.L. Xia, D. Hou, S.C. Zhao, A.M. Zhang, G.F. Chen, J.L. Luo, N.L. Wang, J.H. Wei, Z.-Y. Lu, Q.M. Zhang. Raman phonons of α-FeTe and $Fe_{1.03}Se_{0.3}Te_{0.7}$ single crystals. *Physical Review B*, 79, 140510.

[127] T.M. McQueen, A.J. Williams, P.W. Stephens, J. Tao, Y. Zhu, V. Ksenofontov, F. Casper, C. Felser, R.J. Cava. (2009). Tetragonal-to-Orthorhombic Structural Phase Transition at 90 K in the Superconductor $Fe_{1.01}Se$. *Physical Review Letters*, 103, 057002.

[128] M. Cardona, G. Guentherodt. (1979). *Light Scattering in Solids VIII: Fullerenes, Semiconductor Surfaces, Coherent Phonons (Topics in Applied Physics)*. Springer Verlag, Berlin.

[129] I.W. Johnstone, D.J. Lockwood, G. Mischler. (1978). Examples of a dynamic Jahn-Teller system: Raman scattering from electronic excitations and phonons in paramagnetic and antiferromagnetic $FeCl_2$ and $FeBr_2$. *Journal of Physics C: Solid State Physics*, 11, 2147.

[130] I.W. Johnstone, D.J. Lockwood, D. Bertrand, G. Mischler. (1980). Low lying excitations of Fe^{2+} ions in the mixed antiferromagnet $Fe_{1-x}Mn_xCl_2$ (Raman scattering study). *Journal of Physics C: Solid State Physics,* 13, 2549.

[131] Michael R. Norman. (2008). High-temperature superconductivity in the iron pnictides. *Physics*, 1, 21.

[132] K. Haule, G. Kotliar. (2009). Coherence–incoherence crossover in the normal state of iron oxypnictides and importance of Hund's rule coupling. *New Journal of Physics*, 11, 025021.

[133] *Evanescent wave*. Retrieved October 20, 2010, from http://en.wikipedia.org/wiki/Evanescent_wave

[134] Tineke Thio. (2006). A Bright Future for Subwavelength Light Sources. *American Scientist*, 94, 40-47.

[135] Marston, Philip L.; Matula, T.J. (2002). Scattering of acoustic evanescent waves by circular cylinders: Partial wave series solution. *Acoustical Society of America Journal,* 111, 2378.

[136] Andrew Neice. (2010). Methods and Limitations of Subwavelength Imaging. *Advances in Imaging and Electron Physics*, 163, 117-140.

[137] Hafnium(IV) oxide. Retrieved October 20, 2010, from http://en.wikipedia.org/wiki/Hafnium%28IV%29_oxide

[138] G. D. Wilk, R. M. Wallace, J. M. Anthony. (2001). High-κ gate dielectrics: Current status and materials properties considerations. *Journal of Applied Physics,* 89, 5243-5275.

[139] Donald M. Mattox. (2010). *Handbook of Physical Vapor Deposition (PVD) Processing (Second edition)*. Elsevier Inc.

[140] Paul E. Minton. (1986). *Handbook of Evaporation Technology*. Noyes Publications.

[141] Rointan F. Bunshah. (1994). *Handbook of Deposition Technologies for Films and Coatings: Science, Applications and Technology (Second Edition)*. Noyes Publications.

[142] W.P. Strickland. (1990). Optical thin film technology: Past, present and future. *Proceedings of the 33rd Annual Technical Conference, Society of Vacuum Coaters*, 221.

[143] Leon I. Maissel, Reinhard Glang. (1970). *Handbook of Thin Film Technology (McGraw-Hill Handbooks)*. McGraw-Hill.

[144] E. Ruthner, P. Goldfinger, J.P. Hirth. (1964). *Condensation and Evaporation of Solids.* Chapman-Hall.

[145] R.F. Bunshah, R.S. Juntz. (1972). The Influence of Ion Bombardment on the Microstructure of Thick Deposits Produced by High Rate Physical Vapor Deposition Processes. *Journal of Vacuum Science and Technology*, 9, 1404-1405.

[146] John R. Morley, Hugh R. Smith. (1972). High Rate Ion Production for Vacuum Deposition. *Journal of Vacuum Science and Technology*, 9, 1377-1378.

[147] Y. S. Kuo, R. F. Bunshah, D. Okrent. (1986). Hot hollow cathode and its applications in vacuum coating: A concise review. *Journal of vacuum science & technology*. A4, 397.

[148] *Chemical-mechanical planarization*. Retrieved October 20, 2010, from http://en.wikipedia.org/wiki/Chemical-mechanical_planarization

[149] Viktor G Veselago. (1968). The electrodynamics of substances with simultaneously negative values of ε and μ. *Soviet Physics Uspekhi,* 10, 509.

[150] J. B. Pendry. (2000). Negative Refraction Makes a Perfect Lens. *Physical Review Letters*, 85, 3966-3969.

[151] David R. Smith, David Schurig, Marshall Rosenbluth, Sheldon Schultz, S. Anantha Ramakrishna, and John B. Pendry. (2003). Limitations on subdiffraction imaging with a negative refractive index slab. *Applied Physics Letters*, 82, 1506-1508.

[152] Nicholas Fang, Hyesog Lee, Cheng Sun, Xiang Zhang. (2005). Sub–Diffraction-Limited Optical Imaging with a Silver Superlens. *Science*, 308, 534-537

[153] David O. S. Melville, Richard J. Blaikie. (2005). Super-resolution imaging through a planar silver layer. *Optics Express*, 13, 2127-2134.

[154] Mark J. Bloemer, Michael Scalora. (1998). Transmissive properties of Ag/MgF_2 photonic band gaps. *Applied Physics Letters*, 72, 1676-1678.